

POLITECNICO DI TORINO

Master's Degree Course in Aerospace Engineering



MASTER'S THESIS

Development of a digital twin for the validation of prognostic algorithms for electromechanical actuators

Supervisors

Prof. Paolo Maggiore
Ing. Matteo D. L. Dalla Vedova
Ing. Pier Carlo Berri
Ing. Gaetano Quattrocchi

Candidate

Raffaele Giordano
ID: 275549

Academic Year 2020 - 2021

*A chi è stato sempre presente.
A chi ha sempre creduto in me.
E a me stesso.*

Abstract

For several years now, modern aircraft design has been based on a "More Electric" philosophy. The latter is a concept of great interest to the aerospace industry as it allows the overall efficiency of aircraft to be increased while ensuring a perfect balance between safety and reliability. The thesis work presented is based on the study of an electro-mechanical actuator (EMA) which represents an innovative solution for replacing the electro-hydraulic actuators (EHA) widely used in the aerospace industry. In fact, simultaneously with the development of the "More Electric" project philosophy, there has been increasing interest in the study of EMAs and their use as actuation systems for flight controls. The thesis focuses on the description and simulation, through a numerical reference model developed in the Matlab-Simulink environment, of the operation of an electromechanical servomechanism on a test bench. In addition, it was necessary to build and validate a similar digital twin model in the Simscape environment to describe real phenomena related to non-linearities. The validation process of the model produced in Simscape was characterised by the choice of different elementary blocks and the tuning of some parameters. This made it possible to produce simulations that faithfully reproduce the real behaviour of the characteristic quantities of the electromechanical actuator on the test bench. The various simulations confirmed the correct modelling of the electromechanical servomechanism in Simscape, allowing the subsequent development of prognostic algorithms.

Contents

List of Tables	5
List of Figures	6
1 Actuation system	14
1.1 Electromechanical servomechanism	14
1.2 Electric motor	16
1.2.1 DC motor	16
1.3 Brushless DC motor - BLDC	17
1.3.1 Rotor	18
1.3.2 Stator	18
1.3.3 Working principle	20
1.4 Permanent magnet synchronous motor - PMSM	22
1.4.1 Rotor	22
1.4.2 Stator	23
1.4.3 Working principle	23
2 Test Bench Architecture	24
2.1 Actuation module	25
2.2 SIMATIC Microbox PC	26
2.3 SINAMICS Control Unit	28
2.4 SINAMICS Power Module	29
2.5 SIMOTICS Synchronous Motor	31
2.6 Reduction gearbox	34
2.7 Encoder	38
2.8 Braking module	41
2.9 Servomotor	42
2.9.1 Arduino code	42
2.10 Transmission system	45
2.11 Roller chain	45
2.12 Sprockets	45

2.13	Tensioner	46
3	Brushless DC Motor	47
3.1	High-Fidelity model description	47
3.2	Command and external torque block	50
3.3	Control Electronics PID subsystem	51
3.4	Hall sensors subsystem	52
3.5	Inverter Model subsystem	53
3.5.1	Evaluation of active phase subsystem	54
3.5.2	Pulse Width Modulation	55
3.5.3	Hysteresis PWM subsystem	56
3.5.4	Three-phase bridge subsystem	58
3.6	BLDC electromagnetic model subsystem	58
3.6.1	Computation of back-EMF coefficients subsystem	59
3.6.2	Three-phase RL model subsystem	61
3.6.3	Computation of motor-torque subsystem	62
3.7	Motor transmission dynamic model subsystem	63
3.8	Signal acquisition subsystem	66
3.9	Simscape modelling	67
3.10	Three-phase bridge and RL model Simscape subsystem	68
3.10.1	Three-phase bridge	69
3.10.2	Three-phase stator circuit	70
3.11	Brushless DC Simscape model validation	73
3.11.1	Step command	74
3.11.2	Ramp command	82
3.11.3	Sinusoidal command	85
3.11.4	Step, ramp and external load	88
4	Permanent Magnet Synchronous Motor (PMSM)	93
4.1	High-Fidelity model description	93
4.2	Command block and external torque blocks	93
4.3	Sinusoidal EMA subsystems	95
4.4	Control Electronics PID subsystem	95
4.5	Resolver block subsystem	99
4.6	Inverter subsystem	100
4.6.1	Evaluation of phase currents subsystem	100
4.7	BLDC electromagnetic model subsystem	106
4.7.1	Computation of back-EMF coefficients subsystem	107
4.8	Signal acquisition subsystem	108
4.9	Motor transmission dynamical model subsystem	110
4.10	PMSM Simscape model validation	112
4.10.1	Step command	113

4.10.2	Ramp command	121
4.10.3	Sinusoidal command	124
4.10.4	Step, ramp and external load	127
5	Results and conclusions	132
A	Brushless DC motor	133
A.1	Step command	133
A.2	Ramp command	136
A.3	Sinusoidal command	139
A.4	Step, ramp and external load	142
B	PMSM	145
B.1	Step command	145
B.2	Ramp command	148
B.3	Sinusoidal command	151
B.4	Step, ramp and external load	154

List of Tables

2.1	Basic Data	27
2.2	Ports	27
2.3	Rated Data	30
2.4	Engineering Data of the electric motor	32
2.5	Physical constants of the electric motor	33
2.6	Mechanical Data	33
2.7	Data of the electric motor	33
2.8	Data of Planetary Gearbox	37
2.9	Data of the Encoder	39
2.10	Encoder materials	39
2.11	Encoder Mechanical specifications	40
2.12	Data of the Servomotor	42
2.13	Data of the Sprockets	45
3.1	Mosfet Ideal Switching Data	70
3.2	Data step command	74
3.3	Data ramp command	82
3.4	Data sinusoidal command	85
3.5	Characteristics of two commands	88
3.6	Characteristics of the external load	89
4.1	Data step command	113
4.2	Data ramp command	121
4.3	Data sinusoidal command	124
4.4	Characteristics of two commands	127
4.5	Characteristics of the external load	128

List of Figures

1.1	Electromechanical actuator	15
1.2	Working principle of brush motor	17
1.3	Permanent magnet DC motor (a) and brushless motor (b) structure	18
1.4	Electrical windings configuration	19
1.5	Brushless DC motor working principle [9]	21
1.6	Permanent magnet synchronous motor	22
1.7	Concentrated windings and distributed windings	23
2.1	Test bench	25
2.2	Test bench top view	25
2.3	SIMATIC IPC427E Microbox PC	26
2.4	Control unit CU310-2 PN (PROFINET)	28
2.5	Power module PM240-2	29
2.6	SIMOTICS S 1FK7060-2AC71-1CG0 synchronous motor	31
2.7	Torque characteristics synchronous motor	32
2.8	Reduction gearbox	34
2.9	Speed profile	35
2.10	Encoder	38
2.11	Encoder's dimensions	39
2.12	Braking load trend	43
2.13	Fitting data	44
3.1	HF model	48
3.2	HF model subsystems	48
3.3	Command and external torque block	50
3.4	Control Electronics PID subsystem	51
3.5	PID	52
3.6	Hall sensors subsystem	53
3.7	Inverter Model subsystem	54
3.8	Evaluation of active phase subsystem	55
3.9	Working principle of PWM	56
3.10	Hysteresis PWM subsystem	57
3.11	Three-phase bridge subsystem	58

3.12	BLDC electromagnetic model subsystem	59
3.13	Computation of back-EMF coefficients subsystem	60
3.14	Three-phase RL model subsystem	61
3.15	Computation of motor-torque subsystem	62
3.16	Motor transmission dynamic model subsystem	63
3.17	Borello friction model	64
3.18	Signal acquisition subsystem	66
3.19	Three-phase bridge and RL model Simscape subsystem	68
3.20	Three-phase bridge	69
3.21	Electrical windings	71
3.22	Voltage sensing SSC	72
3.23	Angular position of the motor	74
3.24	Angular speed of the motor	75
3.25	Angular position of the user	75
3.26	I_A	76
3.27	I_A at steady state	76
3.28	I_B	77
3.29	I_B at steady state	77
3.30	I_C	78
3.31	I_C at steady state	78
3.32	V_A	79
3.33	V_A at steady state	79
3.34	V_B	80
3.35	V_B at steady state	80
3.36	V_C	81
3.37	V_C at steady state	81
3.38	Angular position of the motor	82
3.39	Angular speed of the motor	83
3.40	Angular position of the user	83
3.41	I_A at steady state	84
3.42	V_A at steady state	84
3.43	Angular position of the motor	85
3.44	Angular speed of the motor	86
3.45	Angular position of the user	86
3.46	I_A at steady state	87
3.47	V_A at steady state	87
3.48	Signal builder command	88
3.49	Signal builder load	89
3.50	Angular position of the motor	90
3.51	Angular speed of the motor	90
3.52	Angular position of the user	91
3.53	I_A at steady state	91

3.54	V_A at steady state	92
4.1	PMSM model subsystems	94
4.2	Command block and external torque blocks	94
4.3	Sinusoidal EMA subsystem	95
4.4	Control Electronics PID subsystem	96
4.5	PID	96
4.6	Resolver block subsystem	99
4.7	Inverter subsystem	100
4.8	Evaluation of phase currents subsystem	101
4.9	Reference system transformation	103
4.10	Inverse Park matrix	103
4.11	Inverse Clark matrix	104
4.12	BLDC electromagnetic model subsystem	106
4.13	Computation of back-EMF coefficients subsystem	107
4.14	Signal acquisition	108
4.15	Clarke transformation	109
4.16	Clarke matrix	109
4.17	Motor transmission dynamical model subsystem	110
4.18	Borello friction model	111
4.19	Angular position of the motor	113
4.20	Angular speed of the motor	114
4.21	Angular position of the user	114
4.22	I_A	115
4.23	I_A at steady state	115
4.24	I_B	116
4.25	I_B at steady state	116
4.26	I_C	117
4.27	I_C at steady state	117
4.28	V_A	118
4.29	V_A at steady state	118
4.30	V_B	119
4.31	V_B at steady state	119
4.32	V_C	120
4.33	V_C at steady state	120
4.34	Angular position of the motor	121
4.35	Angular speed of the motor	122
4.36	Angular position of the user	122
4.37	I_A at steady state	123
4.38	V_A at steady state	123
4.39	Angular position of the motor	124
4.40	Angular speed of the motor	125
4.41	Angular position of the user	125

4.42	I_A at steady state	126
4.43	V_A at steady state	126
4.44	Signal builder command	127
4.45	Signal builder load	128
4.46	Angular position of the motor	129
4.47	Angular speed of the motor	129
4.48	Angular position of the user	130
4.49	I_A at steady state	130
4.50	V_A at steady state	131
A.1	Phase A current	133
A.2	Phase B current	134
A.3	Phase C current	134
A.4	Phase A tension	134
A.5	Phase B tension	135
A.6	Phase C tension	135
A.7	Phase A current	136
A.8	Phase B current	136
A.9	Phase C current	137
A.10	Phase A tension	137
A.11	Phase B tension	137
A.12	Phase C tension	138
A.13	Phase A current	139
A.14	Phase B current	139
A.15	Phase C current	140
A.16	Phase A tension	140
A.17	Phase B tension	140
A.18	Phase C tension	141
A.19	Phase A current	142
A.20	Phase B current	142
A.21	Phase C current	143
A.22	Phase A tension	143
A.23	Phase B tension	144
A.24	Phase C tension	144
B.1	Phase A current	145
B.2	Phase B current	146
B.3	Phase C current	146
B.4	Phase A tension	146
B.5	Phase B tension	147
B.6	Phase C tension	147
B.7	Phase A current	148
B.8	Phase B current	148
B.9	Phase C current	149

B.10 Phase A tension	149
B.11 Phase B tension	149
B.12 Phase C tension	150
B.13 Phase A current	151
B.14 Phase B current	151
B.15 Phase C current	152
B.16 Phase A tension	152
B.17 Phase B tension	152
B.18 Phase C tension	153
B.19 Phase A current	154
B.20 Phase B current	154
B.21 Phase C current	155
B.22 Phase A tension	155
B.23 Phase B tension	156
B.24 Phase C tension	156

Introduction

“More Electric” philosophy foresees the use of electrical energy as the primary source of power for all on-board systems and allows for the complete or partial replacement of other systems (e.g. hydraulic and pneumatic system), favouring a reduction in operating costs promoted by lower fuel consumption, resulting in less weight, and simplified maintenance processes [1]. In addition, the interconnection of several subsystems to the same power source allows the simultaneous implementation of diagnostic and prognostic algorithms capable of more easily identifying malfunctions at any point in the network and predicting possible scenarios avoiding potential failures [2]. Some of the "More Electric" aircraft currently in operation are the Boeing 787 and the Airbus 380.

The thesis work is based on the study of electro-mechanical actuator (EMA), which represents an innovative solution for replacing the electro-hydraulic actuators (EHAs) widely used in the aerospace industry. In fact, over the last few years and at the same time as the development of the “More Electric” design philosophy, there has been increasing interest in the study of EMAs and their use as flight control actuation systems. Nowadays, EMAs are mainly used on Unmanned Aerial Vehicles (UAVs) and civil aircraft for secondary flight control only, while EHAs are still widely used for primary flight control. The reason for this is that EMAs have a lower safety factor and are prone to failures that are not yet fully known, so they cannot be used on primary flight controls because failure to actuate the moving surface or abnormal behaviour of the surface could cause irreparable damage resulting in the loss of the aircraft. Therefore, it is necessary to carry out various studies and simulations on the ground to test the correct operation of an electromechanical servomechanism and to identify the multiple causes that would lead to irreparable failures when used in flight.

The design philosophy adopted for a civil aircraft is “Safe-Life”, which consists of replacing a component at the end of its operational life regardless of whether it is defective or damaged. The main disadvantage of this method is that it must guarantee a high safety coefficient and overlooks possible initial manufacturing defects in the components. The project method called “Prognostic and Health Management (PHM)” has made it possible to estimate the residual service life

of components, identified by the “Remaining Useful Life (RUL)” parameter, and their degree of damage in parallel with their use in missions [3], [4]. This estimation foresees the implementation, during the mission, of a fault diagnostics and prognostics system that involves the acquisition and processing of data related to the on-board devices and comparing them with a reference model that returns the nominal response of the system. Fault diagnosis is made by comparing the data with the eventual removal of the device in question from the power link. Prognostics techniques focus on the definition of the “Remaining Useful Life” through which the remaining time of use of the component before failure occurs is estimated. The implementation of this method allows greater efficiency in fault management and considerably reduces the costs and operational difficulties associated with maintenance while ensuring high performance, safety, and reliability.

Therefore, this thesis focuses on the description and simulation, using a High-Fidelity (HF) numerical reference model defined and developed in the Matlab-Simulink environment, of the operation of an electromechanical servomechanism and on the need to build an analogous physical model in the Simscape environment, which allows to simulate nonlinear physical phenomena bypassing the systematic construction of linear and differential equations in Simulink. In fact, one of the advantages of using Simscape is that the construction of the physical model allows the equations for solving the system to be implemented automatically. A further advantage offered by the Simscape environment is that of being able to build multi-domain models, i.e., it allows the joint and simultaneous analysis of phenomena of different nature and their overall interaction on the system, making the analysis even more realistic and detailed. An example, could be the electrical modelling of a system and the simultaneous thermal analysis of the electrical circuits to consider heat dissipation due to the Joule effect and potential overheating and demagnetisation of the circuits. Finally, by using Simscape, it was possible to build simplified but at the same time functional physical models perfectly capable of describing the real physical effects. This aspect was conditioned by the fact that various data relating to components are not always directly available and, therefore, it is necessary to simplify the modelling but at the same time guarantee a correct description of the phenomena. The first part of the thesis focuses on the description of the High-Fidelity numerical model of an electromechanical servomechanism characterised by the presence of a brushless DC motor which generates a counter-electromotive force with a trapezoidal waveform on the stator phases. We proceed with the description of the analogous model built in Simscape, which simulates the operation of the inverter and the electromagnetic phenomena characteristic of the stator windings. The validation of the model produced in Simscape was obtained by conducting in parallel several simulations in the time domain on the two models under examination, setting different types of control and different initial conditions, and

comparing the values and trends of the characteristic quantities of the system. Subsequently, the model of the electromechanical servomechanism physically present on the test bench was described. It is characterised by the presence of a PMSM (Permanent Magnet Synchronous Motor) which generates a counter-electromotive force with a sinusoidal waveform on the stator phases. The reason why the physical model through Simscape was initially produced by analogy with the numerical model of the brushless DC motor is that simulating the operation of the latter is numerically less laborious since the control logic for driving the inverter processes ON-OFF signals for switching the phases. For a PMSM motor, this drive logic cannot be envisaged as phase switching is not ON-OFF but follows sinusoidal signals. The numerical model of the PMSM is a perfectly representative model of the operation of the real motor physically present on the test bench since its characterisation has already been conducted [10], [11].

Similarly, to what was done for the brushless DC motor, the validation of the physical model in Simscape environment was obtained by generating in parallel several simulations in the time domain and comparing the values and trends of the characteristic quantities of the system produced by the two models. The physical model obtained and validated in Simscape environment can simulate the correct operation of the electromechanical servomechanism and it represents a valid tool to develop prognostic activities.

Chapter 1

Actuation system

The actuation system is used to move the aircraft's control surfaces in such a way as to generate pressure distributions around the profile and consequently the necessary aerodynamic forces. The deflection of the control surfaces of the primary flight controls (ailerons, elevator, rudder) produces torques with respect to the aircraft's centre of gravity that can vary its attitude and position along the three axes of rotation. This allows the pilot to control the trajectory of the aircraft throughout the mission. The control surfaces of the secondary flight controls (flaps, slats, spoilers) make it possible to vary the aerodynamic coefficients of the aircraft and their activation is only provided for during certain phases of the mission (e.g. take-off and landing). Therefore, the actuators connected to the control surfaces must be characterised by a high safety coefficient and, in the event of a failure, an adequate number of redundancies must be arranged so as to ensure the correct movement of the mobile surfaces for the duration of the mission.

Actuation systems are classified into different types according to the chain of command and the architecture of the system. In particular, they are divided into hydro-mechanical servomechanism, electro-hydraulic servomechanism, electro-hydrostatic servomechanism and electromechanical servomechanism. For the purposes of this thesis, the operation of the electromechanical servomechanism is summarised hereafter.

1.1 Electromechanical servomechanism

An electromechanical servomechanism is an innovative solution that reflects the principles of a "More Electric" and "All Electric" aircraft design philosophy [5]. It makes it possible to eliminate the hydraulic circuit by using as a primary source of power the electrical power used to drive an electric motor which transforms this electrical power into mechanical power used to move the user. This system makes

it possible to eliminate several components linked to the hydraulic circuit, such as the oil under pressure in the actuator chambers, wiring and valves, making the system more compact, lighter, more efficient and allowing easier maintenance and lower operating costs [6]. The use of electromechanical servomechanisms, as already mentioned, is still limited to "non-safety critical functions" because, to date, not all possible failure modes have been defined. For example, a particular problem with this system relates to the difficulty of maintaining a fixed position under the action of an applied load, since this would require a power supply of the same phases, which would lead to overheating of the windings and the the insulating material used.

In the figure 1.1 is a representative diagram of an electromechanical servomechanism [7].

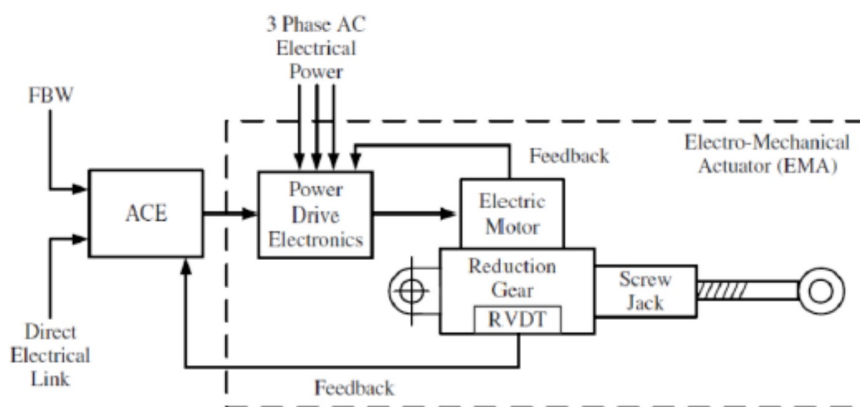


Figure 1.1: Electromechanical actuator

The operating process of an electromechanical servomechanism involves the input of an electrical signal, proportional to the pilot command, which is processed by the Actuator Control Electronics (ACE). The latter also receives the instantaneous position assumed by the user, measured by means of position transducers (LVDT), and processes a signal corresponding to the relative error between the command and the user's position. This signal passes through a filter and an amplifier which amplifies the signal power, given at low power, so that it can be transmitted to the electric motor. Based on the input error signal and the feedback signal of the electric motor, the Power Drive Electronics (PDE) receives a three-phase power supply and it regulates the power required to supply the electric motor. Between the electric motor and the user there is a gearbox which has the function of a reducer, i.e. that of adapting the angular speed produced on the fast shaft of the electric motor to the speed required to move the user, so as to increase the torque delivered at the same mechanical power. The presence of the gearbox is

also useful in that it makes it possible to have smaller overall dimensions and therefore lower weights for the same power delivered by the electric motor, while at the same time ensuring that the moving surfaces of the secondary controls can be moved at a speed of around $5 - 6 \text{ }^\circ/s$ and the primary flight controls at around $50 - 60 \text{ }^\circ/s$, within the performance range envisaged by the standard. In fact, since the power is directly proportional to the torque and angular speed of the motor, it is necessary to increase the angular speed to reduce the torque and, therefore, the overall dimensions and weight, with the same power. The last stage of the system is characterised by a mechanism that converts rotational motion into translational motion. This effect is achieved by using screw-nut screw actuators and the coupling of these two devices is achieved through a ball screw system or a roller system to minimise the effects of friction and wear. The first coupling solution consists of balls rotating in a cylindrical helical guide; the balls allow stresses to be transferred if they are not too small. The second solution, which is suitable if the helix pitch is too small, consists of rollers obtained on the thread of the screw which allow very high transmission ratios to be achieved.

1.2 Electric motor

The most commonly used electric motors in the aerospace industry are the *brushless DC motor* and the *permanent magnet synchronous motor*. Both belong to the category of AC synchronous motors, as they rotate at an angular speed synchronised with the frequency of the motor supply currents. In addition, they are brushless motors and, since the 1970s, have been a viable substitute for classic DC brush motors called *DC motors*.

1.2.1 DC motor

The general structure of a DC brush motor is characterised by an external permanent magnet stator and a mobile internal rotor winding in which the current flows as shown in the figure 1.2.

The current flows from a tension generator through the brushes, which are usually made of graphite, to the collector (or commutator) to the rotor winding. Exploiting the principle of the Lorentz force that is generated, the rotor winding rotates as it is subjected to the action of a torque and, thanks to the collector changing the direction of rotation of the current, it is possible to make the electric motor rotate in one single direction. The risk of using this technology is the sliding contacts between the brushes and the collector. The moment the collector detaches from the brush, the current instantly drops to zero and the high density of electrical charge present tends to return to the brushes, generating an electric arc. This phenomenon is extremely dangerous and should be avoided, as the sparks that are

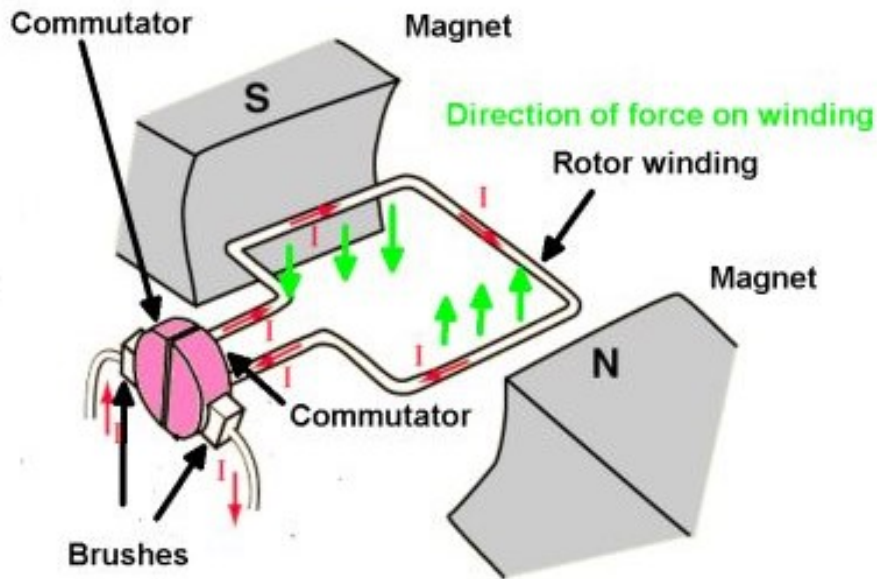


Figure 1.2: Working principle of brush motor

formed could cause a fire or even an explosion in environments where oxygen or reactants are present. A further problem with permanent magnet DC motor is the wear and tear caused by the sliding contacts between the brushes and the collector, which would require periodic maintenance and thus increase operating costs.

A brushless motor avoids these disadvantages by ensuring better performance in terms of rotation speed and torque output, less weight and space requirements, less noise during operation and better efficiency, which guarantees a longer service life [8]. Depending on the type of power supply imposed by the control logic, the waveform of the currents of each phase and the counter-electromotive force generated, it is possible to classify two types of brushless motors:

- Brushless DC Motor (BLDC)
- Permanent Magnet Synchronous Motor (PMSM)

1.3 Brushless DC motor - BLDC

The main difference between a classic DC brush motor and a brushless DC motor (BLDC) lies in the fact that the magnets are located on the rotor, while the electrical windings are located on the stator as shown in the figure 1.3.

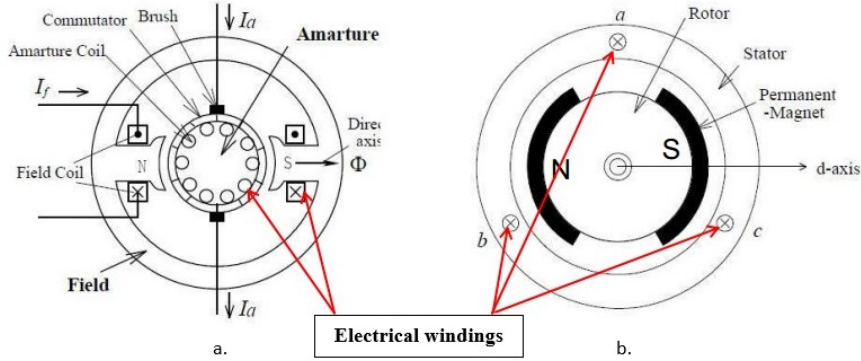


Figure 1.3: Permanent magnet DC motor (a) and brushless motor (b) structure

1.3.1 Rotor

It consists of the permanent magnets which define the pole pairs in the inductive circuit. The number of pole pairs can vary from one to eight, and the higher the number, the more regular the torque but the lower the angular speed. Permanent magnets are made of hard ferromagnetic materials, i.e. materials with high resistance to demagnetisation (they have very high values of the coercive magnetic field) and high magnetic induction values. Initially, the materials used were low-cost, i.e. ferro-silicon and ferrite, but they also had a low magnetic flux density. Nowadays, rare-earth materials are used, which are more expensive but have far superior magnetic properties. These consist mainly of samarium-cobalt or neodymium-iron-boron alloys. However, these elements have the disadvantage of having an average operating temperature lower than that of classic ferromagnetic materials. It will therefore be necessary, during the design phase, to ensure that the operating temperatures never reach temperatures which would lead to demagnetisation ($200^{\circ} C$ for samarium-cobalt, $80^{\circ} C$ for neodymium-iron-boron) [9].

1.3.2 Stator

It consists of a core around which are the electrical windings, made of insulated copper or aluminium. The arrangement of the windings generally provides for a three-phase circuit representing the induced circuit. The three-phase stator configuration can be arranged in two different ways: in a star configuration, also known as a Y configuration, or in a triangle configuration, also known as a delta (Δ) configuration. The respective diagrams are shown in the figure 1.4.

The main difference is that in the delta configuration the phase voltage is equal to the line voltage whereas in the star configuration the phase voltage is equal to $1/\sqrt{3}$ of the line voltage. When the same line voltage is applied, the delta configuration generates higher currents resulting in a higher motor torque than the same motor

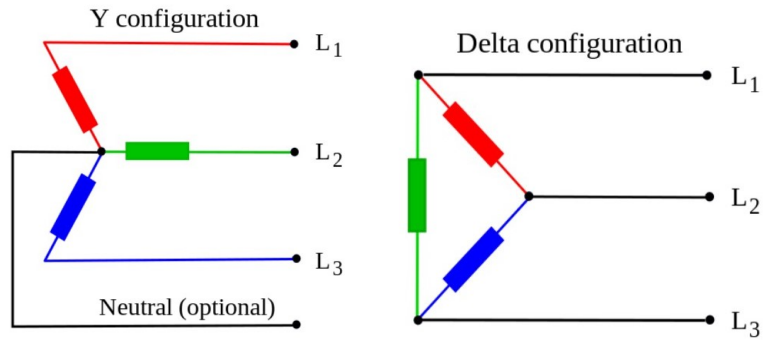


Figure 1.4: Electrical windings configuration

but with a star configuration. However, the delta configuration does not allow for an unpowered phase, so the switching logic must necessarily be different to that adopted. Therefore, in general, the star configuration is always adopted.

The core is made of soft ferromagnetic materials which allow easy magnetisation to create, in the presence of a supply current, a rotating magnetic field which, interacting with that generated by the permanent magnets of the rotor, allows the desired torque to be generated. The choice of soft ferromagnetic materials is essential as they have a very low hysteresis cycle, allowing easy implementation of positive or negative magnetisation without the effect of the previous magnetic history, making current switching perfectly feasible. Soft ferromagnetic materials also have a high magnetic permeability, which produces high values of induced magnetic field. Eddy current losses are governed by several equally shaped and overlapping foils, each electrically isolated, to prevent current flowing between the interfaces [9].

1.3.3 Working principle

The power supply to the stator circuits is no longer via the commutator and brushes used in classic permanent magnet DC motors, but via an inverter which supplies the phases according to the angular position of the rotor and to a precise power supply logic controlled by a control system. This avoids the creeping contacts typical of a brush motor, as the motor is no longer driven by the Lorentz force principle, but by the interaction of two magnetic fields, one stator generated by the electrical circuits and the other rotor generated by the permanent magnets. In fact, the two magnetic fields rotate at the same frequency trying, through the power supply control logic, to generate mutually perpendicular magnetic field lines between the stator and rotor producing maximum drive torque. The magnetic field generated is more uniform, reducing vibrations and therefore increasing the life of the component, while at the same time allowing more precise position control. The waveform characterising the counter-electromotive force of a brushless DC motor is trapezoidal. This type of motor is generally used when the performance to be achieved is not very high. Switching between the three phases of the stator takes place via the inverter and a three-phase bridge with six power transistors (with protection diodes connected), which allows only two phases to be supplied with ON-OFF control logic at a time to ensure interaction between the magnetic fields of the stator and rotor and the generation of motor torque. Switching between the various phases takes place according to the angular position of the rotor, which is evaluated using Hall effect sensors. The technique is extremely effective for high rotation speeds but is not recommended for low speeds as it would produce a discontinuity in the torque delivered, resulting in lower performance and increased vibration. In addition, an incorrect orthogonal situation between the magnetic field lines of the stator and rotor could occur, resulting in a reduction of motor torque. To effectively understand the operation of a three-phase brushless DC motor, we refer to the figure 1.5.

From the figure 1.5, the three phases of the stator are arranged in a star configuration with an angular distance of 120° to each other and each is connected to terminals through which current is supplied and switched by the inverter. In fact, initially only one pair of windings, i.e. two out of three phases, is powered, generating the respective magnetic field. At this point, the interaction between the resulting magnetic field of the stator and that generated by the permanent magnets of the rotor produces a shift in the rotor which tends to align the two fields. The power of the two phases is interrupted and supplied to two different windings. In this way, the same situation as before is repeated [9]. Whenever the power is switched between the phases, this must be done in relation to the instantaneous position of the rotor, which is measured either by the encoders (which directly calculate the angular position of the rotor) or, in the case under consideration, by Hall effect sensors. These sensors detect the orientation of the magnetic polarity of the

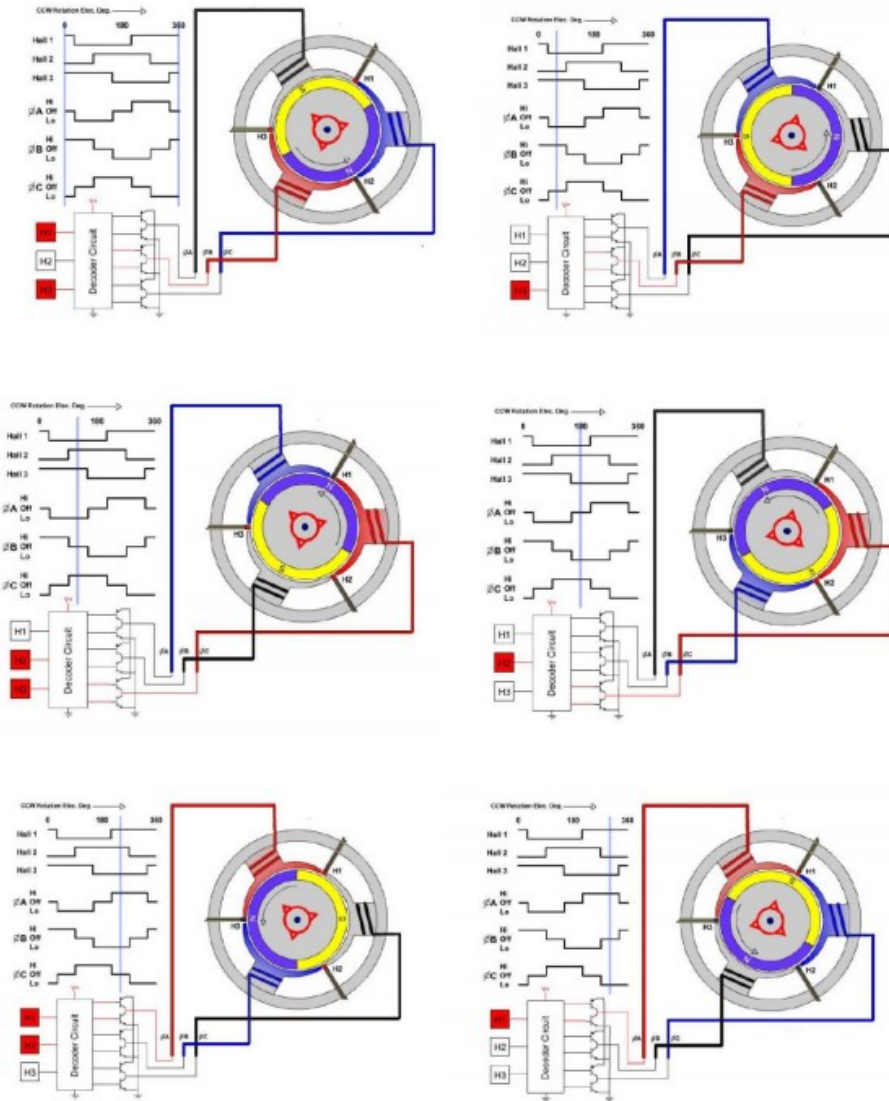


Figure 1.5: Brushless DC motor working principle [9]

permanent magnets, as they are very sensitive to changes in the direction of the magnetic flux generated by them. In fact, the shift in the electric charge defines a voltage which is evaluated at the ends of a conductor at the time of switching. This is supplied to the control system which will manage the information to produce a reference current for the correct switching of the power supply of the three phases.

1.4 Permanent magnet synchronous motor - PMSM

The power supply technique for PMSM is characterised by sinusoidal waveform voltage and 120° phase shift. The supply voltage is a function of the angular position of the rotor, which is measured, unlike the Hall effect sensors for brushless DC motors, by hollow shaft resolvers, which guarantee better discretisation. The phases are switched by means of a three-phase power transistor inverter which does not generate ON-OFF signals but sinusoidal voltages. This allows the torque generated by a PMSM is not subject to the oscillations found in brushless DC motors. The use of PMSM motors in the aerospace field is for low power applications ($0.1 - 10 \text{ kW}$) and due to their high efficiency for operation at low speeds and their high torque-to-weight ratio. The cross-section of a PMSM is shown in the figure 1.6.

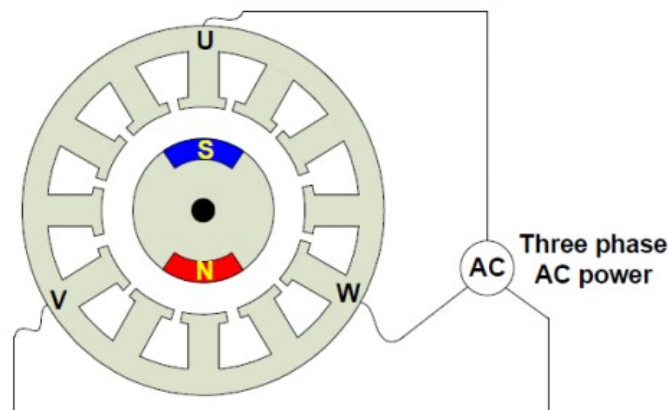


Figure 1.6: Permanent magnet synchronous motor

1.4.1 Rotor

As in brushless DC motors, the permanent magnets on the rotor are made of hard ferromagnetic materials characterised by a large hysteresis cycle and particularly high magnetic fields. The permanent magnets are oriented differently from those immediately adjacent to them, resulting in a magnetic flux density that evolves as the sine of the rotor angle. Thus, not being in a situation of mutual perpendicularity, the value of the rotor's magnetic field will have a maximum when the field lines are orthogonal between the stator and the rotor but, as one moves away from this condition, there is a reduction in the magnetic field until a maximum magnetic field of opposite sign is produced.

1.4.2 Stator

Soft ferromagnetic materials are used to construct the stator in such a way that the hysteresis cycle is very small and the magnetic field is rapidly transformed into magnetic induction with each current flow. The substantial difference with the stator of a brushless DC motor is that in this case the windings are generally distributed as sinusoidally as possible. This produces, as shown in the figure 1.7, distributed winding solutions, characterised by a higher amplitude and lower harmonics content and an almost constant rotating field.

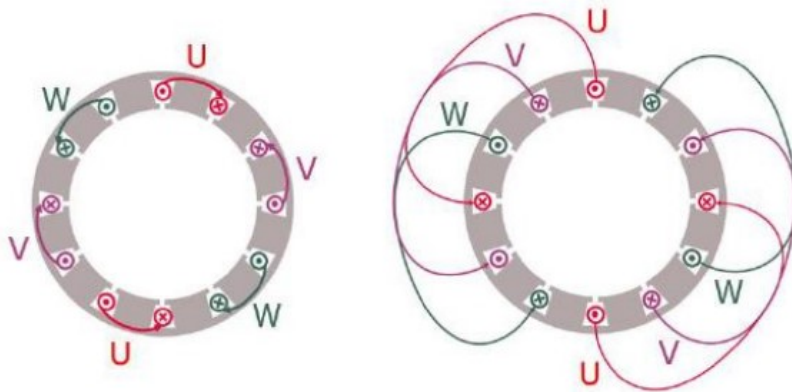


Figure 1.7: Concentrated windings and distributed windings

1.4.3 Working principle

The waveform characterising the power supply logic is sinusoidal. In this case, the phases are fed by voltages with a sinusoidal waveform and offset by 120° , ensuring interaction between the magnetic fields and smoother rotational dynamics. However, the technique has its complications when switching, as oscillations and noise occur which can generate mechanical vibrations. They are also more expensive than brushless DC motors due to their greater complexity. The operating principle involves supplying the three phases simultaneously with waves offset by 120° to create an alternating magnetic field, known as the Galileo Ferraris field, the sum of the three magnetic fields generated in the various phases [9].

Chapter 2

Test Bench Architecture

The test bench is an indispensable instrument as it allows the numerical model built using Matlab-Simulink to be validated and several tests to be conducted to verify the correct response of the servomechanism under nominal operating conditions. In addition, having a real experimental architecture available allows tuning of parameters relating to components that are not known a-priori or are unreliable. By obtaining the trends of the characteristic quantities of the system under nominal operating conditions, it is possible to generate a prognostics algorithm useful for highlighting a fault or malfunction. In addition, in the future it will also be possible to use the test bench to validate the model in the event of failure of one or more system components.

The architecture comprises two modules:

- **Actuation module**
- **Braking module**

The test bench is shown in figure 2.1 and its top view is shown in the figure 2.2.

The PMSM (Permanent Magnet Synchronous Motor), the control and power electronics were supplied by Siemens, while the gearbox and braking system were obtained using a 3D printer using the "Fused Deposition Modelling (FDM)" technique, which allows components to be developed quickly and at low cost [10]. The components supplied by Siemens are not the same as those used in aeronautics, as they have a higher weight and are used for industrial production. However, they are inexpensive and function very similarly to aerospace actuators and are suitable for the type of application described in this thesis [11].

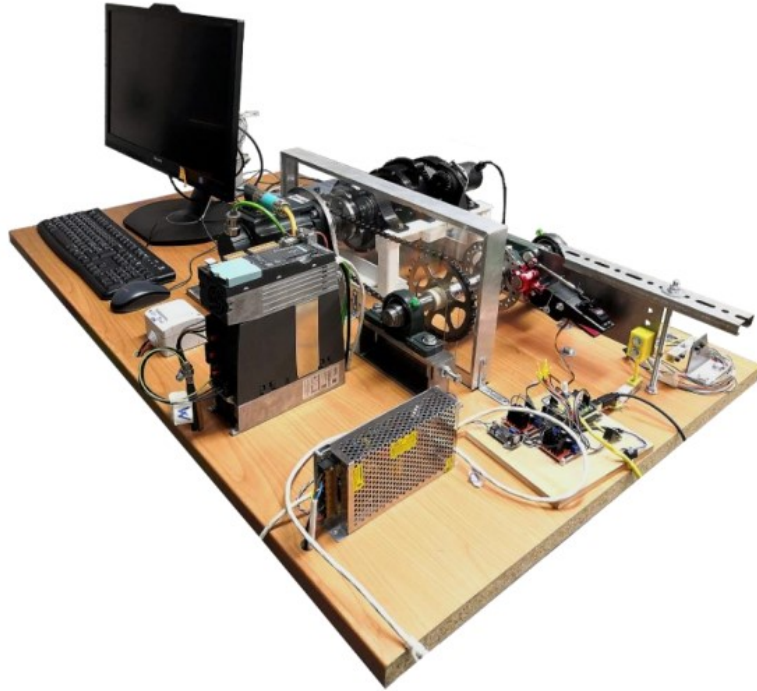


Figure 2.1: Test bench

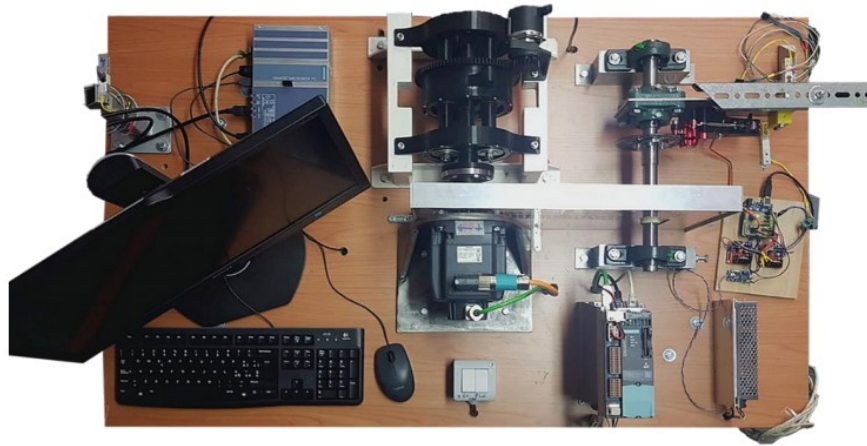


Figure 2.2: Test bench top view

2.1 Actuation module

The actuation module consists of the Microbox PC, the control electronics and the power electronics. All these components are manufactured by Siemens and control the motor drive, which is connected via the output shaft to the planetary gearbox

Basic Data	
Power supply	24 V DC (-20%/+20%) max 4 A
Processor	Intel Core i3-6102E Processor (3M Cache, 1.9 GHz)
Main Memory	16 GB DDR4-SDRAM SODIMM
Operative system	Windows Embedded Standard 7 SP1, 64 bit
SSD (Solid State Disk)	128 GB SATA
Graphic	HD graphic onboard
Installation	Installation on DIN rail, wall mounting/vertical mounting
Free slots for expansion cards	Up to 2xPCIe cards

Table 2.1: Basic Data

Ports	
Serial	COM1/COM2 (RS 232, RS 422, RS 485 configurable)
USB ports	4xUSB V3.0 (high current)
Ethernet ports	3xGbit Ethernet
Keyboard, mouse	Connected via external USB port
Graphics	2 x DisplayPort DPP (DVI via DP++ to DVI adapter possible)

Table 2.2: Ports

2.3 SINAMICS Control Unit

The CU310-2 PN (PROFINET) control unit manages the regulation and control of the Blocksize Power Modules via the PM-IF interface, as it is mounted directly on the Power Module. The Power Module Chassis are controlled by the control unit via the DRIVE-CLiQ interface mounted directly above the power module in a cable-free connection. The memory card (Compact Flash Card) contains the parameters for the operation of the control unit, which is inserted into a special slot (CF). This device is powered at 24 V DC and can perform both open and closed loop control logics. It is connected to the Microbox PC via an Ethernet cable and to the electric motor via a DRIVE-CLiQ signal cable. This device is connected directly to a PC bypassing the connection to the Microbox PC for time domain simulations. For simulations in the frequency domain, it is connected directly to the Microbox and to a PC via an Ethernet cable [12].



Figure 2.4: Control unit CU310-2 PN (PROFINET)

2.4 SINAMICS Power Module

The PM240-2 power module supplies the motor windings according to the information given by the control unit. The power supply of the power module, through which the electric motor is powered following the information from the control unit, is three-phase 380 V AC [13].



Figure 2.5: Power module PM240-2

The component has the following characteristics:

- Line-side diode rectifier
- DC-link electrolytic capacitors with pre-charging circuit
- Output inverter
- Braking chopper for (external) braking resistor
- Gating unit, actual value acquisition
- Fan to cool the power semiconductors

Some of main characteristics are reported in the table 2.3.

Rated Data	
Input	
Number of phases	COM1/COM2 (RS 232, RS 422, RS 485 configurable)
Line Voltage	4xUSB V3.0 (high current)
Line frequency	3xGbit Ethernet
Rated current (LO)	Connected via external USB port
Rated current (HO)	2 x DisplayPort DPP (DVI via DP++ to DVI adapter possible)
Output	
Number of phases	3 AC
Rated voltage	400 V
Rated current (LO)	32.00 A
Rated current (HO)	26.00 A
Max. output current	52.00 A
Rated power IEC 400V (LO)	15.00 kW
Rated power NEC 480V (LO)	20.00 hp
Rated power IEC 400V (HO)	11.00 kW
Rated power NEC 480V (HO)	15.00 hp
Pulse frequency	4 kHz
Output frequency for vector control	0 ... 200 Hz
Output frequency for V/f control	0 ... 550 Hz

Table 2.3: Rated Data

2.5 SIMOTICS Synchronous Motor

The test bench features a SIMOTICS S 1FK7060-2AC71-1CG0 synchronous motor developed by Siemens.



Figure 2.6: SIMOTICS S 1FK7060-2AC71-1CG0 synchronous motor

The motors belonging to class 1FK7 are permanent magnet synchronous motors characterised by a high compactness and allow cooling by heat dissipation through the surface of the motor walls. The heat generated by various factors, such as eddy currents or friction losses, must be dissipated to allow the motor to operate correctly and avoid potential overheating. The type of motor adopted allows self-cooling up to an ambient temperature of $40^{\circ} C$, so the correct operation of the motor depends on the efficiency of cooling, which can be natural, by forced ventilation or liquid cooling [14]. The diagram in the figure 2.7 shows the trend of the torque delivered by the motor, decreasing as the angular speed increases, used for the test bench whose windings can operate in perfect working conditions up to a temperature of $145^{\circ} C$.

The continuous operation of the electric motor depends on the permissible temperature range. Class "S1 (100 K)" in the graph delimits the permissible temperature range and corresponds to a thermal class F ($155^{\circ} C$). It is possible to follow the temperature range provided by class "S1 (60 K)" corresponding to a thermal class B ($130^{\circ} C$) if the housing temperature must be below $90^{\circ} C$ or if an excessive increase in temperature would pose a risk to motor operation. Intermittent operation, whose limits are represented by the classes "S3 25%", "S3 40%", "S3 60%" and Mmax, provides for the possible application of a higher load on the motor but with duty cycles of ten minutes and overtemperatures set at 100 K. In addition, it is possible to operate in transient mode throughout the permissible speed range but not exceeding the "Mmax" limit and with high permissible overtemperatures. In addition to the thermal operating limits to be respected, the physical limits of the motor must also be respected. From the graph in figure 2.7, the mechanical limit represented by "nmax-mech" imposes the admissible speed range linked to the

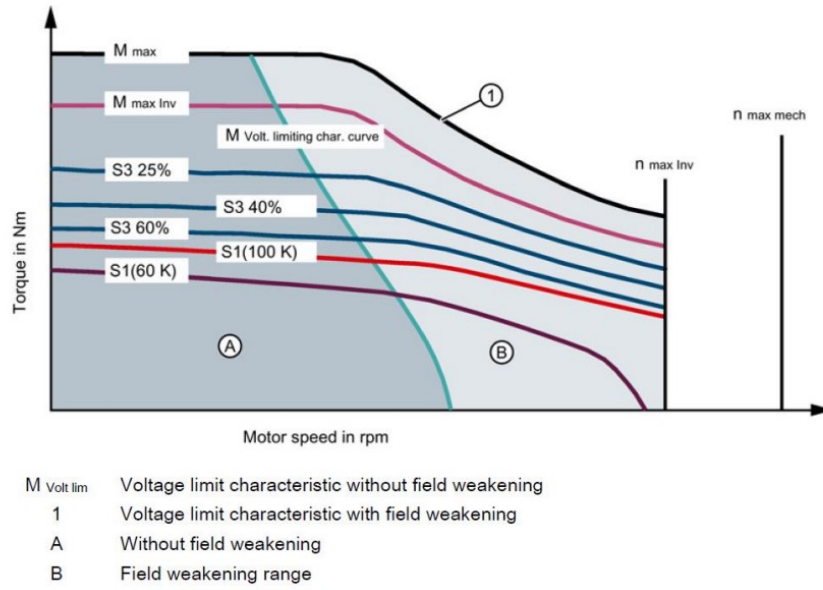


Figure 2.7: Torque characteristics synchronous motor

centrifugal forces of the rotor and the life of the bearings, while the limit represented by "nmax-inv" imposes the maximum intensity and the maximum frequency of the converter. The maximum operating speed of the motor must not exceed these limits. The simulations performed on the test bench also include an external torque applied to the motor which represents the action of the aerodynamic forces on the control surface. The "Siemens starter" software and the "Trace" software respectively enable the behaviour of the motor's characteristic quantities during operation to be analysed and visualised. The main characteristics of the electric motor are shown in the tables 2.4, 2.5, 2.7, 2.6.

Engineering Data	
Rated speed (100 K)	2000 rpm
Number of poles	8
Rated torque (100 K)	5.3 Nm
Rated current	3.0 A
Static torque (60 K)	5.0 Nm
Static torque (100 K)	6.0 Nm
Stall current (60 K)	2.55 A
Stall current 100 K)	3.15 A
Moment of inertia	7700 $kgcm^2$
Efficiency	90.00%

Table 2.4: Engineering Data of the electric motor

Physical constants	
Torque constant	1.1 Nm/A
Voltage constant at 20°C	121.0 V/1000 · min ⁻¹
Winding resistance at 20°C	2.75 Ω
Rotating field inductance	30.5 mH
Electrical time constant	11.10 ms
Mechanical time constant	1.75 ms
Thermal time constant	30 min
Shaft torsional stiffness	40500 Nm/rad
Net weight of the motor	7.1 kg

Table 2.5: Physical constants of the electric motor

Mechanical Data	
Motor type	Permanent magnet synchronous motor
Shaft height	63
Cooling	Natural cooling
Radial runout tolerance	0.040 mm
Concentricity tolerance	0.10 mm
Axial runout tolerance	0.10 mm
Vibration severity grade	Grade A
Connector size	1
Degree of protection	IP64
Temperature monitoring	Pt1000 temperature sensor
Electrical connectors	Connectors for signals and power
Holding brake	No holding brake
Shaft extension	Plain shaft
Encoder system	Encoder AM24DQI: absolute encoder 24 bits (resolution 16777216, encoder-internal 2048 S/R) + 12 bits multi-turn (traversing range 4096 revolutions)

Table 2.6: Mechanical Data

Optimum Operating point	
Optimum speed	2000 rpm
Optimum power	1.1 kW
Limiting Data	
Max permissible speed (mech.)	7200 rpm
Max permissible speed (inverter)	4750 rpm
Maximum torque	18.0 Nm
Maximum current	10.7 A

Table 2.7: Data of the electric motor

2.6 Reduction gearbox

The component was developed and produced entirely by the Politecnico di Torino using the "Fused Deposition Modelling (FDM)" additive manufacturing technique [15]. The planetary gearbox is connected to the crankshaft via an elastic joint and enables the mechanical power generated to be transmitted to the user while reducing weight and dimensions. The component is necessary to increase, with the same mechanical power developed, the torque delivered by the motor by reducing the angular speed at the output of the motor shaft. The figure 2.8 shows the structure of the planetary gearbox.

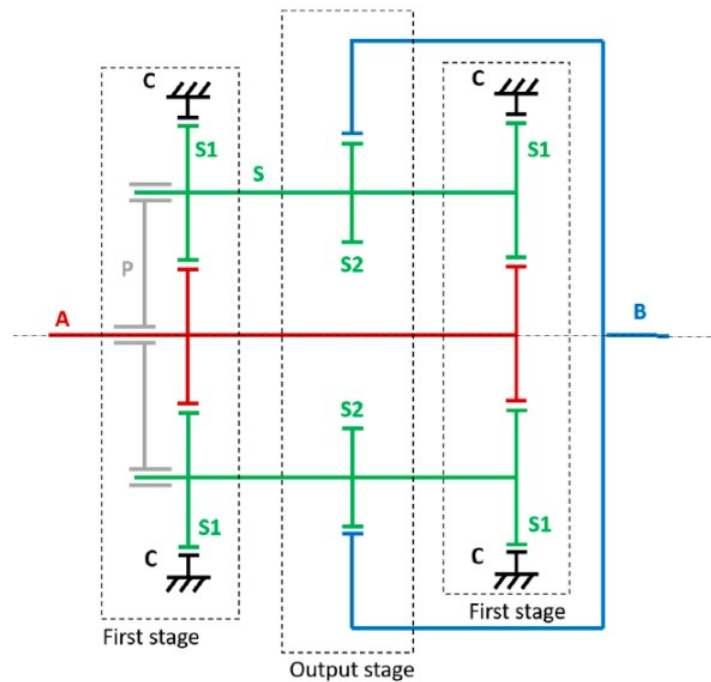


Figure 2.8: Reduction gearbox

The structure is characterised by four shafts and three internal gears. In particular, the central gear, called the sun gear, is rotated by the drive shaft to which it is connected. The sun gear consists of three spacers and two gearwheels with mirrored teeth, connected to the crown gear marked C and with a fixed number of teeth equal to Z_A . The sun gear rotates three other shafts, called planet gears, to which they are connected, consisting of two spacers and three gear wheels. The latter have a connection to the sun gear with the number of teeth equal to Z_{S1} while they are connected to the crown gear B through the number of teeth equal to Z_{S2} as shown in the figure 2.9. The central wheels of the planetary gears have a double helical toothing, while those at the ends have a specular tooth angle. The fixed gear wheels

marked C are used to connect the gear unit to the alloy steel support structure. The planetary gearbox under consideration has a first planetary stage mirrored to the output stage to ensure the balance of forces discharged on the satellites, making it unnecessary to use a carrier as it would not absorb forces or torque. The helical teeth can absorb axial loads in both directions and, moreover, by presenting opposite helix angles on the two end stages and herringbone teeth on the central stage, make all the shafts self-supporting, avoiding the use of mechanical bearings [16]. The effect of the gearbox on speed can be analysed by considering the radius of the gears of the first stage and the output stage. In fact, since the number of teeth of the first stage gears is different from the number of teeth of the output stage, the output speed V_B will not be equal to the peripheral speed V_A . Therefore, it is possible to evaluate the speed V_B using the equation 2.1:

$$V_B = V_A \frac{r_{S1} - r_{S2}}{2r_{S1}} \quad (2.1)$$

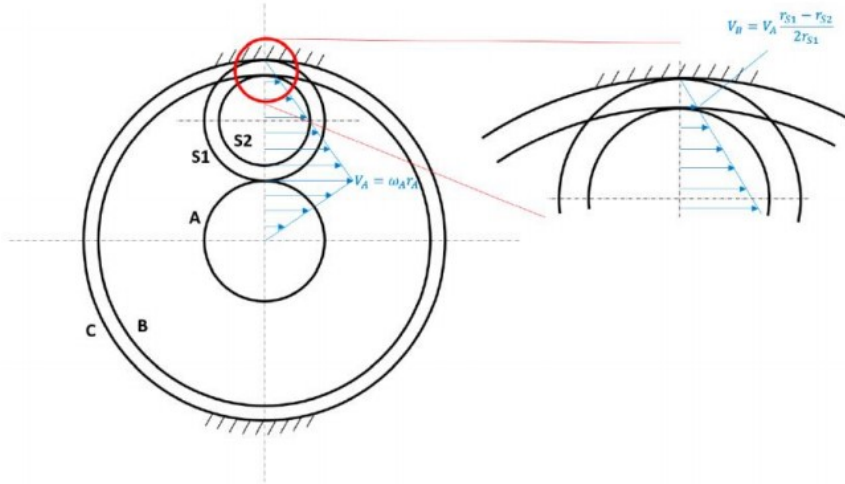


Figure 2.9: Speed profile

It is possible to calculate the transmission ratio from the input shaft A to the output gear B using the Willis formula, which involves using the gear ratio and the number of teeth of each gear [17]. Assuming the observer is fixed on the planet carrier, we can calculate the gear ratio between the input shaft A and the output shaft B as described in equation 2.2:

$$\tau_1 = \frac{\omega_A - \Omega}{\omega_B - \Omega} = -\frac{z_B z_{S1}}{z_A z_{S2}} \quad (2.2)$$

in which Ω is the angular speed of the planet carrier. The transmission ratio evaluated between the input port A of the shaft and the fixed gears:

$$\tau_2 = \frac{\omega_A - \Omega}{\omega_C - \Omega} = -\frac{z_C}{z_A} \quad (2.3)$$

Since $\omega_C = 0$ (fixed gears) the gear ratio in the fixed reference system will be:

$$\tau = \frac{\omega_A}{\omega_B} = \frac{1 + \frac{z_A}{z_C}}{\frac{z_A}{z_C} - \frac{z_A z_{S2}}{z_B z_{S1}}} = \frac{1 + \frac{z_C}{z_A}}{1 - \frac{z_C z_{S2}}{z_B z_{S1}}} \quad (2.4)$$

The inertia of the input shaft was initially evaluated considering unit length and density, and the inertia of the wheels was assumed to be equal to that of the respective primitive cylinder. Therefore, the inertia of the shaft will be:

$$I_A = \frac{1}{2} M_A r_A^2 \quad (2.5)$$

in which M_A is the mass and r_A is the radius of the solar gear.

Subsequently, the inertia of the output shaft was evaluated by considering an outer radius 20% larger than that of the primitive radius:

$$I_B = \frac{1}{2\tau^2} M_B ((2.1r_B)^2 + r_B^2) \quad (2.6)$$

in which M_B is the mass and r_B is the radius of the output shaft. In this case, if one wanted to refer to the input shaft, one would have to divide by τ^2 . The inertia of the satellite gear has been calculated and referred to the input shaft:

$$I_{S,A} = \frac{I_S}{\tau_S^2} + \frac{M_S r_p^2}{\tau_p^2} \quad (2.7)$$

in which: M_S represents the mass of the satellites and the planetary shaft, $\tau_S = \omega_A/\omega_S$, $\tau_P = \omega_A/\omega_P$ and r_P is the radius of the virtual planet carrier.

The table 2.8 shows the data for the planetary gearbox.

Planetary Gearbox Data	
Number of teeth ZA	21
Number of teeth ZS1	21
Number of teeth ZS2	20
Number of teeth ZC	63
Number of teeth ZB	62
Degrees of freedom	1
Reduction ratio	124
Total inertia reduced to A	$1750 \text{ g} \cdot \text{mm}^2$

Table 2.8: Data of Planetary Gearbox

2.7 Encoder

The encoder used is the high-resolution optical incremental model TSW581HS.M2.5000.5.V.K4.B127.PL10.PP2-5. The encoder translates information on the position and angular speed of the motor shaft into an electrical signal to be sent to the control unit, which then implements a closed-loop control logic.



Figure 2.10: Encoder

The incremental encoder works by using a disc mounted on the motor shaft and characterised by transparent and opaque zones. A beam of light from photo emitters is passed through these zones and detected by a photo detector mounted on the opposite side. The light signal will result in an output logic signal of 1 if the light beam is detected and 0 otherwise. The incremental encoder generates two quadratic waveforms offset by 90° called channel A and channel B. The reading of the single channel A allows the angular displacement of the motor shaft to be evaluated, while the reading of both channels also evaluates the direction of rotation. A third channel, called Z channel and also characterised by a quadratic pulse, allows to verify the completion of one revolution of the motor. The encoder is fixed on the support of the planetary gearbox and communicates with the output crown. The table 2.9, 2.10, 2.11 show the main characteristics of the incremental encoder.

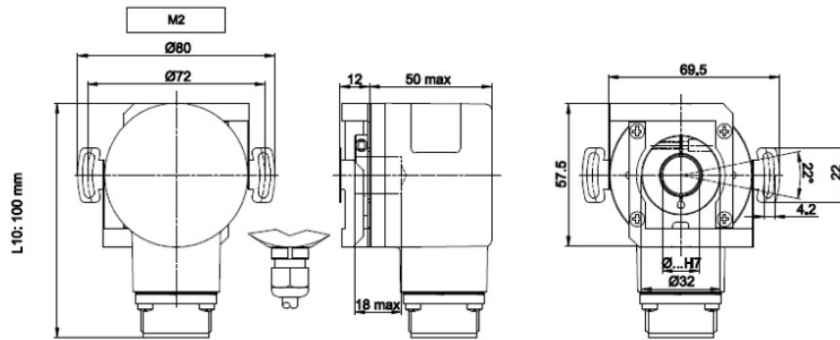


Figure 2.11: Encoder's dimensions

Order code Encoder		
TSW581HS.M2.5000.5.V.K4.B127.PL10.PP2-5		
Name	Code	Meaning
Model	TSW581HS	Bidirectional + index
Assembly	M2	M2 spring type
Pulse Rate	5000	5000
Power Supply	5	5 V ± 5%
Output frequency	V	From 0 a-up to 300 kHz
Protection Degree	K4	IP64 (EN60529)
Shaft	B127	12.7 mm of diameter
Electrical connection	PL10	Radial cable gland with cable of 1 meter length
Output circuits	PP2-5	Push-Pull 5V output only

Table 2.9: Data of the Encoder

Materials	
Flange	Non corroding Aluminium
Housing	Polyamid 6 (PA6)
Shaft	Stainless steel
Environmental Specifications	
Operation temperature range	-10°C / + 70°C
Storage temperature range	-30°C / + 85°C
Relative humidity	98% RH without condensing
Vibrations	10 g (from 10 up to 2000 Hz)
Shock	20 g (for 11 ms)

Table 2.10: Encoder materials

Mechanical specifications	
Shaft rotation speed	6000 rpm continous
Starting torque at 25°C	0.025 Nm
Bearings life	5· 10 ⁹ revolutions (minimum)
Moment of inertia	40 <i>gcm</i> ²
Weight	~ 0.25 kg
Electrical Specifications	
Synchronous index outpu	Default on channel A; A+B optional
Supply current without load	150 mA max
Protection	Short circuit protection (only output LD2 and PP2) against inversion of polarity (except 5V, 5/28 V)

Table 2.11: Encoder Mechanical specifications

2.8 Braking module

The braking module makes it possible to simulate the action of external aerodynamic loads on the control surface of the actuator during flight. In particular, the external load will be a braking torque applied to the motor shaft. Among the various elements that make up the braking module, we find the brake shaft, made of alloy steel, placed parallel to the motor shaft and supported by two self-aligning bearings that allow its rotation. On the brake shaft there is a pinion connecting the drive module with the braking module and the brake disc with holes distributed to allow cooling by heat dissipation and, finally, a rectangular plate interposed between two standard self-aligning bearings. The plate supports the brake caliper and transfers the braking load to the load cell, which is connected to the Arduino board on the test bench. The brake caliper features circular magnetic pads typical of the cycling industry, while the servomotor comes from the model-making industry. The two devices are interfaced by a steel tie rod which enables the braking system to be activated. In particular, the rotation of the servomotor activates the tie rod that brings the pads into contact with the brake disc through a lever on the brake caliper. In this way, a friction-generated braking action is exerted on the disc to decelerate the drive shaft. Similarly, releasing the brake caliper lever moves the magnetic pads away from the disc, cancelling the braking action of friction. To evaluate the braking torque, the braking load must be transferred to the load cell connected to the Arduino board. To do this, a support made using the "Fused Deposition Modelling (FDM)" technique is used through a 3D printer that transfers the braking load from the rectangular plate to the load cell. The load cell deforms under the effect of the braking load, changing the length of the electrical wires inside it and thus changing their electrical resistance, which is evaluated by the Arduino board. This signal is used to calculate the force that pulls on the cell and by multiplying this value by the distance between the point of application of the load and the axis of rotation of the brake shaft it is possible to calculate the overall braking torque.

2.9 Servomotor

The main characteristics of the servomotor used in the test bench architecture are shown in the table 2.12.

Digital Servo DM5163M	
Dimensions	40x20x37 mm
Torque (@ 4.8 V)	15.5 Kgcm
Torque (@ 6.0 V)	16.3 Kgcm
Speed (@ 4.8 V)	0.15 s/60°
Speed (@ 6.0 V)	0.13 s/60°
Weight	58 g
Bearings	2
Motor	DC
Voltage	4.8-6 V

Table 2.12: Data of the Servomotor

The power supply for the servomotor is provided by a converter that transforms the 24 V DC voltage into 6 V DC.

2.9.1 Arduino code

The code implemented using the "Arduino R3" board allows closed loop control logic to be implemented to control the braking force to be applied to the brake caliper according to the signal in the angular position that is to be commanded to the servomotor. A potentiometer connected to the Arduino board provides an input command corresponding to the braking load to be imposed called "set". At this point, the "command" signal corresponding to the load applied on the brake shaft of the braking system is measured in absolute value. The signal is supplied to the load cell and the error between the commanded signal and the signal applied to the braking system is calculated:

$$error = set - load \quad (2.8)$$

The error is supplied to a PID controller which provides both proportional and integrative control input.

- **Proportional contribution**

$$y_P = GP \cdot error \quad (2.9)$$

- **Integrative contribution**

$$y_I = GI \cdot \int error dt \quad (2.10)$$

- **Total contribution**

$$y = y_P + y_I \tag{2.11}$$

Using the "STARTER" software, it was possible to derive a function that would allow the relationship between the braking force applied and the angular position commanded to the servomotor to be expressed. Various simulations were performed, imposing an angular speed of 100 rpm on the motor, and a potentiometer was used to measure the braking force expressed in [gf] as a function of the angular position expressed in [deg]. The figure 2.12 shows the trend.

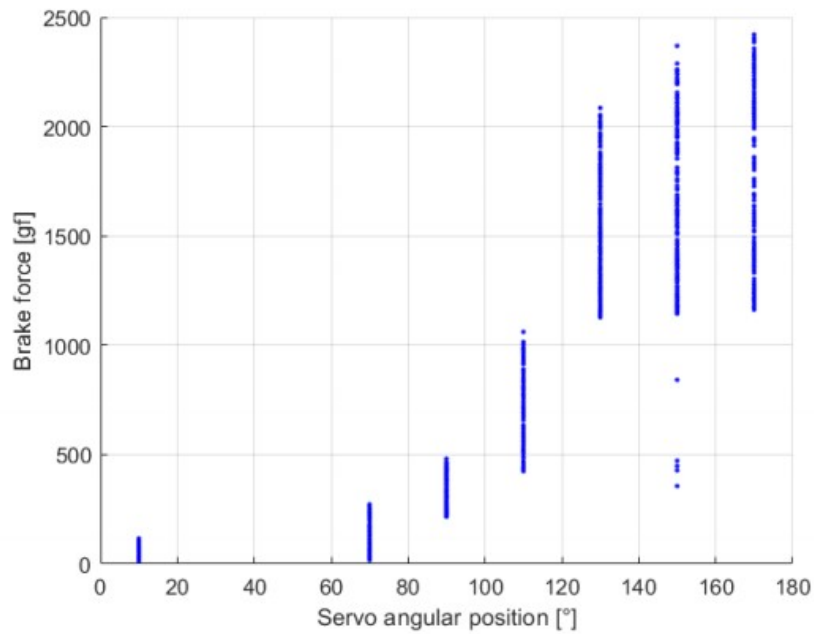


Figure 2.12: Braking load trend

The mathematical relationship approximating the trend of the points was then extrapolated and the standard deviation highlighted.

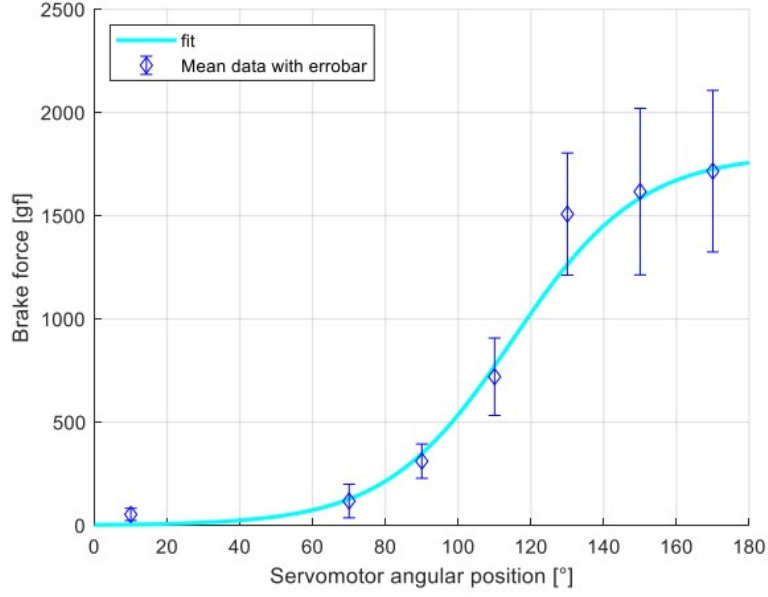


Figure 2.13: Fitting data

From the figure 2.13, it can be seen that as the servomotor angle increases, the braking force also increases. The equation 2.12 describes the trend as follows:

$$brakeforce = \left(\tanh \left(\frac{angularposition - 115}{35} \right) + 1 \right) \cdot 900 \quad (2.12)$$

From the equation 2.12, the inverse formula is derived expressing the angular position of the servomotor as a function of the braking load applied as described in the equation 2.13.

$$angularposition = \frac{35}{2} \log \left(\frac{brakeforce}{1800 - brakeforce} \right) + 115 \quad (2.13)$$

Finally, the condition reported in the inequation 2.14 introduce the limit of angle excursion assumed for the servomotor:

$$0^\circ < angularposition < 180^\circ \quad (2.14)$$

2.10 Transmission system

The drive module consists of a drive chain connecting the drive module with the brake module. The chain is made up of rollers and supported by two toothed wheels installed one on the drive shaft and the other on the brake shaft. This system makes it possible to introduce a transmission ratio between the two modules so as to make the system operate as close as possible to real operation. The transmission chain allows the tensioner to be operated by adjusting the play between the sprockets, adding a delay in the transmission of torque, which is a characteristic of a real motor and which must be controlled in closed loop to avoid instability. The components of the architecture are analysed in more detail below.

2.11 Roller chain

The transmission chain makes it possible to transfer the torque generated by the drive shaft to the brake shaft by rotating the latter and to transfer the braking torque to the drive shaft. The chain is a classic roller chain generally used in the cycling industry and consists of links connected by two pins and composed of two rollers. The rollers on bushings are pressed onto the internal connecting plates. The friction generated between the teeth of the sprocket and the rollers of the chain is very low, so the wear and noise generated do not compromise the correct functioning of the system.

2.12 Sprockets

The geometrical characteristics of the two sprockets are shown in the table 2.13.

Sprockets	
Motor sprocket	
Diameter	142 mm
Teeth number	34
Brake sprocket	
Diameter	90 mm
Teeth number	23

Table 2.13: Data of the Sprockets

It is possible to calculate the transmission ratio by the equation 2.15:

$$transmissionratio = \frac{Z_{motorsprocket}}{Z_{brakesprocket}} = \frac{\omega_{motorsprocket}}{\omega_{brakesprocket}} = \frac{34}{23} = 1.48 \quad (2.15)$$

The angular speed of the braking shaft is lower than that of the electric motor, while the torque is higher. In this way, the braking system works within its operating range, allowing several bench tests to be performed. In fact, the stall torque of the motor is of the order of 6 Nm while the torque produced by the braking system is of the order of $20 - 30 \text{ Nm}$ which, thanks to the transmission ratio, transfers a lower braking torque to the motor than that which is instantaneously applied.

2.13 Tensioner

The tensioner is used to transmit mechanical power by increasing or reducing chain tension. It consists of an L-shaped steel plate resting on one of the two brake shaft bearings. An M8 screw inserted on the side surface of the tensioner adjusts the chain tension. By tightening the screw it is possible to make the plate move horizontally, thus moving the bearing that supports the brake shaft.

Chapter 3

Brushless DC Motor

3.1 High-Fidelity model description

The Matlab-Simulink numerical model in the following describes the operation of an actuation system with an intermediate response time between a primary and secondary flight command. In this way, it is possible to predict and examine the responses of the system, ensuring a direct correlation with the real operation of the system whether it is implemented on primary or secondary flight commands. In addition, the high level of detail that characterises the numerical model makes it possible to develop highly accurate prognostic algorithms capable of identifying and predicting possible failures before they have serious consequences.

The numerical resolution settings of the model involve the implementation of the Euler method (in Simulink *ode1 (Euler)*) with fixed step, which represents the first-order Runge-Kutta integration method. This method allows first-order differential equations to be solved by imposing initial conditions. Furthermore, the Euler method reduces the computational cost of the simulation as it requires one single function evaluation for each calculation cycle. The time integration step for the simulation is set at 10^{-6} s as the latter must be less than the characteristic time of the whole system in order to guarantee numerical convergence.

The figure 3.1 represents the High-Fidelity (HF) project built in Simulink which models the operation of a brushless DC motor.

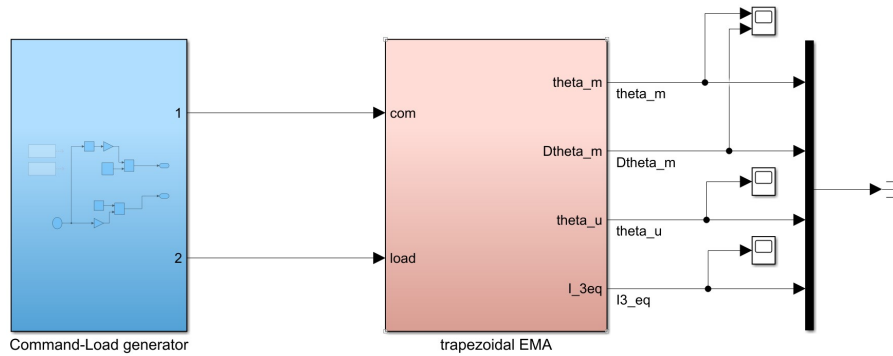


Figure 3.1: HF model

The "Command-Load generator" subsystem allows the input of the command signal in the angular position of the mobile surface to be driven and the external load expressed as a torque (corresponding to the action of the aerodynamic forces acting on the mobile surface). Both inputs are chosen by the user and sent to the "trapezoidal EMA" subsystem which implements the electromechanical dynamics of the motor through several subsystems shown in the figure 3.2.

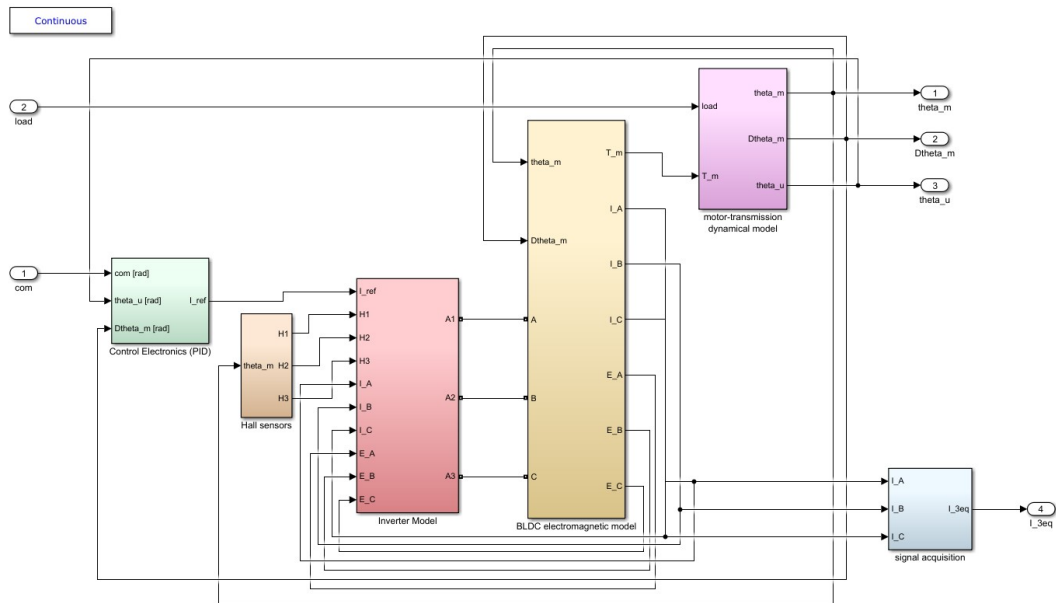
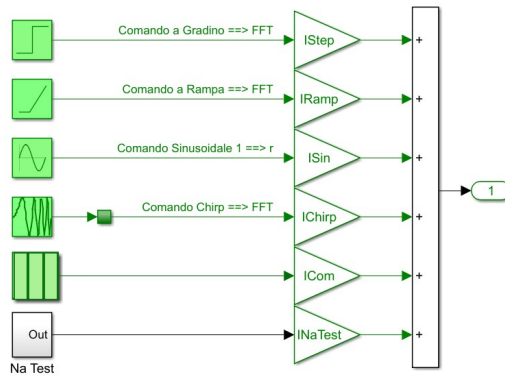
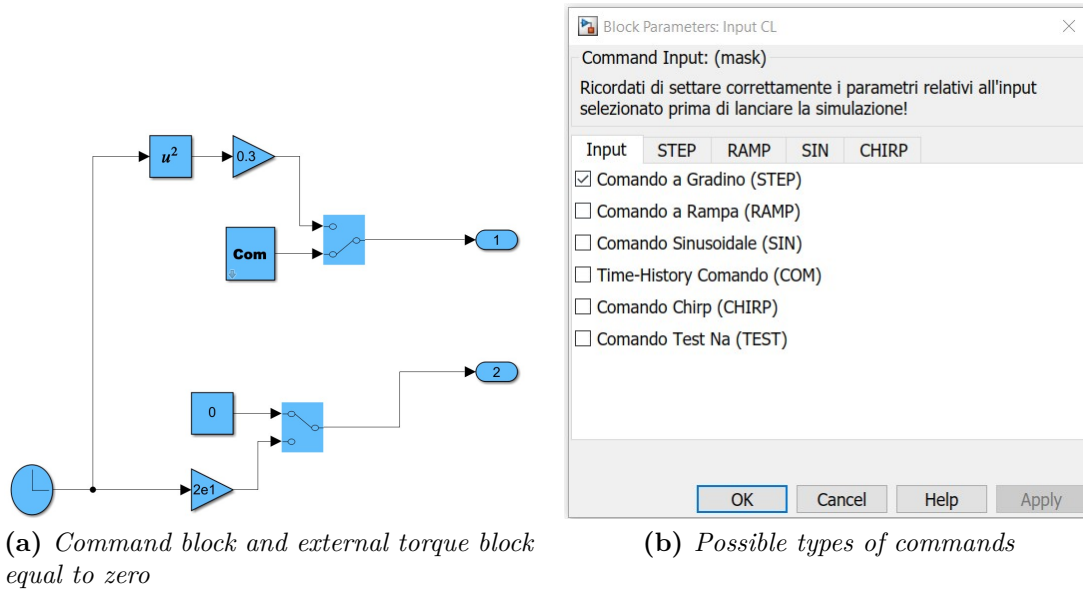


Figure 3.2: HF model subsystems

The "Com" command signal enters the input of the "Control Electronics (PID)" subsystem which, receiving also angular position of the user and angular speed of the motor, produces a reference current according to the input signals and the PID controller settings. The current produced enters the input of the "Inverter Model"

subsystem, which models the PWM (Pulse Width Modulation) supply logic of the transistors used in the three-phase bridge and the three-phase stator circuit. The subsystems "Inverter Model" and "BLDC electromagnetic model", the latter implementing the electromagnetic effects on the stator windings, produce the voltage and current signals characteristic of each stator phase, the corresponding counter-electromotive force, and the resulting motor torque of the electric motor. The latter is an input signal of the "motor transmission dynamic model" subsystem which, together with the external "load" supplied by the user, produces the angular position signals of the motor and user and the angular speed of the motor. The "Signal acquisition" subsystem receives as input the currents circulating on each stator phase and calculates the equivalent quadrature current.

3.2 Command and external torque block



(c) Blocks of commands

Figure 3.3: Command and external torque block

It is possible to set two different types of commands. The "Com" block allows you to choose between different input commands via a mask as shown in the figure 3.3. The commands that can be entered are step, ramp, sine command, chirp command or time history directly set by Matlab. The external load acting on the moving surface of the actuator is modelled using a "Clock" and multiplying this signal by a gain to have an external action that lasts for a time equal to the simulation time. Alternatively, an external load equal to zero can be set.

3.3 Control Electronics PID subsystem

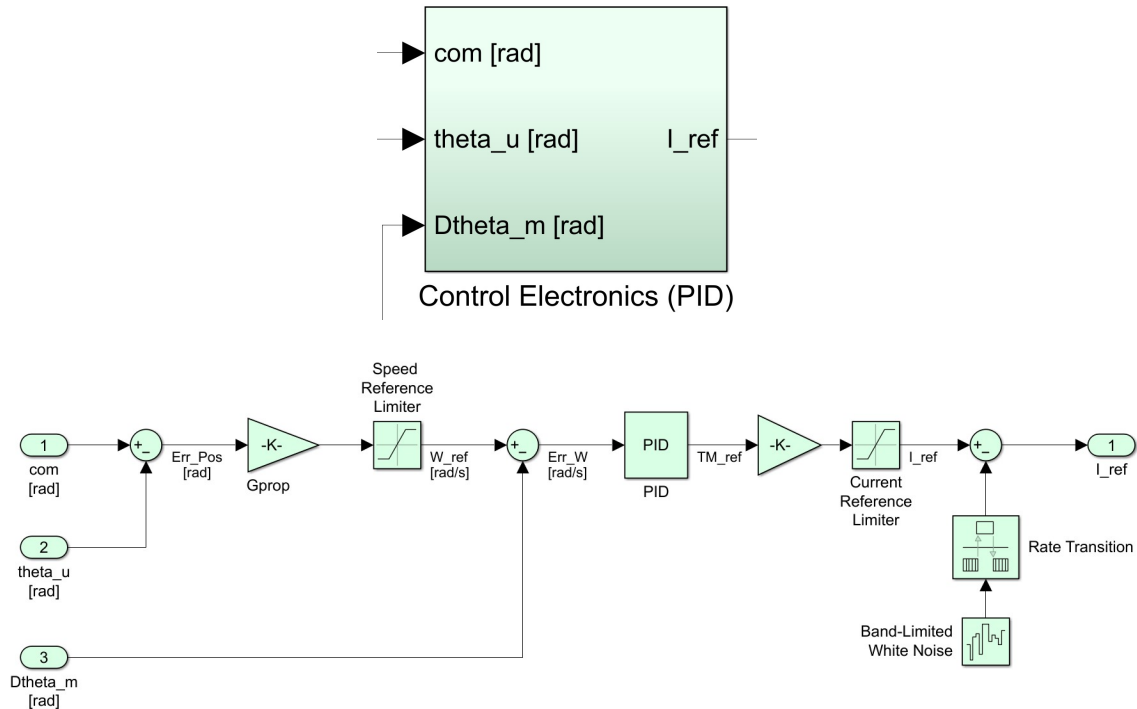


Figure 3.4: Control Electronics PID subsystem

The input angular position command is compared through a sum block to the angular position of the user (both signals are referred to the slow shaft) to obtain the position error signal. The latter is multiplied with a proportional gain to obtain the reference speed on the fast shaft and then saturated according to the maximum angular speed that the motor can deliver. The reference angular speed is compared with the instantaneous angular speed of the motor, generating a speed error. The latter goes to the input of the PID controller, the diagram of which is shown in the figure 3.5.

The PID controller receives the angular velocity error as input and multiplies it by three different characteristic gains.

- The GAP proportional gain works by producing a control signal proportional to the error.
- The gain on the integrative branch GAI works on the time history of the error producing a control that cancels out an error that remains non-zero over time.
- The gain on the derivative branch GAD, with a low-pass filter attached to eliminate any external noise, produces an action proportional to the derivative

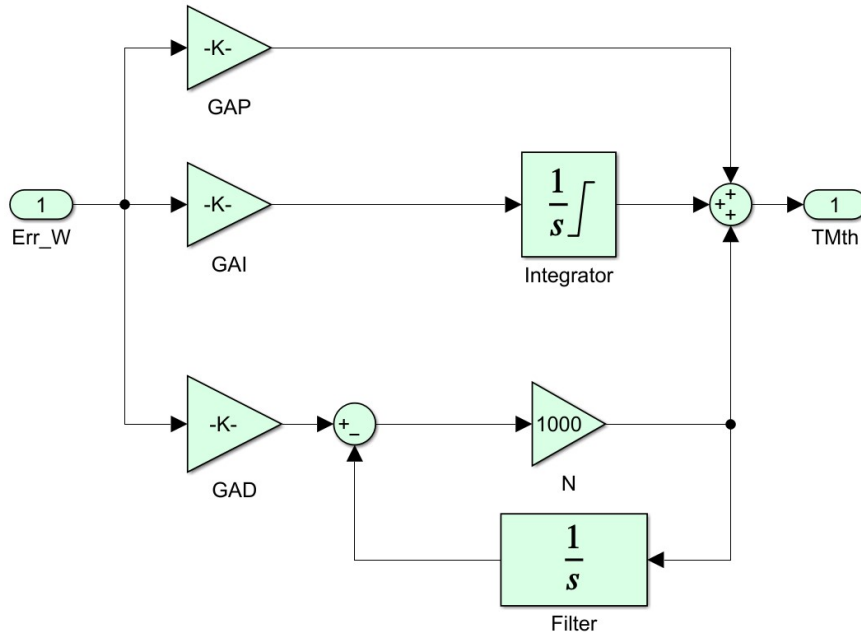


Figure 3.5: PID

of the error, making it possible to anticipate a sudden increase in the error and to damp it.

The signals coming from the three respective gains are added together to obtain the theoretical motor torque and this is the output of the PID subsystem. The reference motor torque is multiplied by a gain related to the constant counter-electromotive force of the motor to obtain the reference current. Subsequently, the current signal is saturated to avoid short-circuiting of the circuit due to potential overheating. The current signal output from the saturation block is compared with a signal generated by the "Band-Limited White Noise" block, which produces a fluctuation of the signal frequency (but in this case it is set to zero). The output of the "Control Electronics PID" subsystem is the single-phase reference current signal I_{ref} .

3.4 Hall sensors subsystem

In the "Hall sensors" subsystem, the mechanical signal of the angular position of the motor is converted into the corresponding electrical signal. The formula 3.1 is used:

$$\vartheta_e = N_p \vartheta_m \quad (3.1)$$

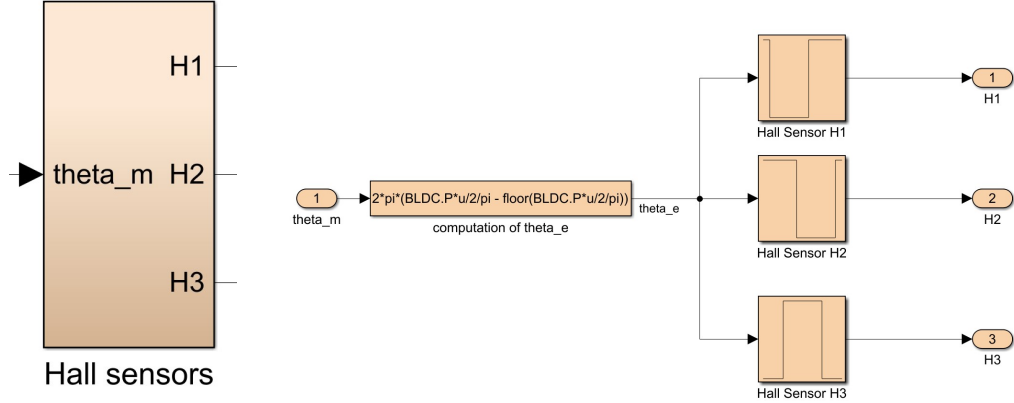


Figure 3.6: Hall sensors subsystem

in which N_P is the number of motor pole pairs, ϑ_e is the electrical angle and ϑ_m is the mechanical angle. The expression given in the "computation of ϑ_e " block makes it possible to obtain an output signal ϑ_e always between 0 and $2\pi \text{ rad}$. The equation 3.2 is used:

$$\vartheta_e = 2\pi \left(\frac{N_P \vartheta_m}{2\pi} - \text{floor} \left(\frac{N_P \vartheta_m}{2\pi} \right) \right) \quad (3.2)$$

Once the ϑ_e signal has been converted into an electrical signal, it passes through three "lookup" blocks that implement the Hall effect sensors' operating logic. These allow the generation of signals corresponding to the switching ON-OFF of the sensors by means of Boolean signals respectively 1 or 0, controlled by appropriate phase-shifted square-wave functions that simulate, depending on the position of the rotor (evaluated every 30°), the switching of the stator phases.

3.5 Inverter Model subsystem

The "Inverter Model" subsystem contains several subsystems through which the action of the inverter is modelled.

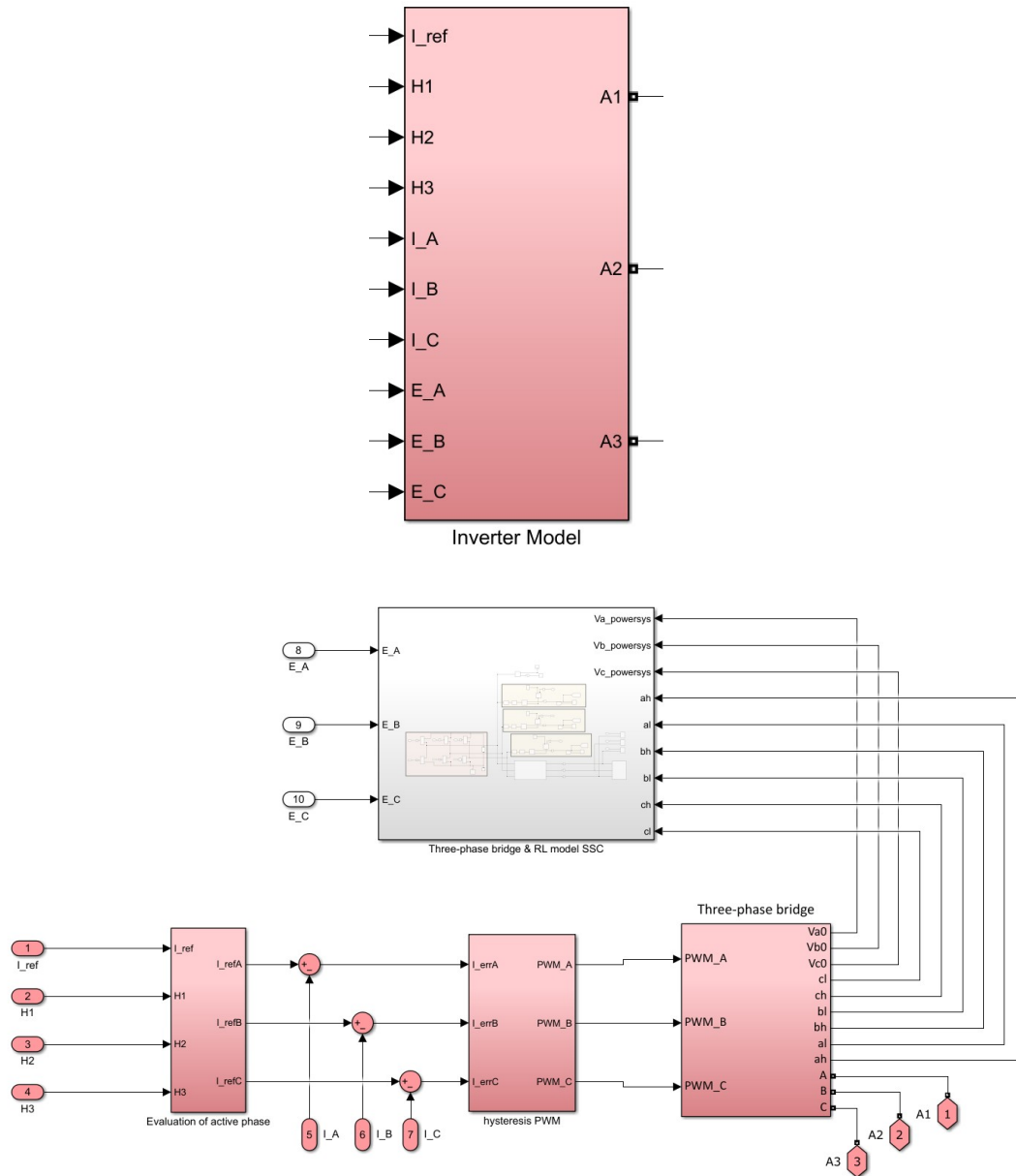


Figure 3.7: Inverter Model subsystem

3.5.1 Evaluation of active phase subsystem

The "Evaluation of active phase" subsystem receives as input the single-phase reference current I_{ref} and the signals H1, H2, H3 that correspond to the action of the Hall effect sensors described above. The comparison between H1, H2, H3 takes place through summing blocks that produce a multiplication factor (1 0 -1) so that the reference current is split over the three phases and the corresponding reference

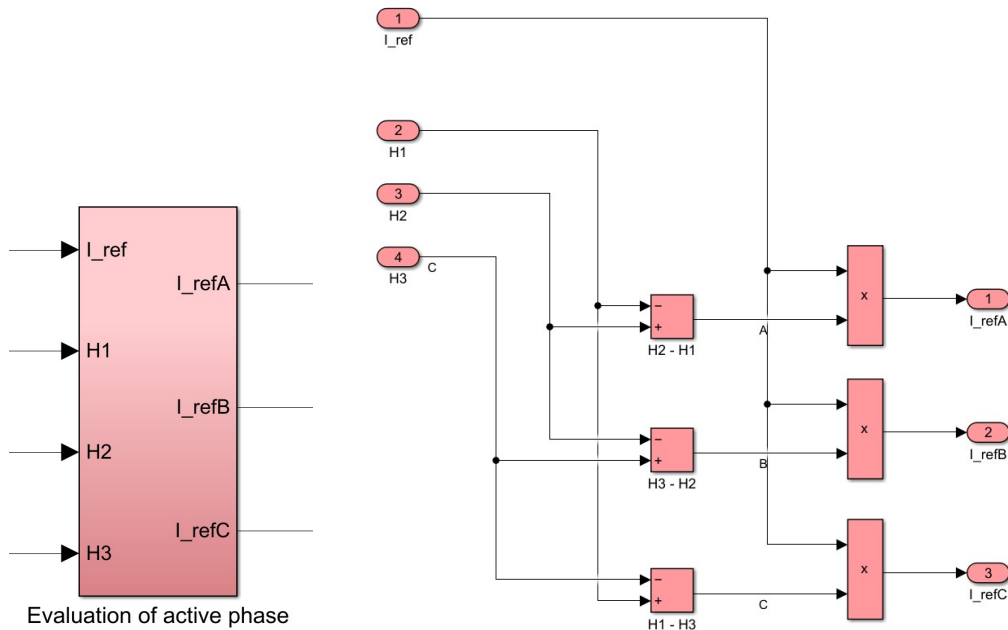


Figure 3.8: Evaluation of active phase subsystem

currents. This operation allows two phases to be supplied at a time (corresponding one to the multiplication factor 1 and the other to -1) while the third phase is set to zero. This subsystem returns the reference currents circulating in each phase of the stator circuit from which the corresponding effective currents circulating in the stator windings are subtracted to obtain a relative error of each current [18]. These signals are sent as input to the "Hysteresis PWM" subsystem, which makes it possible to generate a PWM power supply.

3.5.2 Pulse Width Modulation

PWM switching technology enables effective motor speed control. The motor is supplied with an armature voltage which, instead of being continuous, has a rectangular or impulsive pattern with a supply voltage frequency between a few kHz up to 20 kHz or more, to avoid generation and diffusion of noise in the audible frequency range. The idea is to operate on pulse duration modulation (pulse regulation): the current circulating in the windings, if the modulation frequency is sufficiently high (kHz), due to the circuit's impedance, the current voltage will not be affected by the modulation of the latter, and for the same pulse duration, it will appear approximately constant.

From the figure 3.9, an amplifier senses the difference between a reference voltage V_i and the reaction voltage V_f generated by a tachometer, producing an error voltage V_e at the output. A comparator compares V_e with a sawtooth (or triangular)

voltage V_{es} of constant frequency, generated by an oscillator. The output of comparator V_0 is a rectangular wave of constant frequency and variable duty-cycle with frequency and duty-cycle varying with the level of V_e , which switches to drive the transistor.

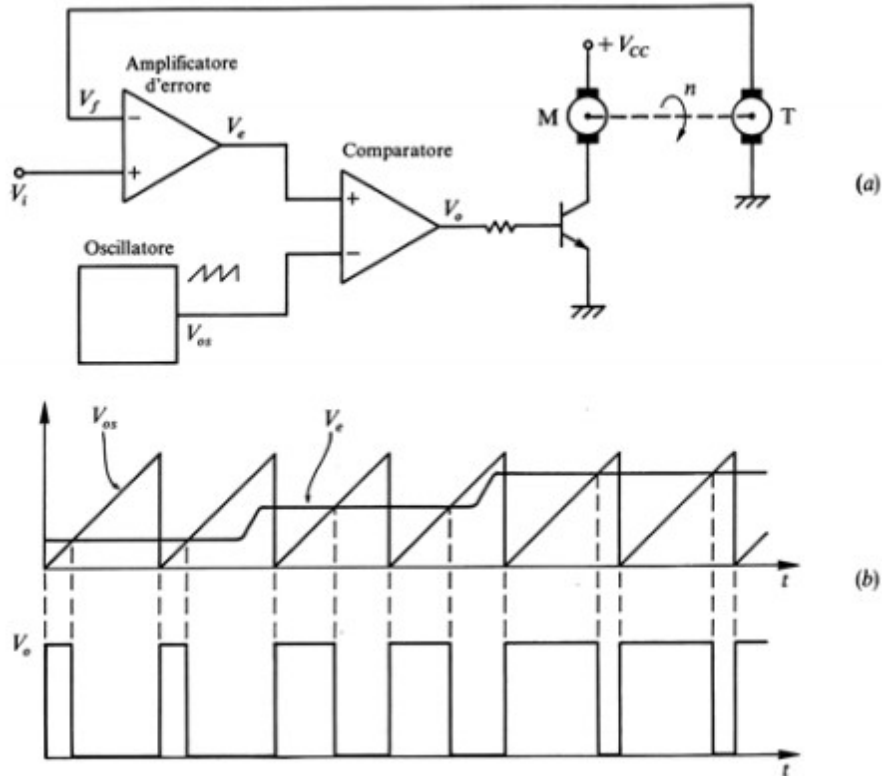


Figure 3.9: Working principle of PWM

Any modulating function can be used for PWM modulation, as long as its frequency is small enough in relation to the frequency of the triangular wave (Nyquist-Shannon sampling theorem) [9].

3.5.3 Hysteresis PWM subsystem

The PWM technique is modelled in a more simplified manner than the real technique, which involves sending the relative error of each current to a PID controller which will command the correct alternation of the power supply of the various phases to obtain a magnetic field of the stator properly directed to that of the rotor generated by the permanent magnets to generate the driving torque. For this thesis work, it was considered unnecessary to model the PWM technique in detail, since the action of the PID controller could be replaced by a “hysteresis” block which compares the input with a maximum and minimum threshold value,

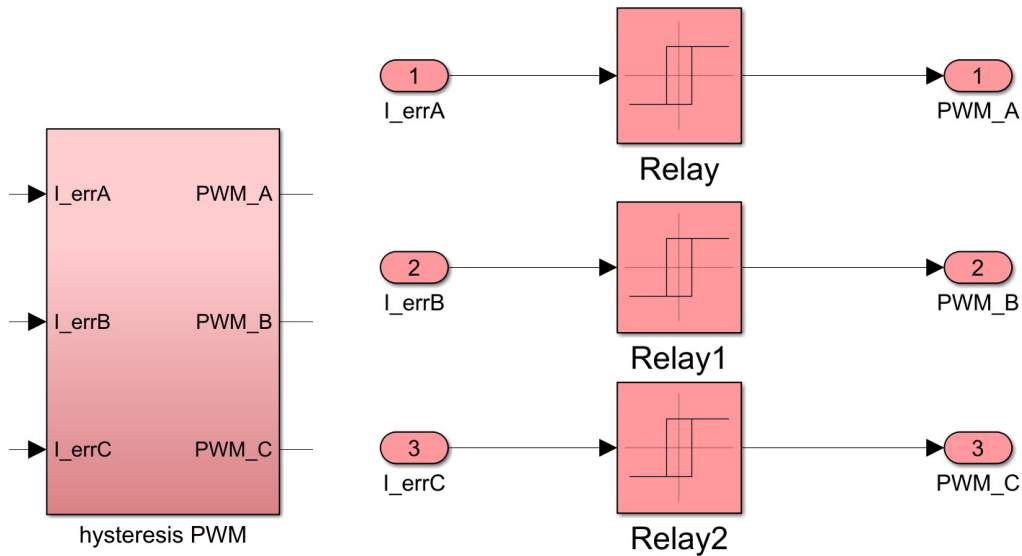


Figure 3.10: Hysteresis PWM subsystem

generating the following output signals:

- 1 if the current exceeds the maximum threshold value
- 0 if the current is below the minimum threshold value
- The input value if the latter is within the band

In this way, the correct supply voltage is controlled, avoiding the return signal branch of the PID controller but at the same time having a signal that respects the characteristics of a PWM modulation. In reality, this type of modulation presents a criticality at the moment the system is not activated as the currents settle at the null value (unless the action of the integral branch of the PID controller is not active enough to damp any non-linearities that persist over time). In the case of using the “hysteresis” block, the currents never settle on the null value since the passing signal corresponds to the one when the system was still active, therefore the currents will assume a value close to zero but not completely null. The PWM technique determines the frequency at which the phases are fed and, according to the Nyquist-Shannon theorem, this must be at least one order of magnitude higher than the inverter’s switching frequency to avoid aliasing problems and loss of information due to inefficient sampling. The Boolean signals PWM_A , PWM_B , PWM_C coming out of the "Hysteresis PWM" block enter the "Three-phase bridge" subsystem [19].

3.5.4 Three-phase bridge subsystem

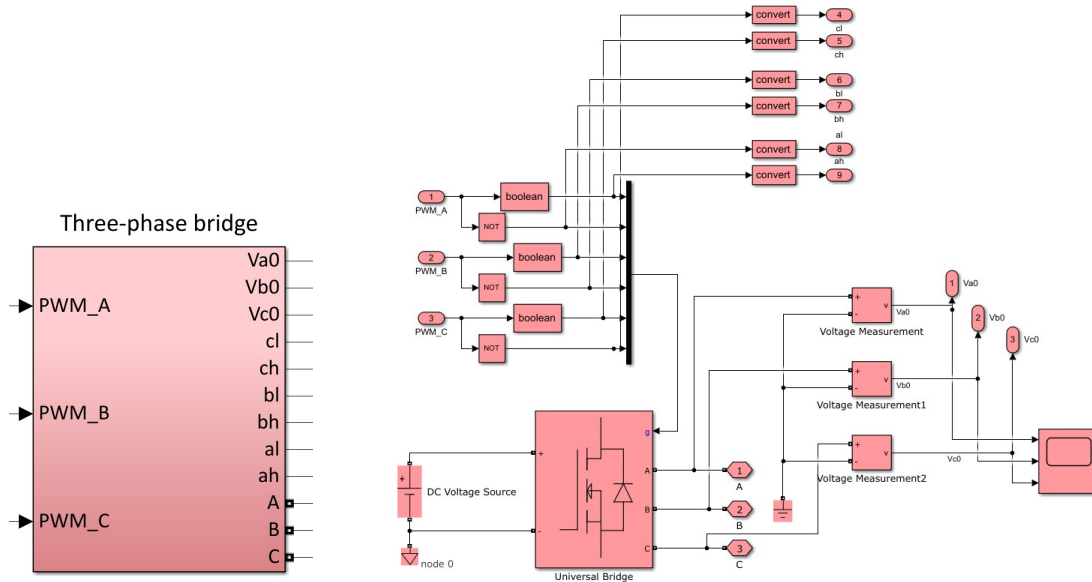


Figure 3.11: Three-phase bridge subsystem

The "Three-phase bridge" subsystem makes it possible to model, through the "universal bridge" block of the Simscape library, a static three-phase bridge converter powered by a DC voltage generator. The three-phase bridge is characterised by the presence of six MOSFET-type power transistors which switch the supply voltage according to the Boolean input signals in the "g" port dependent on the angular position of the rotor detected by the position sensor. In this way, the system solves three equations in voltage and current considering that the voltages of phases A, B, C are the same that supply the electromagnetic circuit while the supply currents of the three phases will have opposite sign in the input of the "electromagnetic model" subsystem respecting the input-output sign convention.

3.6 BLDC electromagnetic model subsystem

The "BLDC electromagnetic model" subsystem shown in the figure 3.12 implements the electromagnetic effects on the stator windings by taking into account the counter-electromotive force opposing the current variation that induced it (according to Faraday's law). This effect is modelled in the "computation of back-EMF coefficients" subsystem.

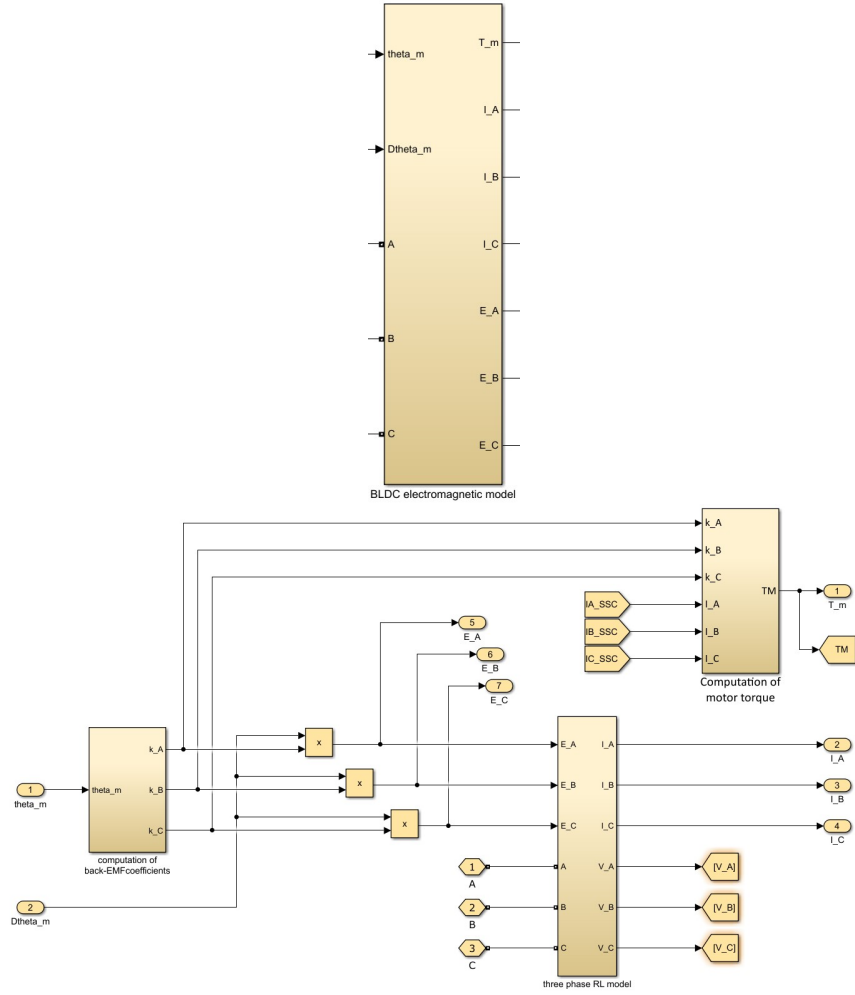


Figure 3.12: BLDC electromagnetic model subsystem

3.6.1 Computation of back-EMF coefficients subsystem

As shown in the figure 3.13, the input of the subsystem is the angular position ϑ_m of the motor which undergoes, in the "computation of ϑ_e " section, the conversion from a mechanical signal into the corresponding electrical signal which is limited between 0 and $2\pi \text{ rad}$.

$$\vartheta_e = N_p \vartheta_m \quad (3.3)$$

$$\vartheta_e = 2\pi \left(\frac{N_p \vartheta_m}{2\pi} - \text{floor} \left(\frac{N_p \vartheta_m}{2\pi} \right) \right) \quad (3.4)$$

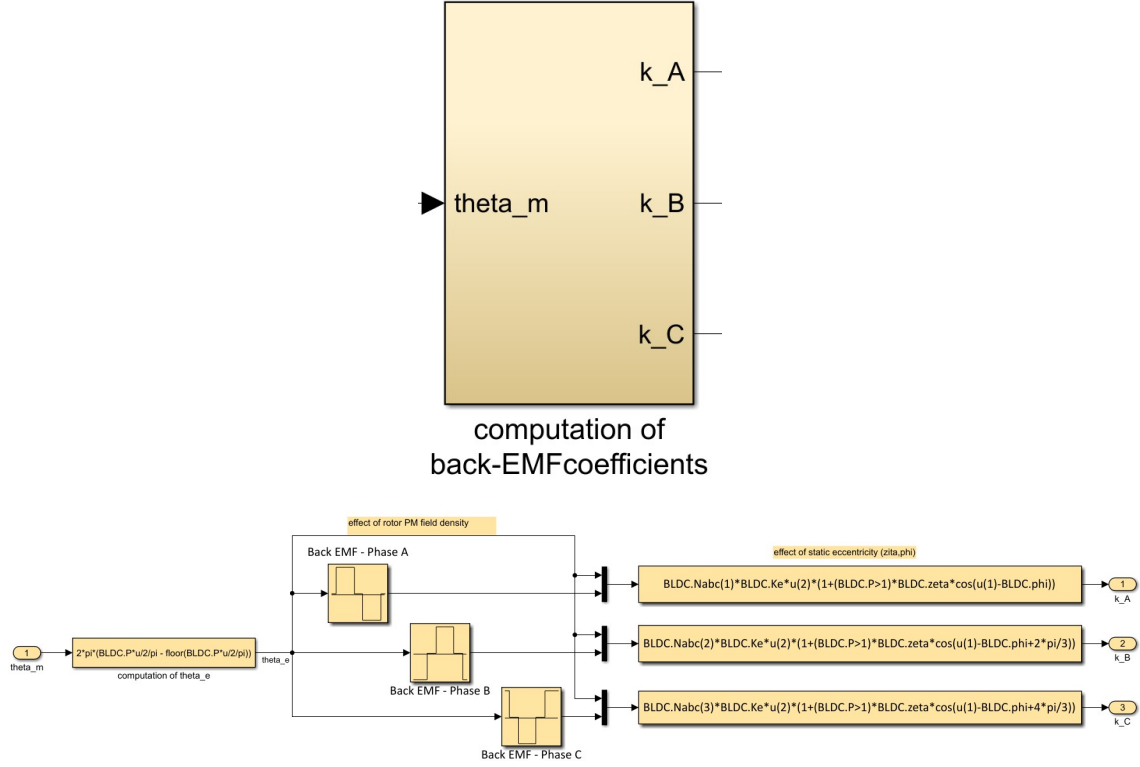


Figure 3.13: Computation of back-EMF coefficients subsystem

Subsequently, in the "effect of rotor PM field density" section, the effects linked to the nominal and constant counter-electromotive force on each individual phase are calculated through the use of "Lookup" blocks which allow ϑ_m to be multiplied by specific form functions that contain Boolean signals so as to assign a sign of the back-EMF on each phase as a function of the currents that are instantaneously switched for the power supply. Next, the effects of two different failures are considered, such as a possible short circuit and the effect of static eccentricity of the rotor, through the section "effect of static eccentricity (ζ, ϕ)", which may be present due to manufacturing defects [18]. If the number of motor pole pairs is greater than one, the effect of eccentricity in the electromagnetic coupling is considered as a function of the angular position of the rotor:

$$K_{f_{cem}}^{(i)} = N_i K_e^{(i)} f(\vartheta_e) \cdot \left(1 + \zeta \cos \left(\vartheta_e - \varphi + \frac{2(i-1)}{3} \pi \right) \right) \quad (3.5)$$

where $K_e^{(i)} f(\vartheta_e)$ is the waveform of the normalised counter-electromotive force for each individual motor phase without faults, evaluated in the lookup table above, ζ is the ratio of rotor eccentricity and nominal air gap, N_i is the fraction of active

coils of the i -th phase and φ is the static eccentricity phase. The outputs of the subsystem k_A, k_B, k_C represent the normalised counter electromotive forces of the three phases which are multiplied by the angular speed of the motor to obtain as a result the counter electromotive force acting on the single phases E_A, E_B, E_C .

3.6.2 Three-phase RL model subsystem

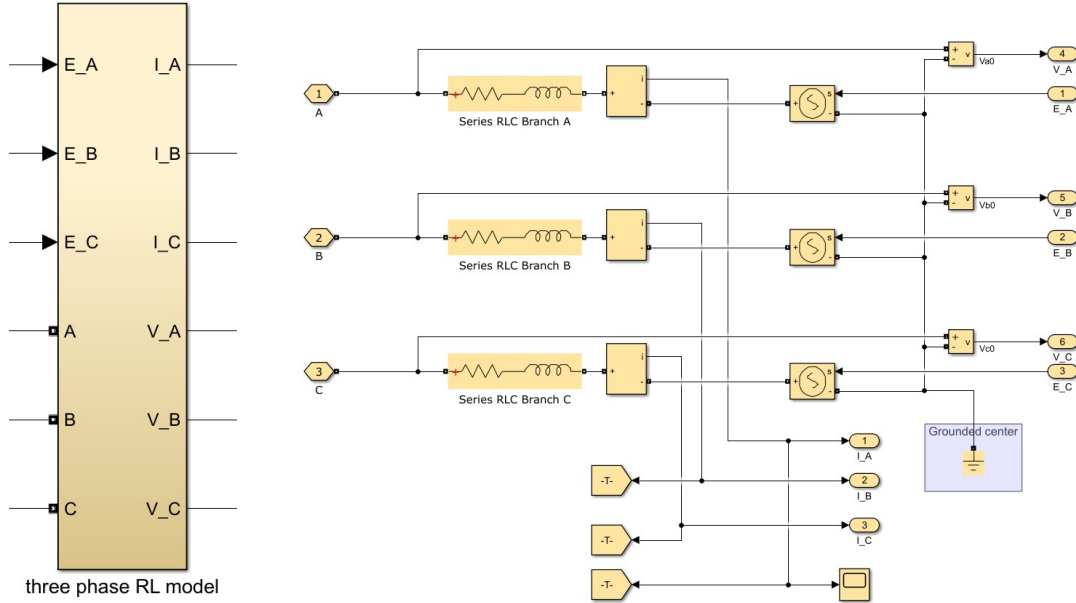


Figure 3.14: Three-phase RL model subsystem

The subsystem is connected via connection ports A, B and C to the phases exiting the "universal bridge" described in "Three-phase bridge subsystem" subsection. In particular, the three stator windings are modelled as an ohmic-inductive system characterised by a resistor and an inductance placed in series and connected in a star configuration. The formula 3.6 describing the voltage trend is:

$$V_{eff}^{(i)} = Ri^{(i)} + L \frac{di^{(i)}}{dt} \tag{3.6}$$

The value of resistance and inductance are chosen so that a possible short circuit can be modelled by selecting the partial fraction of windings which are actually active according to the relationships 3.7 and 3.8:

$$R_i = RN_i \tag{3.7}$$

$$L_i = LN_i^2 \quad (3.8)$$

A voltage generator is placed in series to the three "RL blocks", which takes as input the signal of the respective counter-electromotive force of each phase calculated at the output of the "computation of back-EMF coefficients" subsystem and converts it into voltage. In addition, the voltage generator is connected to the "RL block" of each phase and to the branch connected to the "ground" representing the star centre of the three-phase circuit, respectively. Thus, according to the voltage sign convention, on each phase the corresponding counter-electromotive force is subtracted from the active supply voltage commanded by the "universal bridge" to take into account these effects on the generation of the active current on each winding. Therefore, the effective voltage will be:

$$V_{eff}^{(i)} = V_{alim}^{(i)} - E^{(i)} \quad (3.9)$$

To measure the active currents I_A, I_B, I_C an ammeter is placed in series on each phase "RL circuit", while a voltmeter connected in parallel between the phase and the star centre is used to measure the active voltages.

3.6.3 Computation of motor-torque subsystem

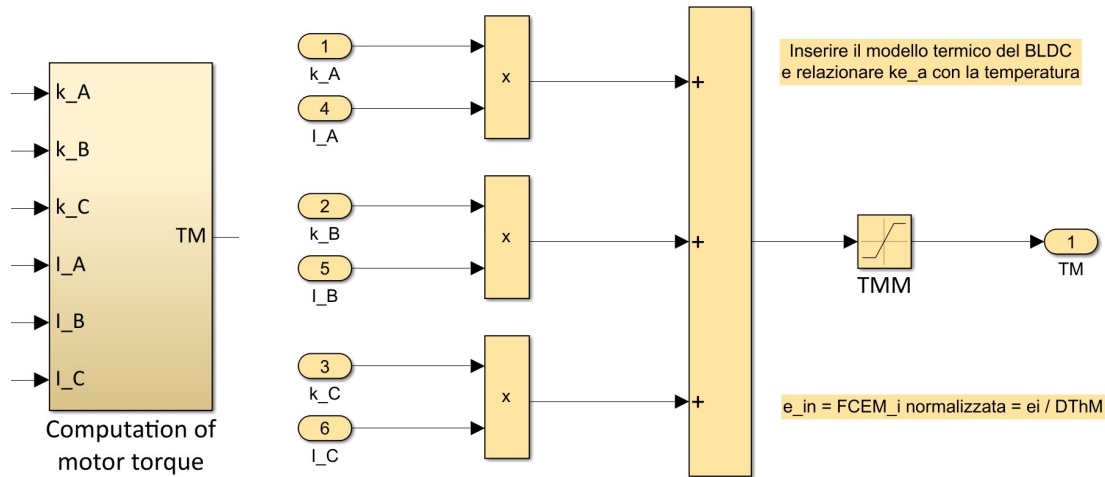


Figure 3.15: Computation of motor-torque subsystem

The subsystem calculates the torque produced by each motor phase by multiplying the counter-electromotive force constant and the respective current circulating in

each phase:

$$C_i = k_i I_i \tag{3.10}$$

Subsequently, the three contributions are added together to obtain the resulting torque produced by the motor. The "saturation" block is used to limit the value of the resulting torque to take account of the motor's performance limits.

3.7 Motor transmission dynamic model subsystem

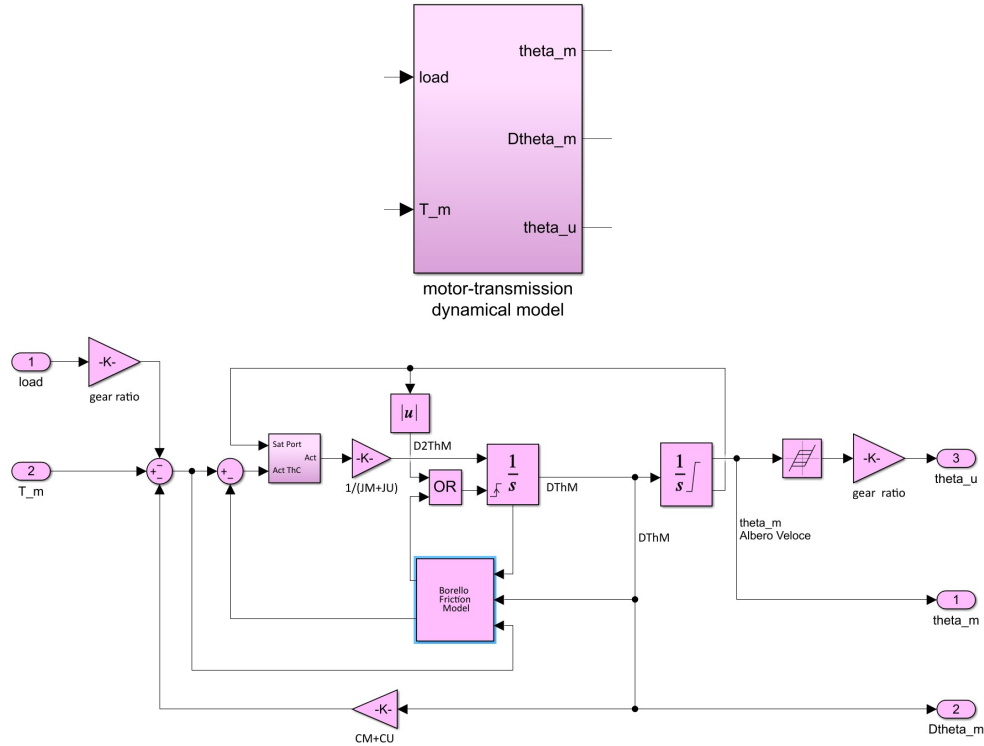


Figure 3.16: Motor transmission dynamic model subsystem

The subsystem is used to calculate the angular position of the motor and of user and the angular speed of the motor. It has as input the torque generated by the motor calculated previously and the external load set by the user at the start of the simulation. The latter is multiplied by a gain equal to the transmission coefficient τ to take account of the transition from the low-speed shaft (in relation to which the external load is set) to the high-speed shaft (in relation to which ϑ_m and $\dot{\vartheta}_m$ are calculated). Then, the contribution of the external load is subtracted from

the torque generated by the motor and the contribution of the torque generated by the viscous forces equal to the product of the angular speed of the motor $\dot{\vartheta}_m$ and a gain equal to the viscosity coefficient of the motor-user system. The net torque is further reduced by a contribution equal to the friction force generated by the “Borello friction model” block implementing the Borello friction model. A representation of this model is shown in the figure 3.17.

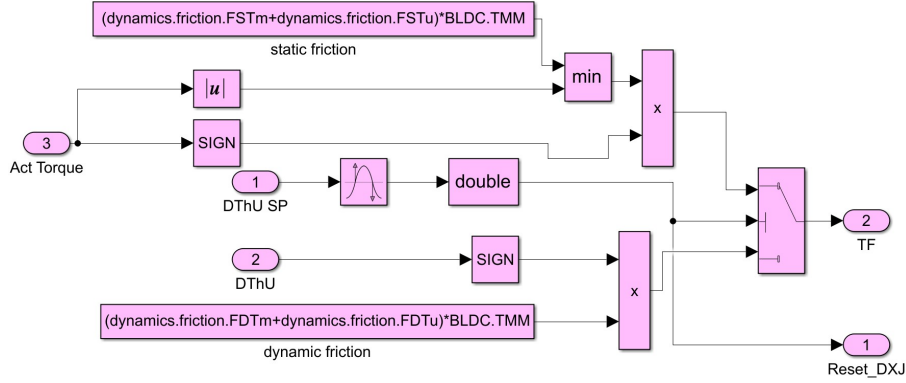


Figure 3.17: Borello friction model

The peculiarities of this friction model make it indispensable to model the effects of static and dynamic friction on a system and to have a description very similar to that of real phenomena [20]. In particular, the model makes it possible to:

- Discriminate the condition of static or dynamic friction
- Correlate the sign of the friction force to the sign of the system’s velocity
- Evaluate if the body, initially stationary, starts to move
- Evaluate if the body, initially in movement, stops
- Evaluate possible adherence conditions
- Consider possible mechanical end stops of the system

From a mathematical point of view, the model can be expressed through the following system of equations:

$$F = \begin{cases} F_{act} & \text{if } v = 0 \wedge |F_{act}| \leq FSJ \\ \text{sign}(F_{act}) \cdot FSJ & \text{if } v = 0 \wedge |F_{act}| \geq FSJ \\ \text{sign}(v) \cdot FDJ & \text{if } v \neq 0 \end{cases}$$

In the static friction situation, the model compares the active force, in absolute value, with the static friction force by means of a function that returns the minimum between the two values. Multiplying the latter by the sign of the active

force, the value of the friction force in static conditions is found. In the dynamic friction situation, the sign of the effective velocity generated by the first integrator is multiplied with the value of the dynamic friction force to obtain the dynamic friction force with sign. To evaluate the static or dynamic condition, the "Zero-Crossing-Detection" block is used, which takes as input the velocity coming out of the integrator. This block is useful because:

- If the output is equal to 1, it means that the condition of zero crossing has occurred and therefore there is a condition of static friction with the activation of only the static branch, while if the output of the block is zero it means that there is a situation of dynamic friction and only the respective branch is active.
- It evaluates the value of the velocity at each time step and whenever a zero crossing occurs it means that the velocity has assumed the value of zero. Since it is highly improbable that it is possible to evaluate exactly the instant in which the velocity assumes the null value (this would risk numerical instability), when there is a zero crossing, the model arbitrarily sets the velocity equal to zero. If, at the next time step, the equilibrium of forces is such that the system starts moving again, then the velocity is automatically recalculated, otherwise it remains at zero.

The difference between the active force and the friction force calculated with Borello's model, is supplied as input to the subsystem that models the reaction of the support and contains, in addition, a "saturation port" block for the angular velocity signal coming out of the integrator. The output of the "saturation port" can take on three different values:

- 1 if the upper speed limit is exceeded
- 0 if the speed value is within the limits
- -1 if the lower limit is exceeded

Within the subsystem, the "switch" regulates the passage of the signal and imposes a zero effective torque if the torque is greater than zero with the motor at the upper position limit or if there is less than zero torque with the motor at the lower position limit. This logic makes it possible to simulate the reaction of the support. In all other cases, however, what passes through is the calculated torque.

In this way, the torque generated at the output of the block is divided by the equivalent inertia of the motor, allowing the calculation of the angular acceleration, which then undergoes two successive integrations to calculate the speed and angular position respectively. The first integrator that returns the angular velocity as output is equipped with a "rising reset" which is activated if one of the following two cases is verified [20]:

- The absolute value of the signal coming from the "saturation port" of the

speed integrator is between 0 and 1; this means that the stop condition has been reached.

- The value given by the zero-crossing-detection block is 1, i.e. a zero crossing of the speed has occurred.

At this point, the acceleration integrator produces the angular velocity signal, which in turn is integrated by another integrator to calculate the angular position on the fast shaft, limited at the top and bottom by a "saturation" block. Next, the "backlash" block models the mechanical phenomena that could affect the mechanical gearbox while this gain returns the signal to the slow shaft to calculate the user's angular position.

3.8 Signal acquisition subsystem

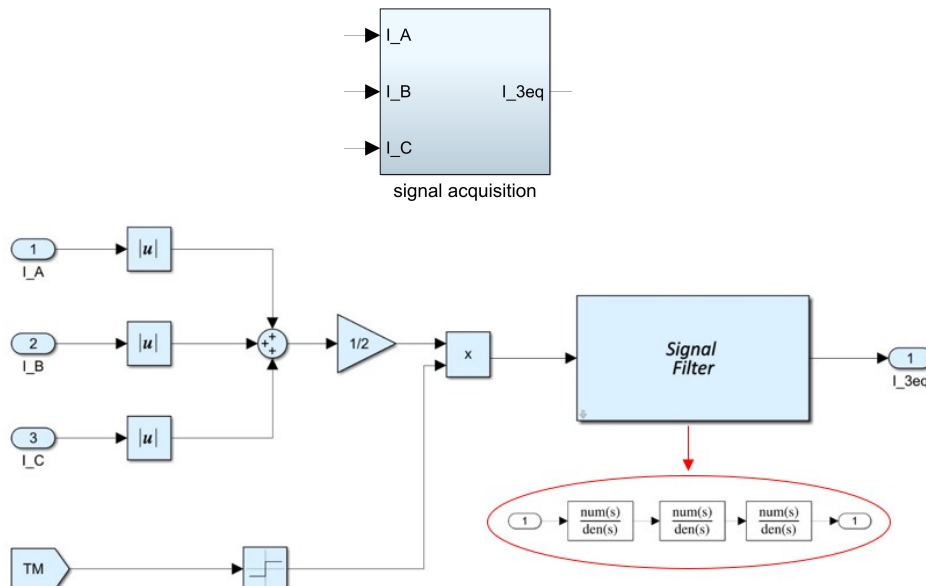


Figure 3.18: Signal acquisition subsystem

The subsystem makes it possible to calculate the current of a single-phase circuit equivalent to the three-phase system that characterises the real motor. As the currents are switched by the control logic, it will result that at each time step one current will be zero on the OFF phase while the other two, equal in magnitude but opposite in sign, will circulate in the other two ON phases. Therefore, the absolute value produces a value equal to twice the corresponding equivalent single-phase current. Therefore, the sum of the three currents obtained must be multiplied by a gain of $1/2$. At this point, this value is again multiplied by the sign of the motor torque obtained previously to obtain a current with a sign and which carries

information on the direction of the current. This current is passed through three first-order filters to eliminate the errors associated with the noise in the system and obtain I_{3eq} . The three filters, however, add a delay to the signal, so it will be necessary to add the three filters to a possible equivalent monophasic model to allow an appropriate and precise comparison between the two current signals, which at this point will be phased.

3.9 Simscape modelling

The use of Simscape was necessary to enable future applications to model various problems related to non-linearities and to perform multi-domain analyses, i.e. considering the interaction of different physical effects on the system. In fact, unlike the blocks of the "Power Systems" library in Simulink, with Simscape it is possible to create physical models that automatically implement precise linear and differential algebraic equations to solve the system and obtain the characteristic quantities useful for post-processing analysis. In this specific case, a digital 'twin' model was generated in Simscape which reproduced the same operation of the three-phase power transistor bridge and the electromagnetic phenomena characteristic of the stator windings.

3.10 Three-phase bridge and RL model Simscape subsystem

Simscape model simulation runs in parallel with Simulink model simulation. It is possible to change the simulation parameters in Simscape through the "Solver configuration" block. In particular, the block allows you to set several parameters including the integration method for the simulation by choosing from the settings in "Use local solver" and the time integration step from the "Sample time" interface. In the present case, the same parameters of the Simscape model have been set, i.e. the fixed step Euler integration method (in Simulink *ode1 (Euler)*) and the time integration step equal to 10^{-6} s.

Representative three-phase bridge and three-phase stator circuit diagrams are shown in the figure 3.19 .

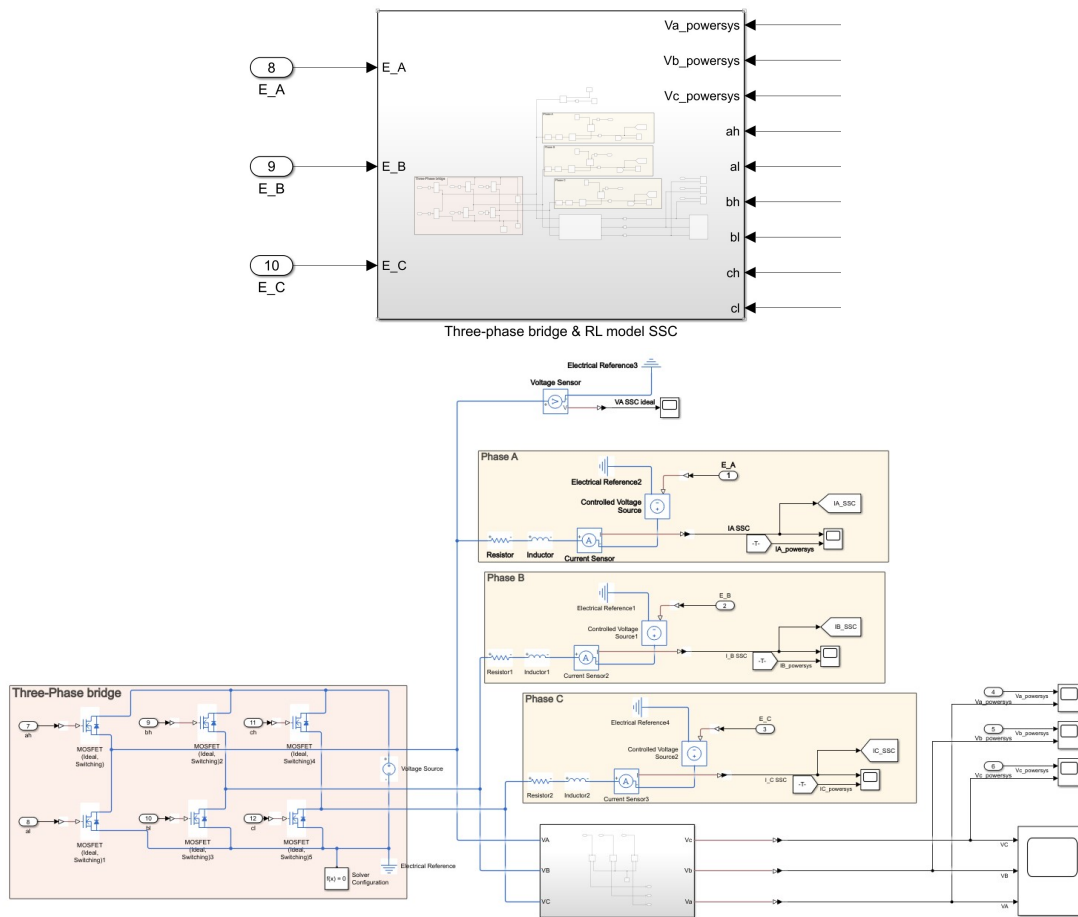


Figure 3.19: Three-phase bridge and RL model Simscape subsystem

3.10.1 Three-phase bridge

The figure 3.20 shows the construction of the model implementing the operation of a static three-phase bridge power transistor converter of the "Mosfet" type .

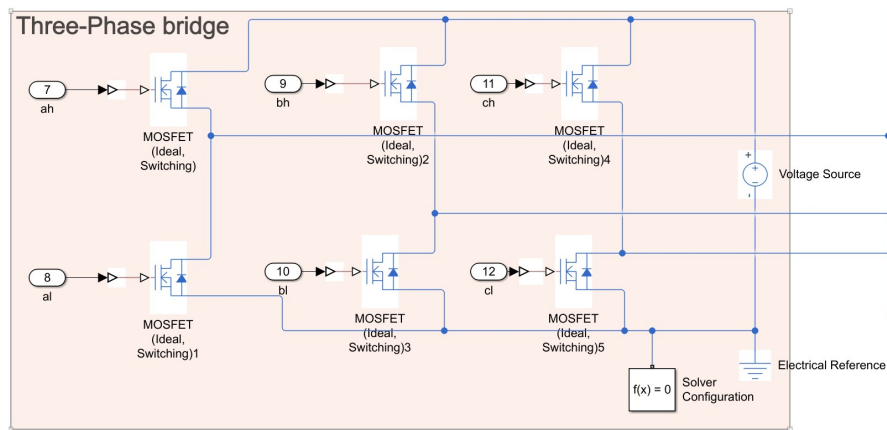


Figure 3.20: Three-phase bridge

A preliminary analysis allowed us to select the "Mosfet (Ideal Switching)" blocks from the "Electrical" library in Simscape. These blocks represent a simplification of the actual devices, since their characterisation required very precise technical data known only to the manufacturing companies. The "Mosfet (Ideal Switching)" blocks can be equipped with protection diodes which prevent dangerous over-voltages at the ends of the transistors during ON-OFF switching of the phases due to the inductive behaviour of the electric motor. The main characteristics that protection diodes must have are:

- They must be able to switch from a non-current flowing condition to a conducting condition and vice versa. Therefore, they must have characteristic operating times in the order of nanoseconds
- They must be able to dissipate high currents since in the ON-OFF transition all the current supplying the motor passes through the diode (in the order of amperes).

The parameters set for the six "Mosfets (Ideal Switching)" and for the protection diodes are shown in the table 3.1.

Being a three-phase stator circuit, it was necessary to construct three different branches with two power transistors each of which receives as input the Boolean signals for phase switching. These signals are "ah, al, bh, bl, ch, cl" which come from the "Three-phase bridge" subsystem implemented in "Power Systems" and correspond exactly to the signals for the switching implemented in the HF reference

Main	
Drain-source on resistance, $R_{DS(on)}$	$10^{-2} \Omega$
Off-state conductance	$10^{-6} \Omega^{-1}$
Threshold voltage, V_{th}	$0.5 V$
Integral diode	
Forward voltage	$0.8 V$
On resistance	$10^{-3} \Omega$
Off conductance	$10^{-5} \Omega^{-1}$

Table 3.1: Mosfet Ideal Switching Data

model produced in Simulink. These signals are then transformed from Simulink signals to physical signals using a converter called the "Simulink-PS Converter". In this way and according to the data set for the "Mosfet (Ideal Switching)", it was possible to implement phase switching according to the angular position of the motor and the control logic applied. The three-phase bridge is supplied with a voltage of 380 V DC.

The electrical model in Simscape requires the presence of two further blocks: the "Electrical Reference" block, which represents the "ground" reference required to solve the voltage and current equations, and the "Solver Configuration" block, which allows the model to be implemented by setting various parameters, such as the local time integration step or the degree of tolerance.

3.10.2 Three-phase stator circuit

In this case, the three stator phases have a star arrangement, i.e. they have their own common point called the star centre. Initially, for the resolution of the model, it was not planned to connect the star centre to a ground reference because the use of the electric motor in flight would not have allowed such a connection. Therefore, the model to be modelled and analysed should have been a floating neutral. This problem was also addressed using Simscape's "Foundation Library" but, while in "Power Systems" the floating-neutral model was solvable because Simulink works numerically on the final solution, Simscape differently implements automatically equations to find the solution, so eliminating the ground reference means depriving the system of an equation, making the system unsolvable. In fact, every physical model built through Simscape needs its own "reference" to implement the equations for resolution. Therefore, the initial intention to model a three-phase system with a floating neutral has been replaced by placing the neutral connected to the "ground" reference. In reality, this does not particularly affect the results on which this thesis work wishes to focus since it is still necessary to implement a simulation as close to reality as possible even with the use of the electric motor connected to ground. Each phase of the system is characterised by a resistor and an inductance placed in series, making the circuit ohmic-inductive. In series with the circuit RL of each

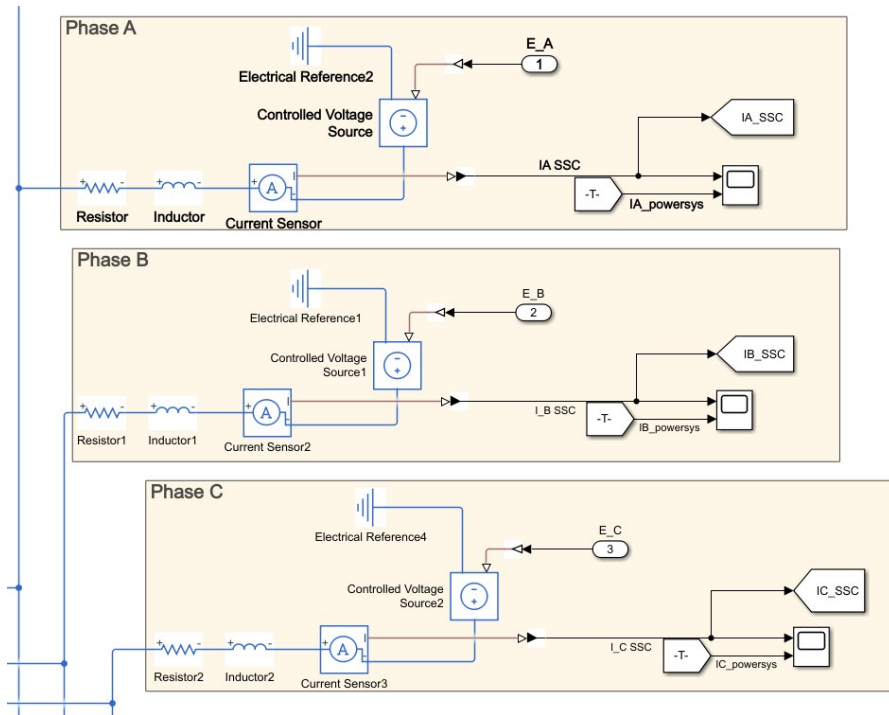


Figure 3.21: Electrical windings

phase, a voltage source referring to the "ground" is placed which receives the signal of the counter-electromotive force so that the voltage generated is subtracted from the supply voltage acting on each phase driven by the three-phase bridge. In this way, the effect of the counter-electromotive force is taken into account to calculate the active currents acting on each phase of the stator. An ammeter is connected in series to the RL circuit to measure the active current on each phase while the voltages are calculated using the "voltage sensing SSC" subsystem shown in the figure 3.22.

The supply voltages on each phase are calculated respectively by means of a voltmeter connected in parallel to the RL circuit and with respect to the "ground". The physical signals produced in Simscape are converted into Simulink signals by the "PS-Simulink Converter" blocks so that trends can be graphed and compared with those obtained in Simulink through the "Scope" blocks.

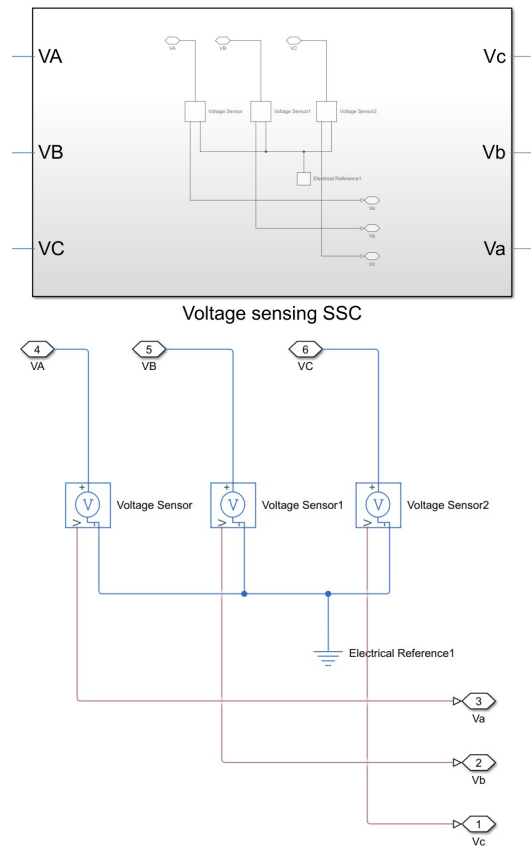


Figure 3.22: Voltage sensing SSC

3.11 Brushless DC Simscape model validation

Several simulations have been conducted in parallel between the numerical HF model produced in Simulink and the physical model produced in Simscape to validate the effectiveness of the latter in faithfully reproducing the same values and trends of the characteristic quantities of the system. In particular, the interest falls only on the voltages and currents acting in the stator circuit since the Simscape model under examination has been produced to simulate the operation of the three-phase bridge and the electromagnetic effects on the windings.

In the following analyses, the graphs of the mechanical quantities of the system, voltages and currents are shown. Only for the case of the "step command" the trends of all three voltages and currents are shown; for the other commands only the trend of the voltage and current on phase A is shown for reasons of synthesis. The graphs of all the characteristic quantities are shown in Appendix A.

3.11.1 Step command

The simulation parameters are reported in the table 3.2.

Initial amplitude	Final amplitude	Instant of application	External load	Simulation time
0 rad	30°	0 sec	0 Nm	0.5 sec

Table 3.2: Data step command

The figures 3.23, 3.24 and 3.25 show respectively the trend of angular position of the motor, angular speed of the motor and angular position of the user.

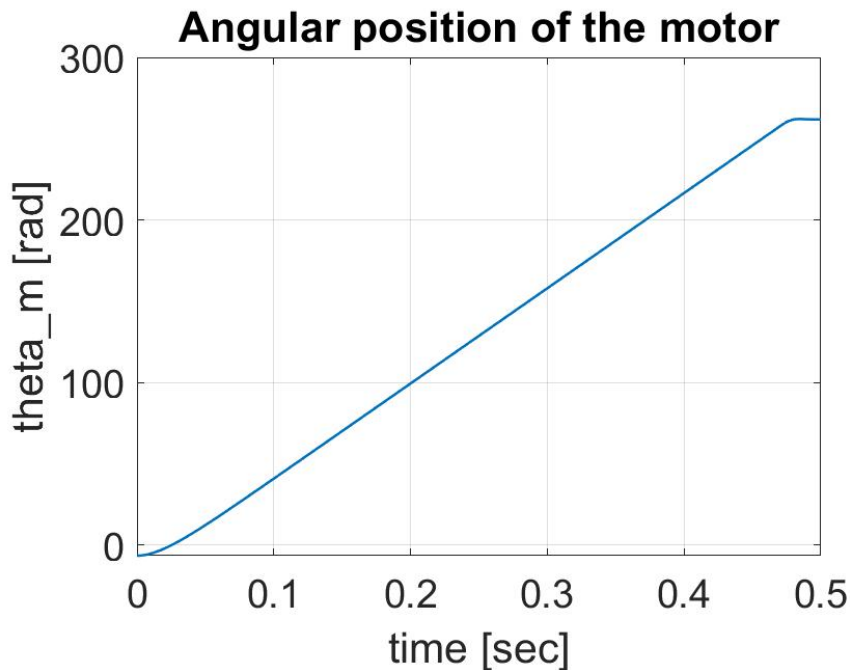


Figure 3.23: Angular position of the motor

The figures 3.26, 3.28, 3.30 show respectively the trend of phase A, B and C current throughout the simulation. The figures 3.27, 3.29, 3.31 show respectively the trend of phase A, B and C current at steady state.

From the figure 3.27, 3.29 and 3.31 which represents the trend of the two currents (from Simulink and from Simscape models) at steady state, it is possible to appreciate more clearly the overlapping of the two lines. The curves have the typical phase current pattern of a brushless DC motor and both suffer from the effects of the inductance present in the stator windings since the currents do not have an instantaneous dynamic (as happens in the purely ohmic model) but grow

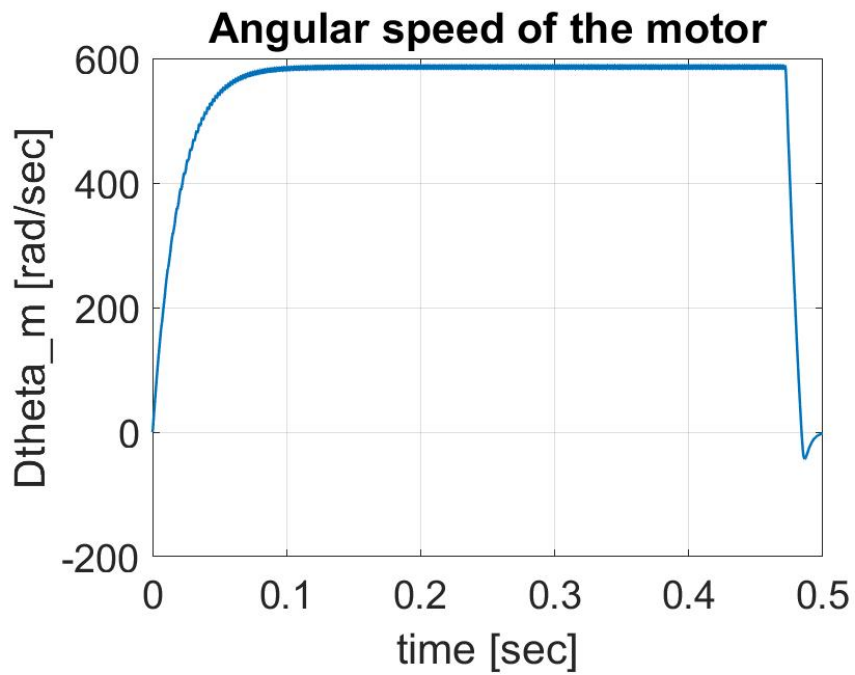


Figure 3.24: Angular speed of the motor

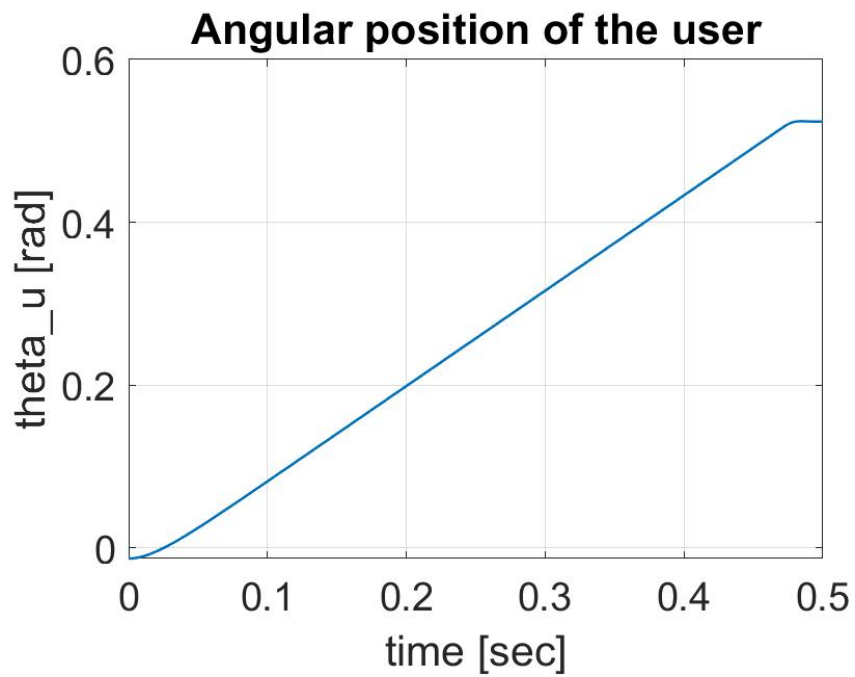


Figure 3.25: Angular position of the user

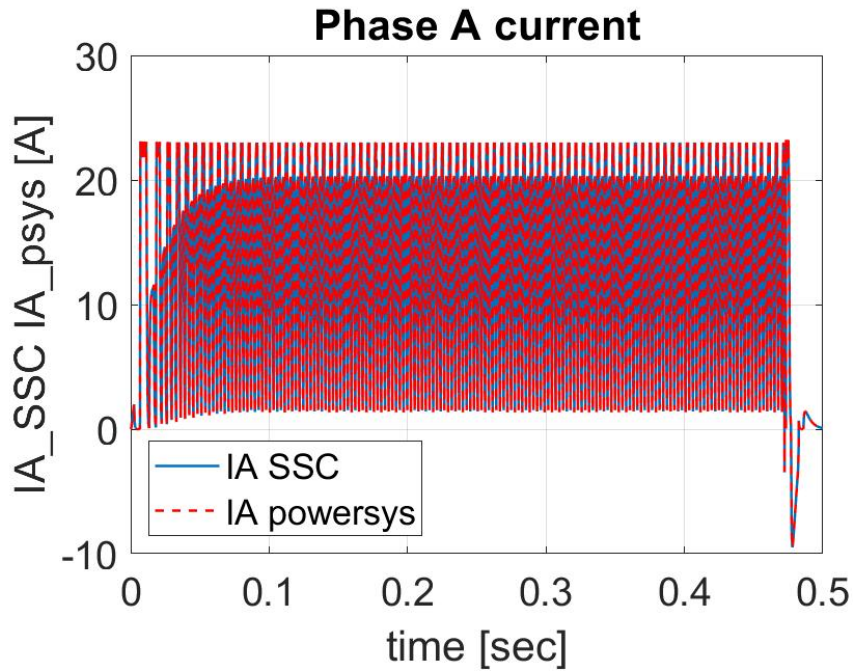


Figure 3.26: I_A

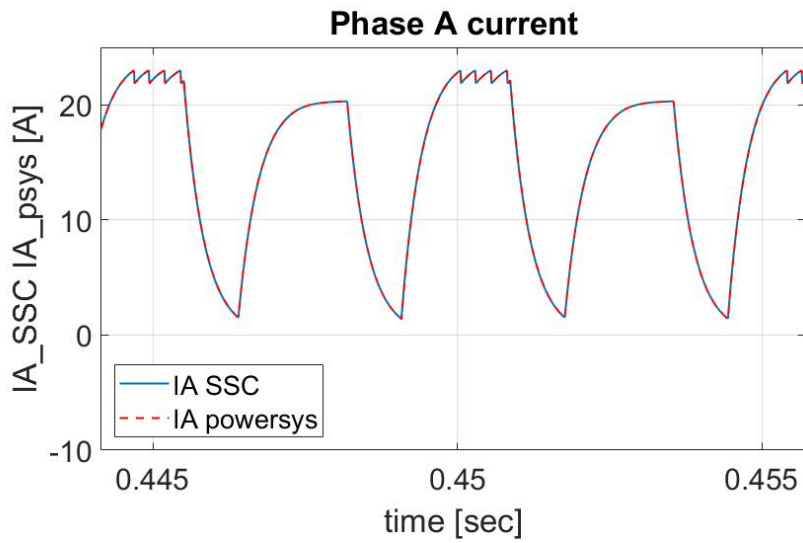


Figure 3.27: I_A at steady state

gradually over time with an exponential trend typical of a first-order dynamic. In fact, the dynamics is characterised by a time constant $\tau = L/R$ (ratio between inductance and resistance) which is generally very small. Neglecting this effect would mean overestimating the degree of stability of the system since the time

constant τ could be of the same order of magnitude as the characteristic time of the dynamics of the whole system and must be taken into account in a realistic modelling to avoid the occurrence of limit cycles.

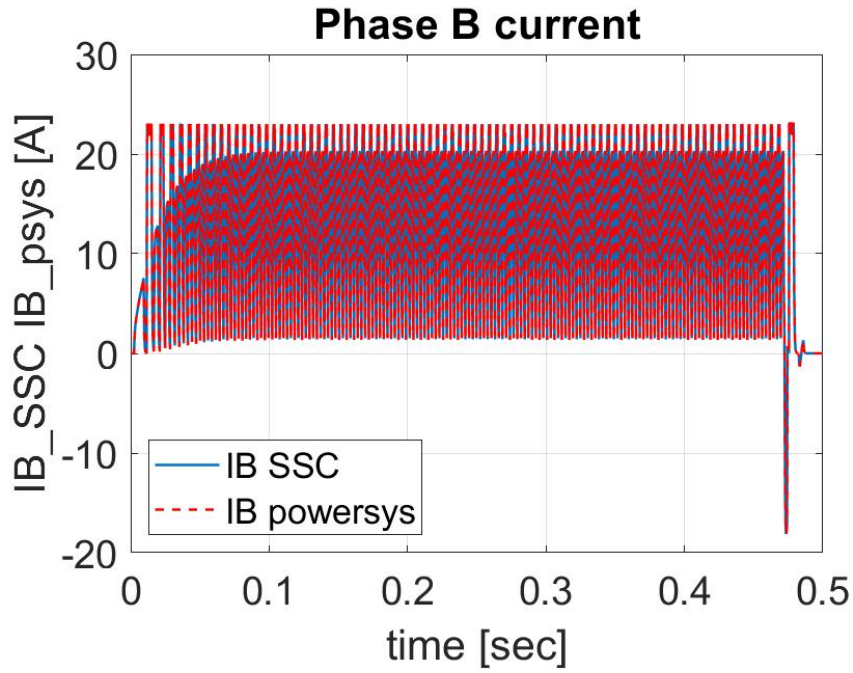


Figure 3.28: I_B

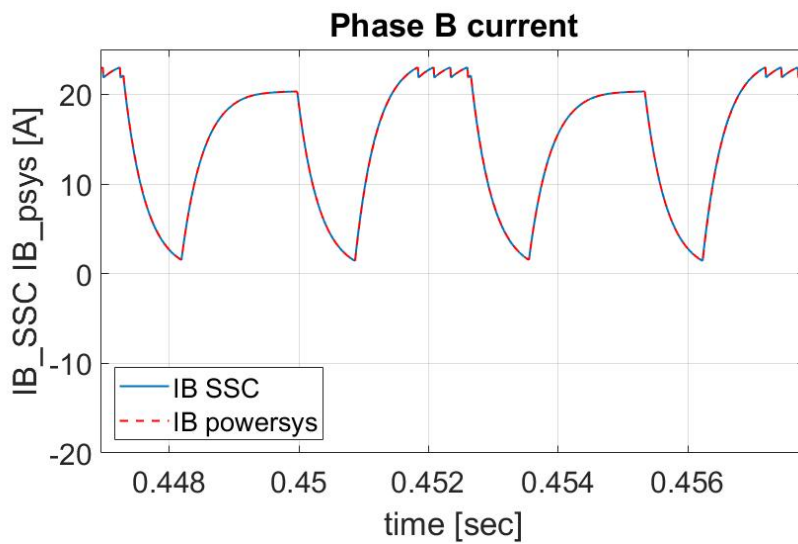
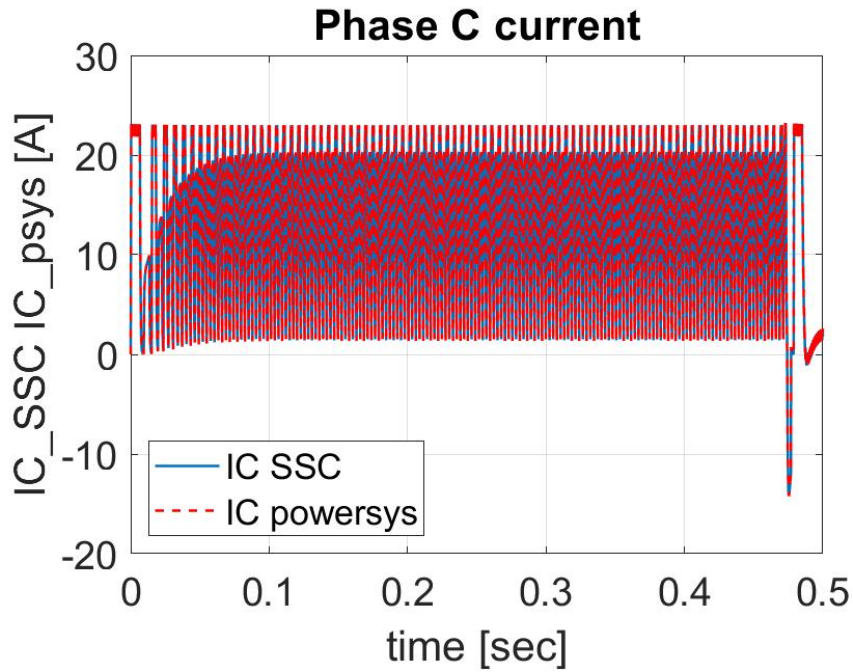
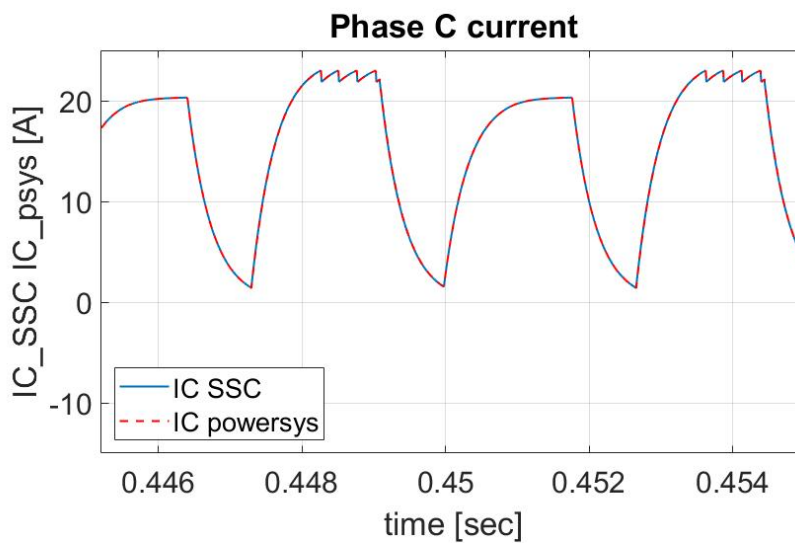


Figure 3.29: I_B at steady state

Figure 3.30: I_C Figure 3.31: I_C at steady state

The figures 3.32, 3.34, 3.36 show respectively the trend of phase A, B and C tension throughout the simulation. The figures 3.33, 3.35, 3.37 show respectively the trend of phase A, B and C tension at steady state and the overlapping of the two curves from Simulink and Simscape model can be appreciated more clearly. In addition,

it can be seen that the PWM power supply logic generates phase voltages that are impulsive and referenced to ground, since the star centre of the three-phase stator circuit is connected to ground reference [9].

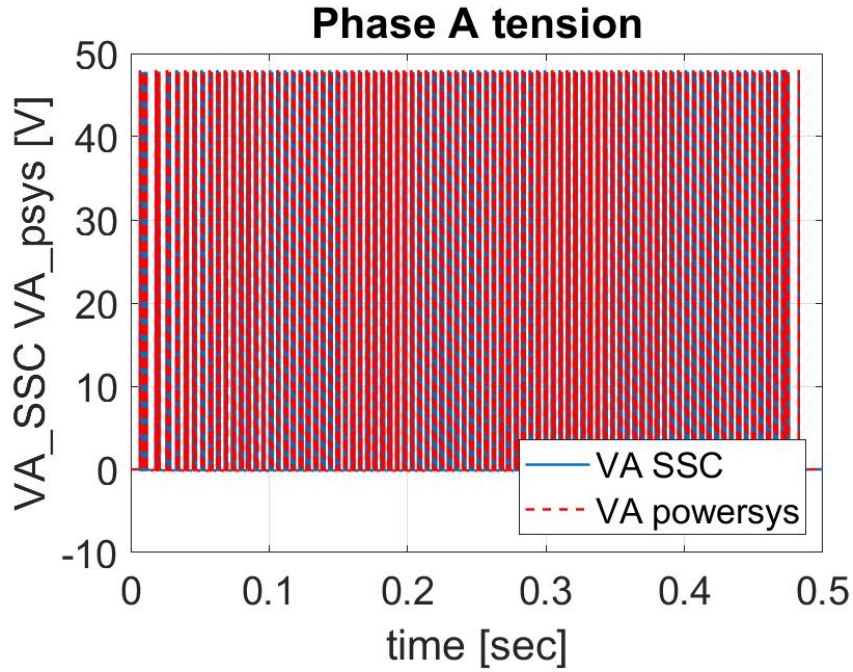


Figure 3.32: V_A

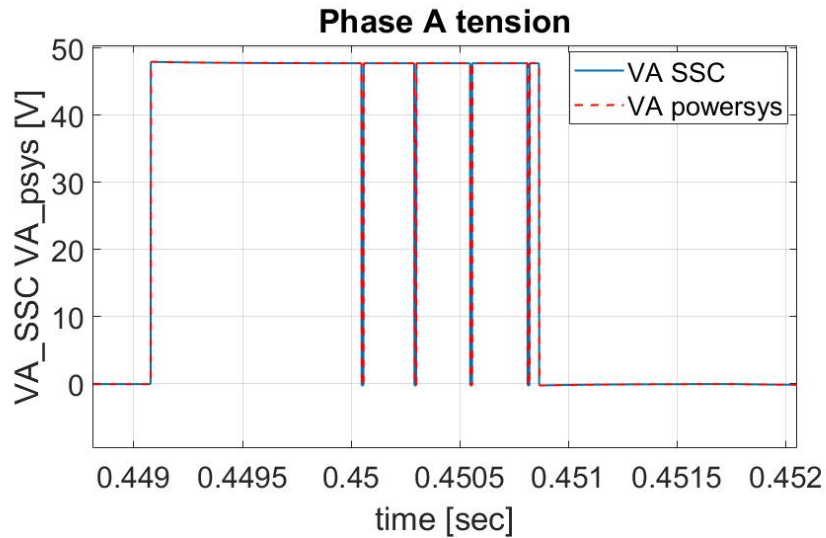


Figure 3.33: V_A at steady state

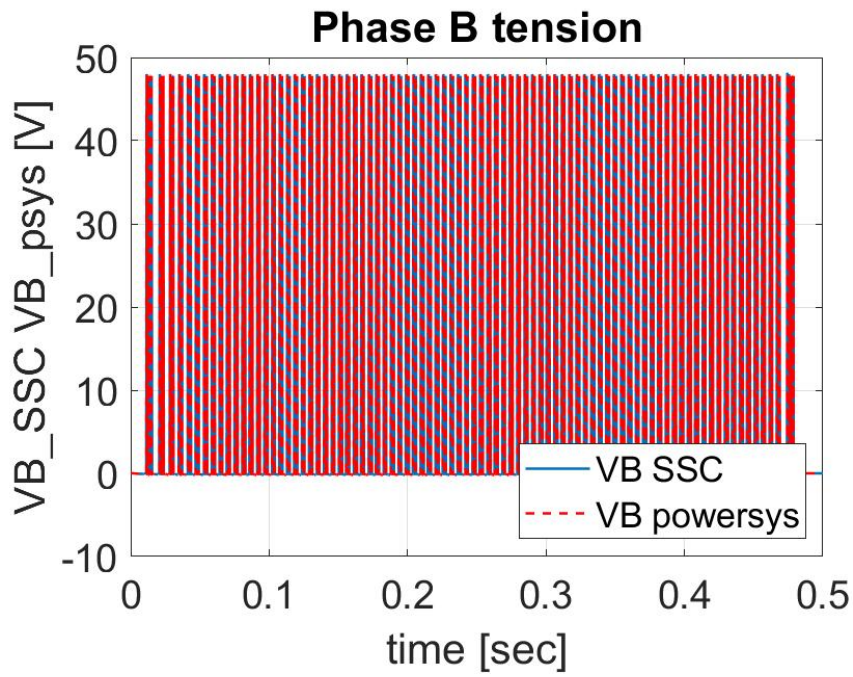


Figure 3.34: V_B

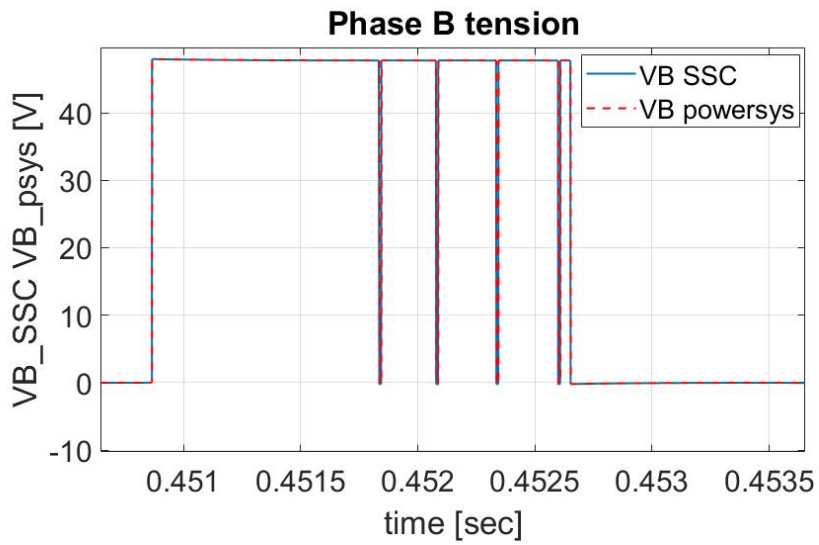


Figure 3.35: V_B at steady state

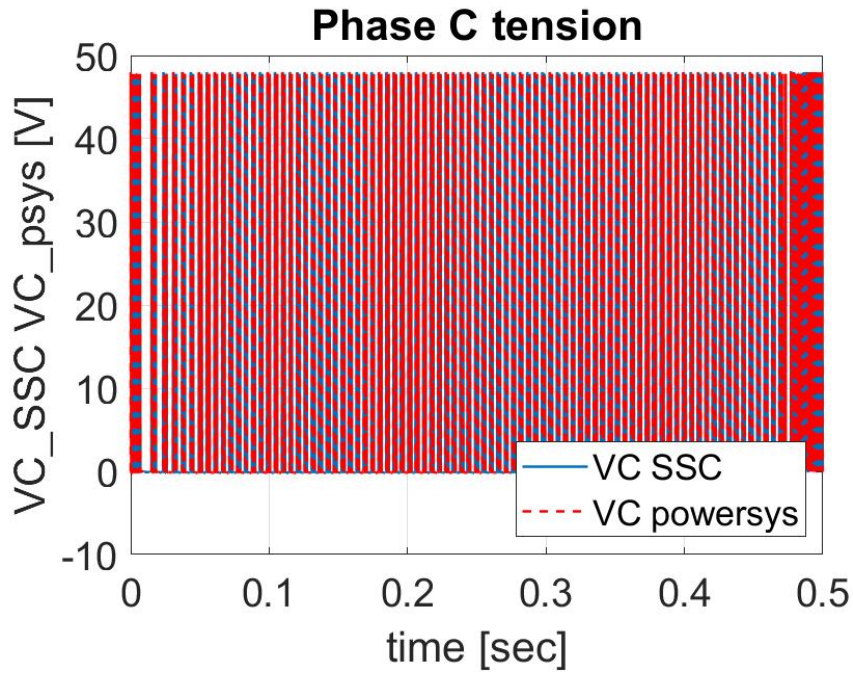


Figure 3.36: V_C

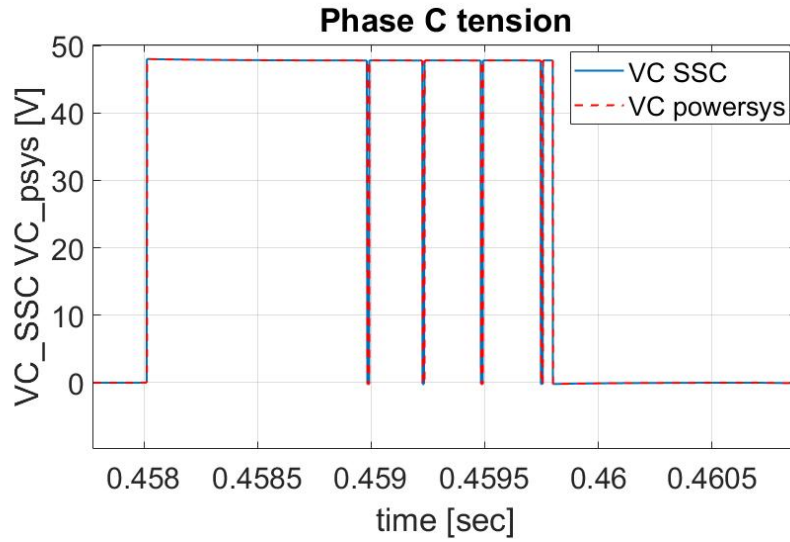


Figure 3.37: V_C at steady state

3.11.2 Ramp command

The simulation parameters are reported in the table 3.3.

Initial output	Slope	Instant of application	External load	Simulation time
0 rad	0.3 rad/sec	0 sec	0 Nm	0.5 sec

Table 3.3: Data ramp command

The figures 3.38, 3.39 and 3.40 show respectively the trend of angular position and angular speed of the motor and angular position of the user.

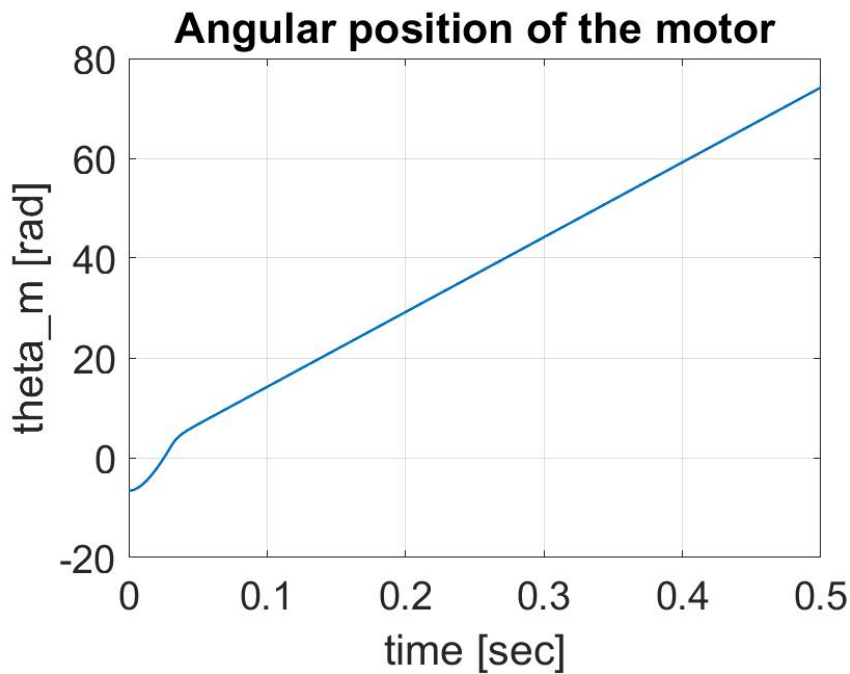


Figure 3.38: Angular position of the motor

The figures 3.41 and 3.42 show respectively the phase A current and tension at steady state to highlight the overlapping of the curves.

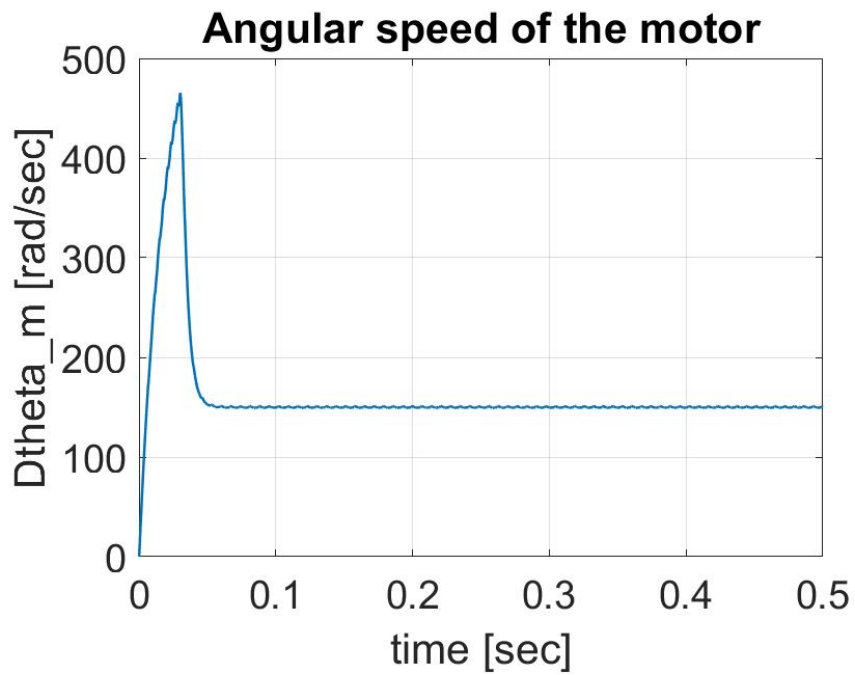


Figure 3.39: Angular speed of the motor

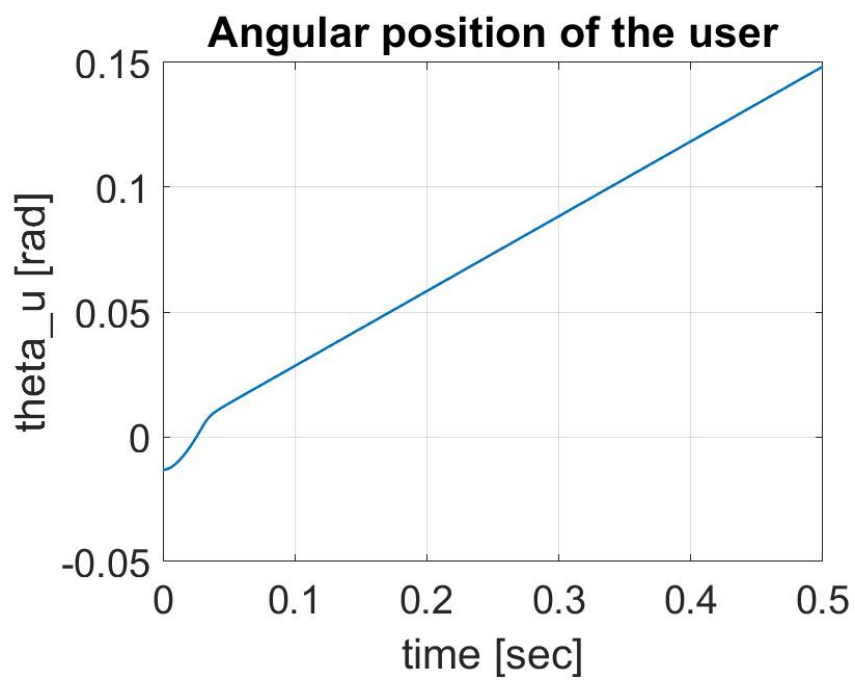


Figure 3.40: Angular position of the user

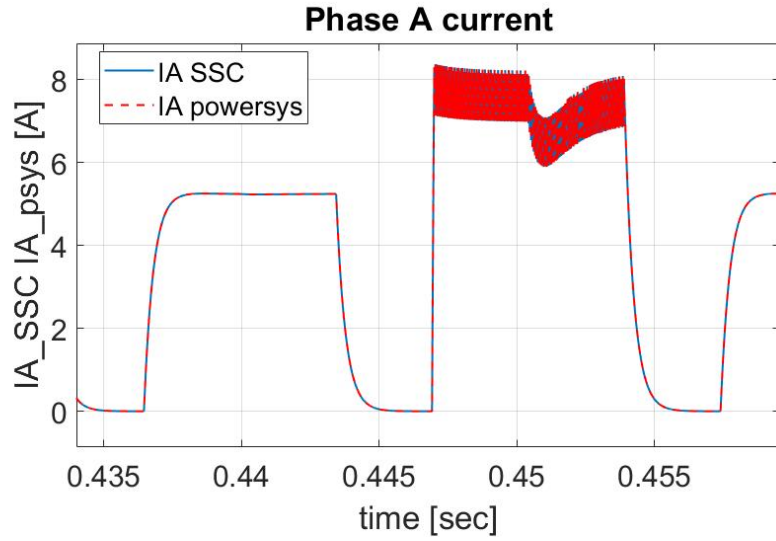


Figure 3.41: I_A at steady state

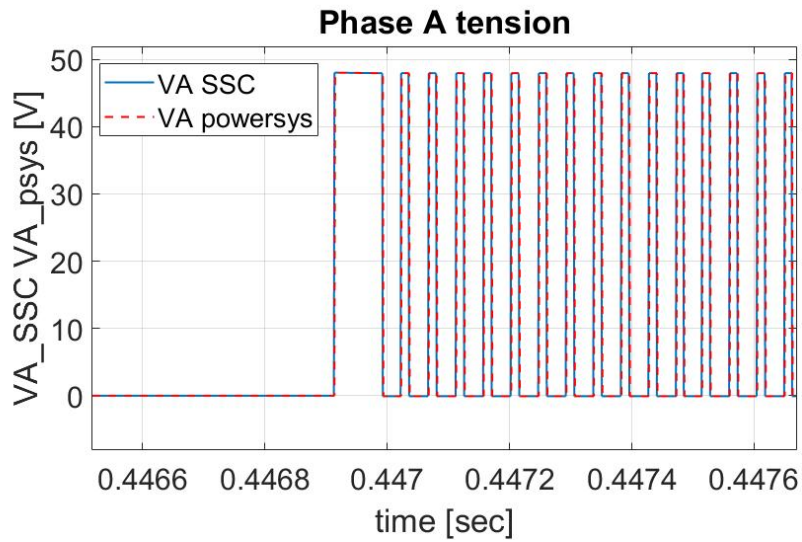


Figure 3.42: V_A at steady state

3.11.3 Sinusoidal command

The simulation parameters are reported in the table 3.4.

Input semiamplitude	Bias input	Input frequency	External load	Simulation time
0.5 rad	0 rad	1 Hz	0 Nm	0.5 sec

Table 3.4: Data sinusoidal command

The figures 3.43, 3.44 and 3.45 show respectively the trend of angular position and angular speed of the motor and angular position of the user.

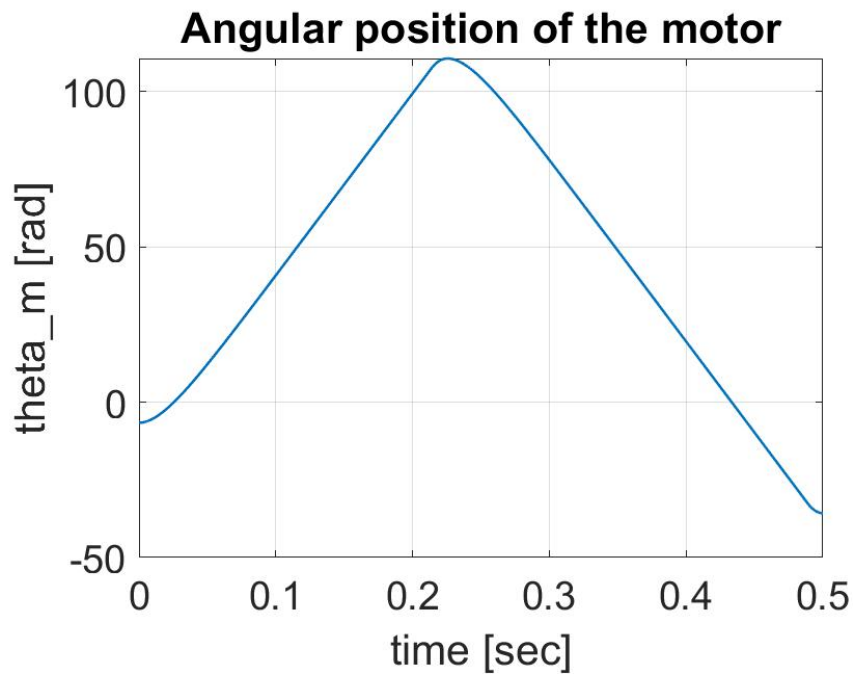


Figure 3.43: Angular position of the motor

The figures 3.46 and 3.47 show respectively the phase A current and tension at steady state to highlight the overlapping of the curves.

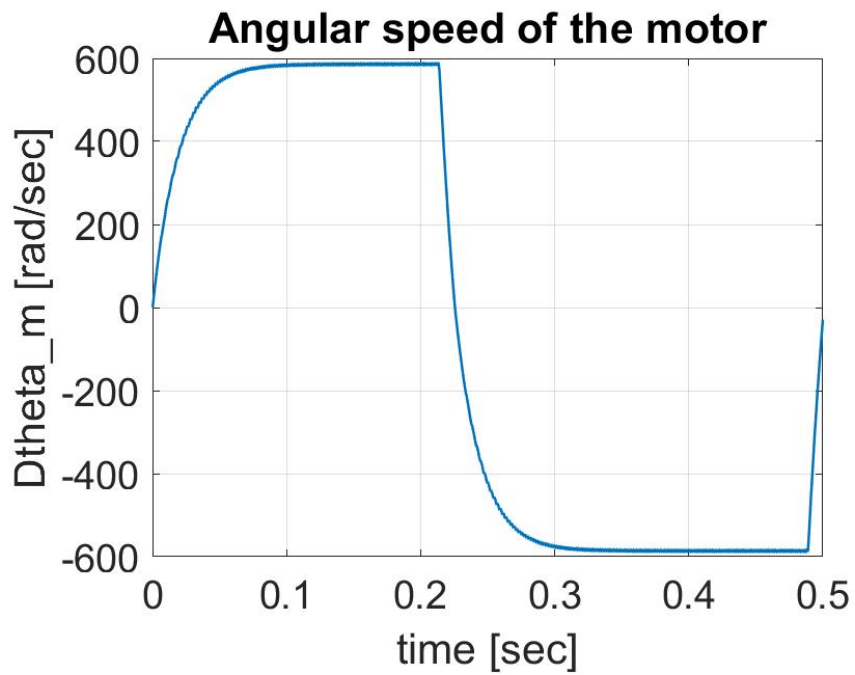


Figure 3.44: Angular speed of the motor

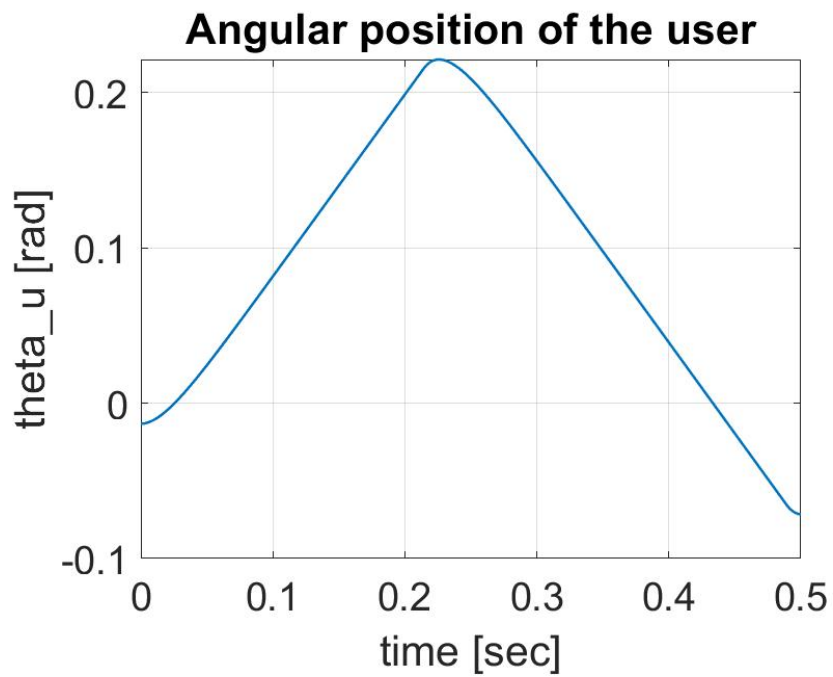


Figure 3.45: Angular position of the user

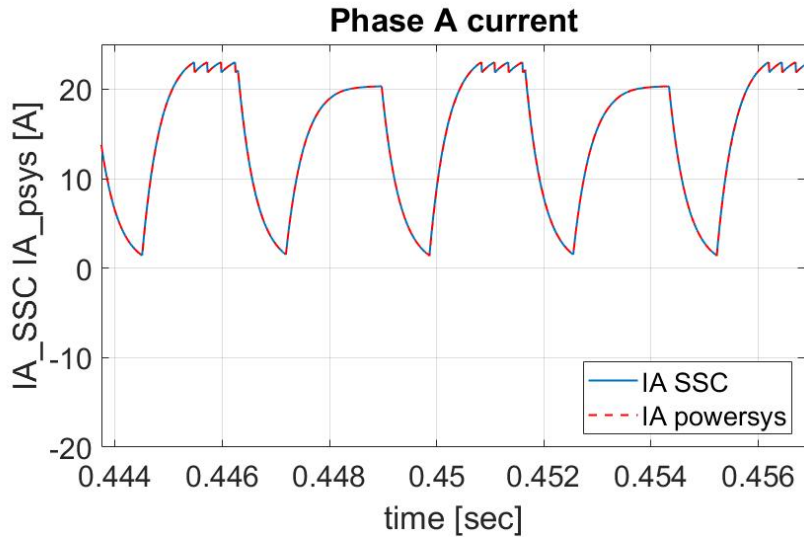


Figure 3.46: I_A at steady state

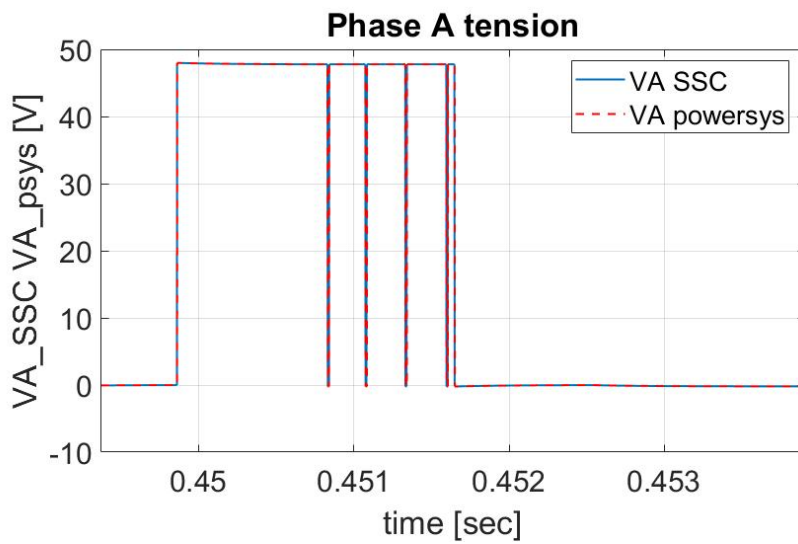


Figure 3.47: V_A at steady state

3.11.4 Step, ramp and external load

The figure 3.48 shows the combination of commands that was chosen for the simulation. In particular, a step command and a subsequent ramp command were chosen. Using the "Signal builder" block, it was possible to set the characteristics of the two commands by points for a period of time equal to the simulation time. The data are shown in the table 3.5.



Figure 3.48: Signal builder command

Step command			Ramp command	
t=0 sec	t=0.05 sec	t=0.2 sec	t=0.2 sec	t=0.5 sec
0 rad	0 rad - 0.1 rad	0.1 rad - 0 rad	0 rad	0.1 rad

Table 3.5: Characteristics of two commands

The external load was also set graphically via the "Signal builder" block as shown in the figure 3.49. The characteristics are shown in the table 3.6.

The figures 3.50, 3.51 and 3.52 show respectively the trend of angular position and angular speed of the motor and angular position of the user.

From the figure 3.51, it can be seen that the angular speed of the motor is reduced because at 0.35 sec an external load is applied which acts in the opposite direction to the direction of rotation of the motor and therefore acts as a brake. The reduction in speed produces a change in the slope of the curve on the angular position of the



Figure 3.49: Signal builder load

External load		
t=0 sec	t=0.35 sec	t=0.5 sec
0 Nm	0-150 Nm	150 Nm

Table 3.6: Characteristics of the external load

motor and consequently the user will also be slowed down.

The figures 3.53 and 3.54 show respectively the phase A current and tension at steady state to highlight the overlapping of the curves.

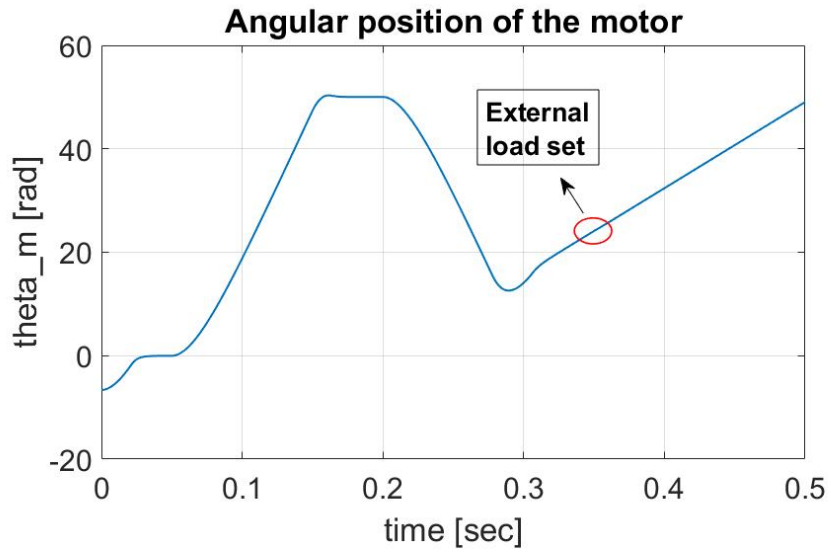


Figure 3.50: Angular position of the motor

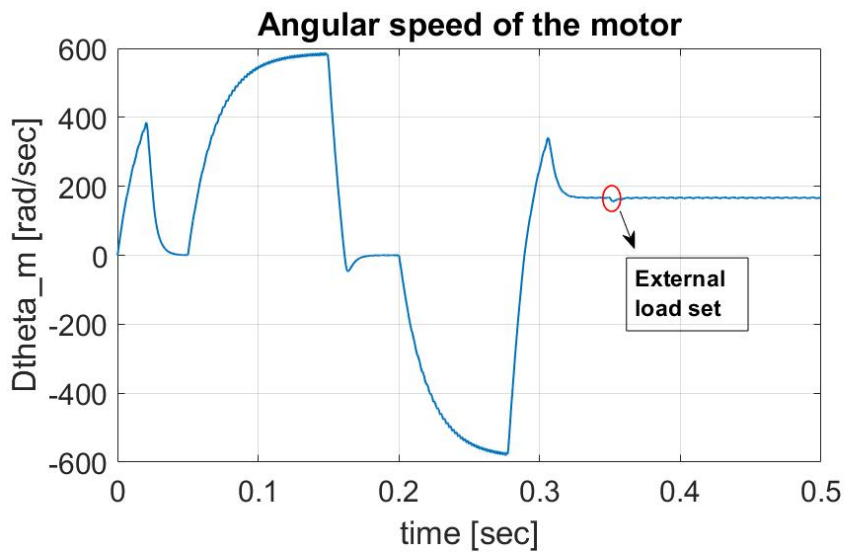


Figure 3.51: Angular speed of the motor

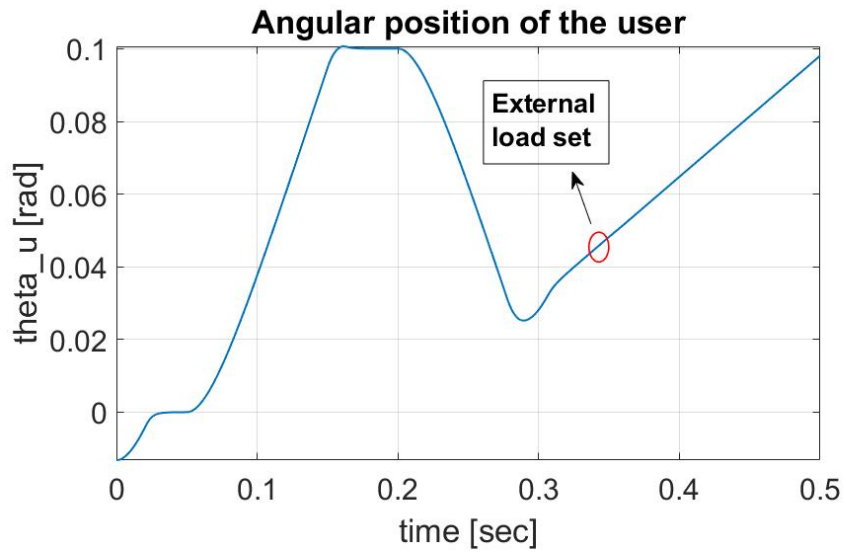


Figure 3.52: Angular position of the user

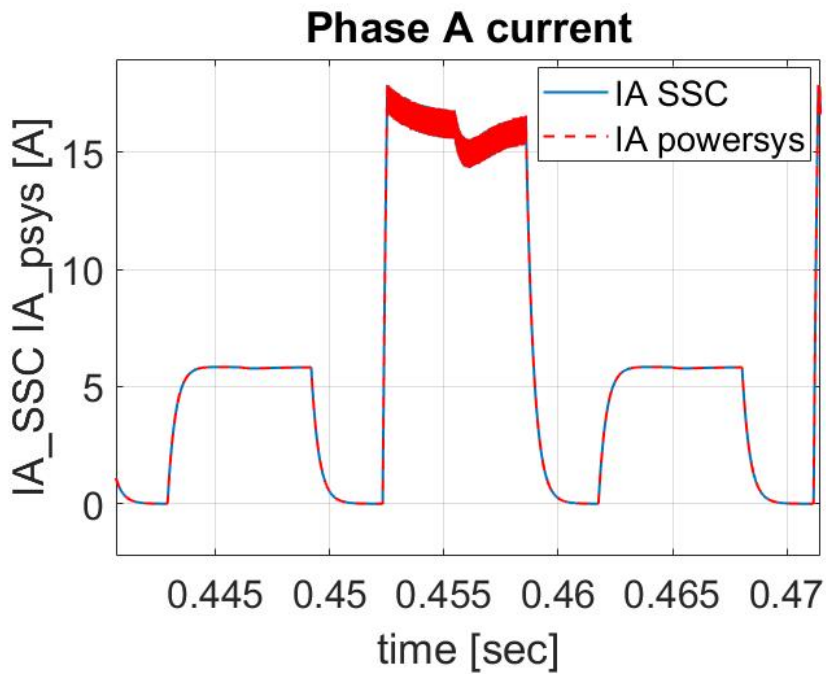


Figure 3.53: I_A at steady state

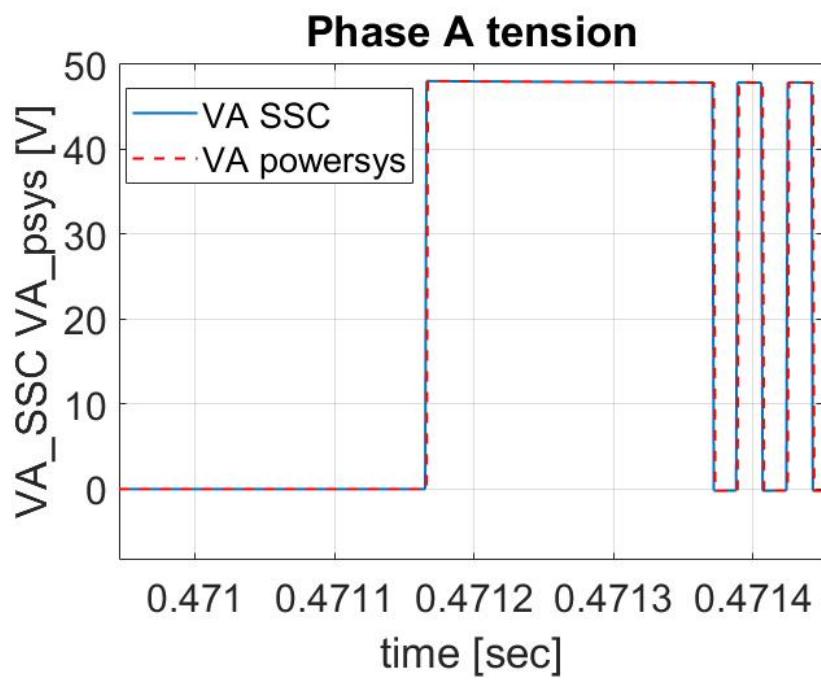


Figure 3.54: V_A at steady state

Chapter 4

Permanent Magnet Synchronous Motor (PMSM)

4.1 High-Fidelity model description

The construction and validation of the correct functioning of the model produced in Simscape was conducted on the HF model of the brushless DC motor. Since the test bench described in Chapter 2 is composed of a PMSM, it is necessary to validate the Simscape model also on the Simulink model of the PMSM to perform simulations of the operation of the motor actually present on the test bench.

The integration method adopted for the PMSM simulation is the fixed step Euler method (in Simulink *ode1 (Euler)*) with a time step of 10^{-6} s respecting the numerical convergence criteria already explained for the brushless DC motor model. The HF model of the PMSM in the figure 4.1 is described in detail hereafter, highlighting the most important differences with the HF model of the brushless DC motor.

4.2 Command block and external torque blocks

From the figure 4.2, the "Com" block allows you to choose between different input commands via a mask. The commands that can be inserted are step, ramp, sine command, chirp command or time history directly set by Matlab. The external load is set through a "Repeating Sequence" block through which it is possible to set the value of the load corresponding to the desired instant of time defined by a sequence of time steps. The two control signals for position and external load

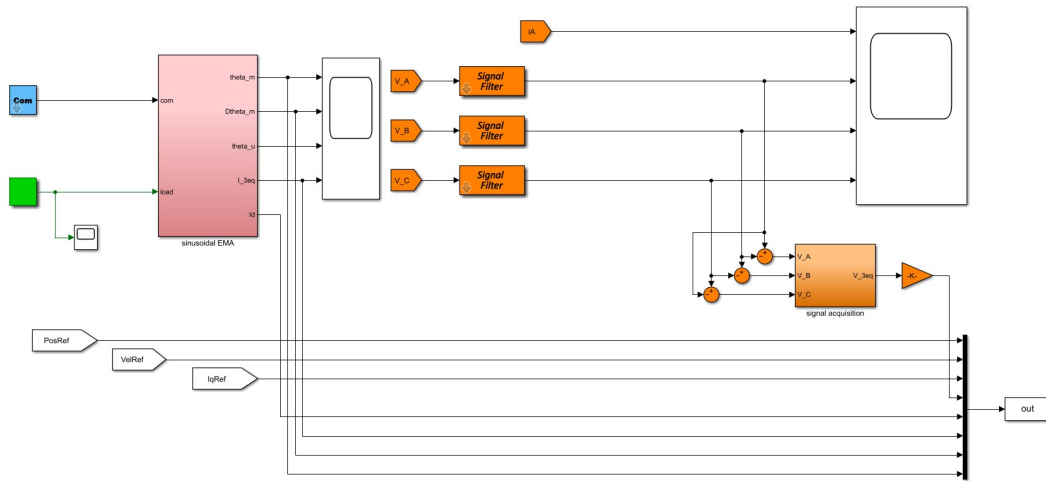


Figure 4.1: PMSM model subsystems

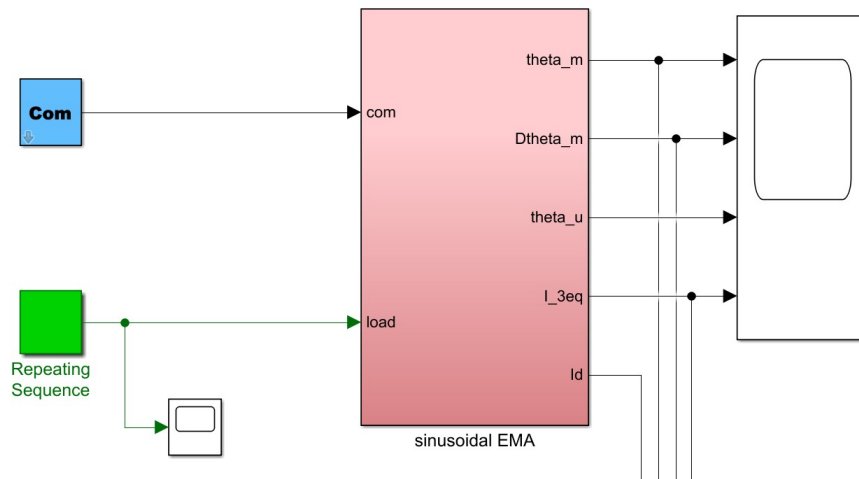


Figure 4.2: Command block and external torque blocks

are supplied as input to the "sinusoidal EMA" subsystem which implements the electromechanical operation of the PMSM on the test bench.

4.3 Sinusoidal EMA subsystems

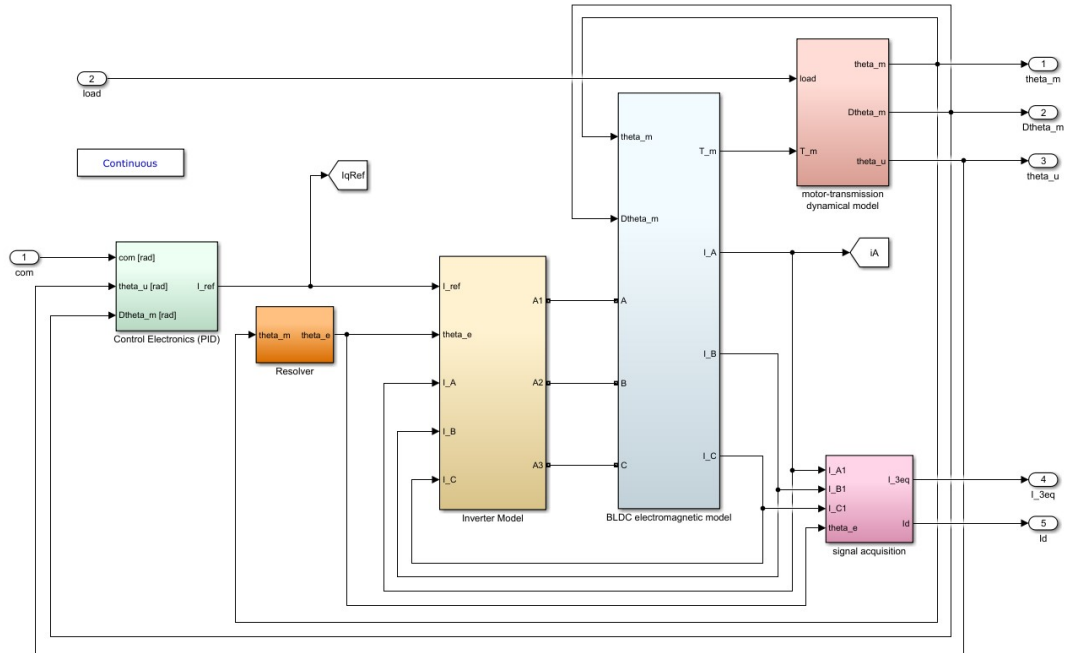


Figure 4.3: Sinusoidal EMA subsystem

It consists of several subsystems implementing different operating logics as shown in the figure 4.3.

4.4 Control Electronics PID subsystem

From the figure 4.4, the input angular position command is compared through a sum block to the user angular position (both signals are referred to the slow shaft) to obtain the position error signal. The latter is multiplied by a proportional gain to obtain the reference speed on the fast shaft and then saturated according to the maximum angular speed that the motor can deliver. The saturated angular reference speed is compared with the instantaneous angular speed of the motor, generating a speed error. This is fed into the PID controller, which also receives the position error and the instantaneous angular speed of the motor. The diagram of the PID controller is shown in the figure 4.5.

The PID controller shown in the figure 4.5 represents a much more complex control logic than the case seen in the brushless DC motor model. Its structure is described below.

It has three characteristic branches: the proportional branch, the integrative branch and the derivative branch.

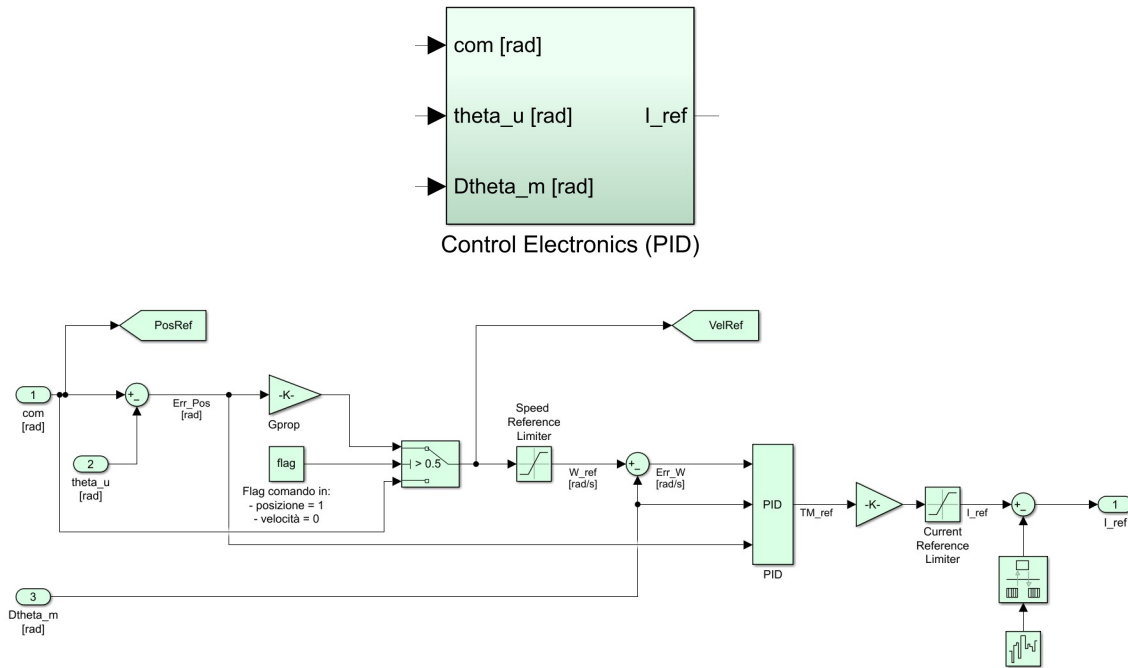


Figure 4.4: Control Electronics PID subsystem

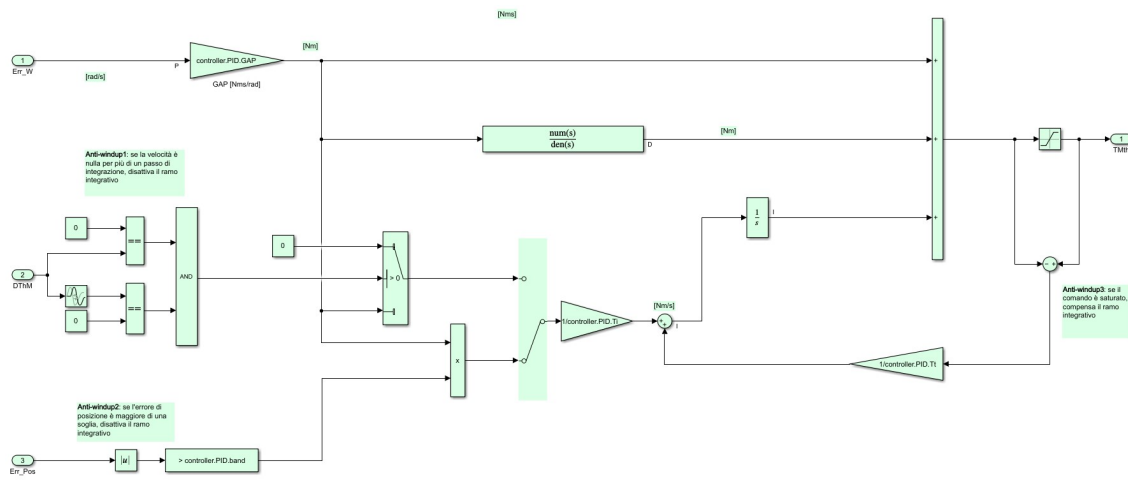


Figure 4.5: PID

- Proportional branch**
 It has the proportional gain GAP which multiplies the speed error. The branch produces a proportional response that works to cancel the error.
- Derivative branch**
 It has a "Transfer function" block that receives the product of the proportional

branch as input and implements the transfer function defined in the equation 4.1:

$$G(s) = \frac{T_d s}{\frac{T_d s}{N} + 1} \quad (4.1)$$

The derivative branch works on the derivative of the error, generating a response that dampens a sudden change in the error. In addition, the transfer function thus defined also acts as a "filter" through which the effects on error amplification caused by signal noise are reduced. In fact, working on the error derivative generally amplifies signal noise, which is stronger the smaller the integration step.

- **Integrative branch**

It generates a signal which is the integral of the product generated by the proportional branch and a gain defined as $1/T_i$. In addition, it is necessary to equip the integrative branch with anti-windup systems whose function is to manage the presence of non-linearities, such as friction and saturation, which compromise the correct operation of the integrative branch. An example would be the action of a saturation on the signal. This produces a difference between the commanded signal and the output signal, which is read by the integrating branch as an error to be reduced over time. Therefore, the effect of the integrating branch will be to overload the error. When the input signal falls within the saturation band, the error accumulated in the previous phase causes an unsuitable control signal that could generate instabilities. To avoid such problems, various anti-windup controls must be implemented.

1. **Anti-windup1 logic:** if the angular velocity is zero for more than one time integration step, the integrative branch is switched off.

In particular, the instantaneous value of the angular velocity and the value at the previous time step are measured, the latter through the use of the "Transport delay" block, and it is verified if both velocity values are zero. If this occurs, then the "AND" block returns the value 1 which activates the upper branch of the "switch" which provides 0 as input to the integrator block. In this way, the output contribution from the integrator remains constant and equal to the value it returned before the input signal became saturated. If, vice versa, the "AND" block returns a value of 0 at the output, the lower branch of the "switch" is activated supplying the integrator with the value at the output of the proportional branch. The zero speed condition can occur under various conditions, for example when there is a limit switch or when the system is subjected to a static friction force such that it does not move. In the latter case, an error is

produced which is integrated in time and the contribution of the integrating branch continues to increase until the action of the control logic produces a much greater force to set the system in motion again. The continuous alternation between the static and dynamic conditions of the system generates numerical limit cycles which can be avoided by means of anti-windup logic.

2. **Anti-windup2 logic:** if the position error is greater than a certain threshold, the integrative branch is deactivated.

This logic makes it possible to control the effects of friction by monitoring the position and not the speed of the system. In fact, it may happen that due to friction the system has a speed equal to zero for several time integration steps, so the logic previously described could be unusable and the system would remain at a standstill unless the action of the proportional branch has a contribution that would restart the system. In fact, the anti-windup2 logic is more efficient than the anti-windup1 logic.

3. **Anti-windup3 logic:** if the command is saturated the integrative branch is compensated.

Specifically, the torque command is saturated and is compared with the unsaturated torque value through an algebraic sum block. If the difference between the two signals is zero, it means that the system is not saturated, so there is no need to compensate. Conversely, the difference produces an error that is multiplied by a gain generate control action to be added to the integrating branch to reduce its contribution. The contributions generated by each branch of the PID controller are added together to generate the theoretical motor torque. This value is saturated to obtain the reference value of the output torque from the PID subsystem.

The reference torque is multiplied by a gain related to the constant counter-electromotive force of the motor to obtain the current signal. This value is then saturated to take account of the physical limits of the motor necessary to avoid potential short circuits caused by excessive overheating. The reference current is compared with a signal generated by the "Band-Limited White Noise" block, which introduces a fluctuation in the signal frequency to take account of any noise present (in this case the fluctuation is set to 0). The "Control Electronics (PID)" subsystem generates an output signal representing the single-phase reference current.

4.5 Resolver block subsystem

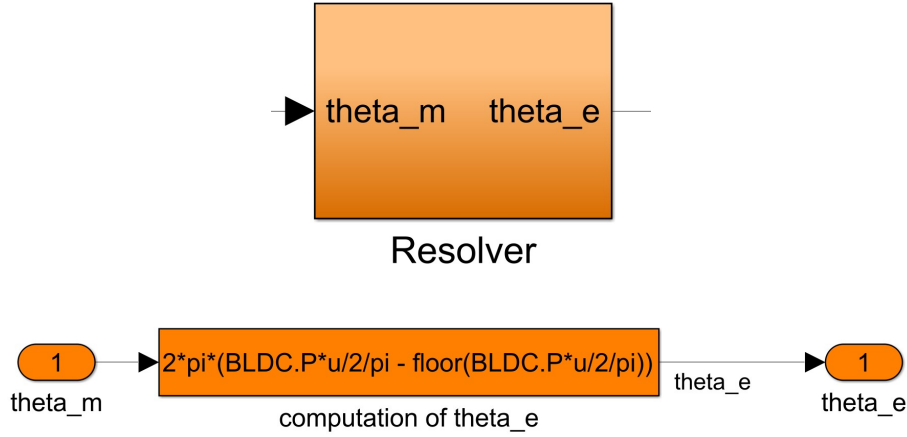


Figure 4.6: Resolver block subsystem

In the "Resolver" block, the mechanical signal of the angular position of the motor is converted into the corresponding electrical signal. The equation used is 4.2:

$$\vartheta_e = N_p \vartheta_m \quad (4.2)$$

where N_p is the number of motor pole pairs, ϑ_e is the electrical angle and ϑ_m is the mechanical angle. The expression given in the "computation of ϑ_e " block makes it possible to obtain an output signal ϑ_e always between 0 and 2π rad. The equation used is 4.3:

$$\vartheta_e = 2\pi \left(\frac{N_p \vartheta_m}{2\pi} - \text{floor} \left(\frac{N_p \vartheta_m}{2\pi} \right) \right) \quad (4.3)$$

4.6 Inverter subsystem

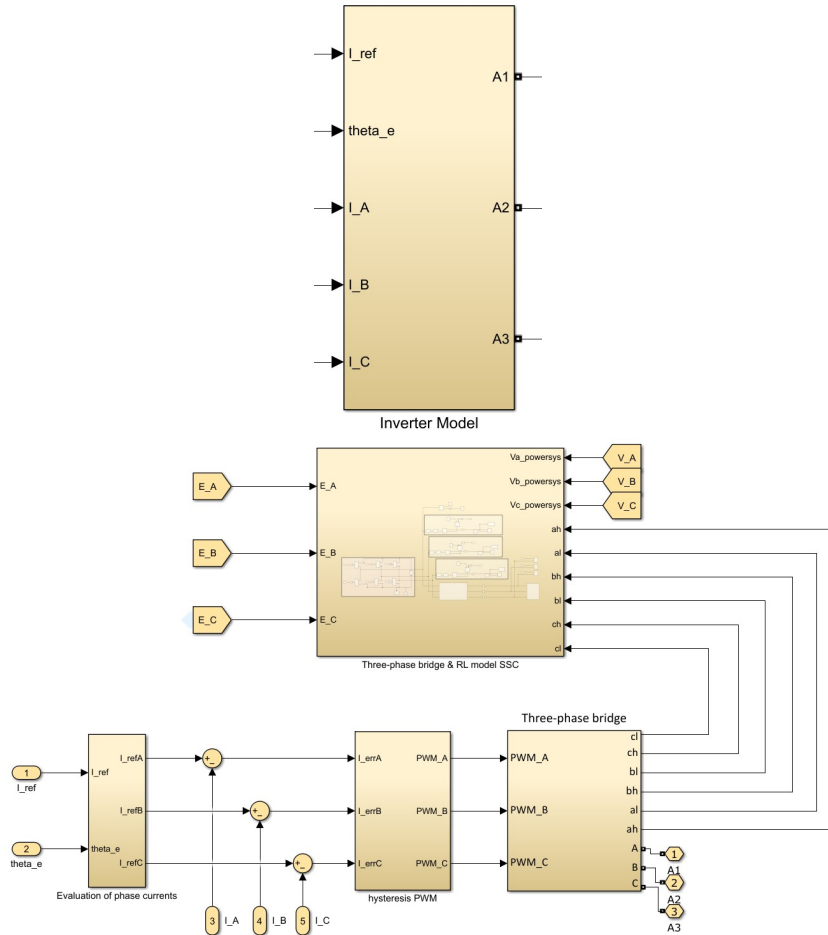


Figure 4.7: Inverter subsystem

The "Inverter" subsystem shown in the figure 4.7 consists of four other subsystems.

4.6.1 Evaluation of phase currents subsystem

Unlike the brushless DC motor model, the evaluation of the currents on the three phases of the stator circuit is not performed by means of the signals generated by the "Hall effect" blocks but by means of Clark-Park transformations subsystems shown in the figure 4.8. Using this system, it is possible to calculate the currents circulating on each phase as a function of the previously calculated reference current I_{ref} . In particular, it is necessary to calculate the inverse Clark-Park transformations. The following is the discussion.

Since the stator circuit is connected in a star configuration, it is first necessary

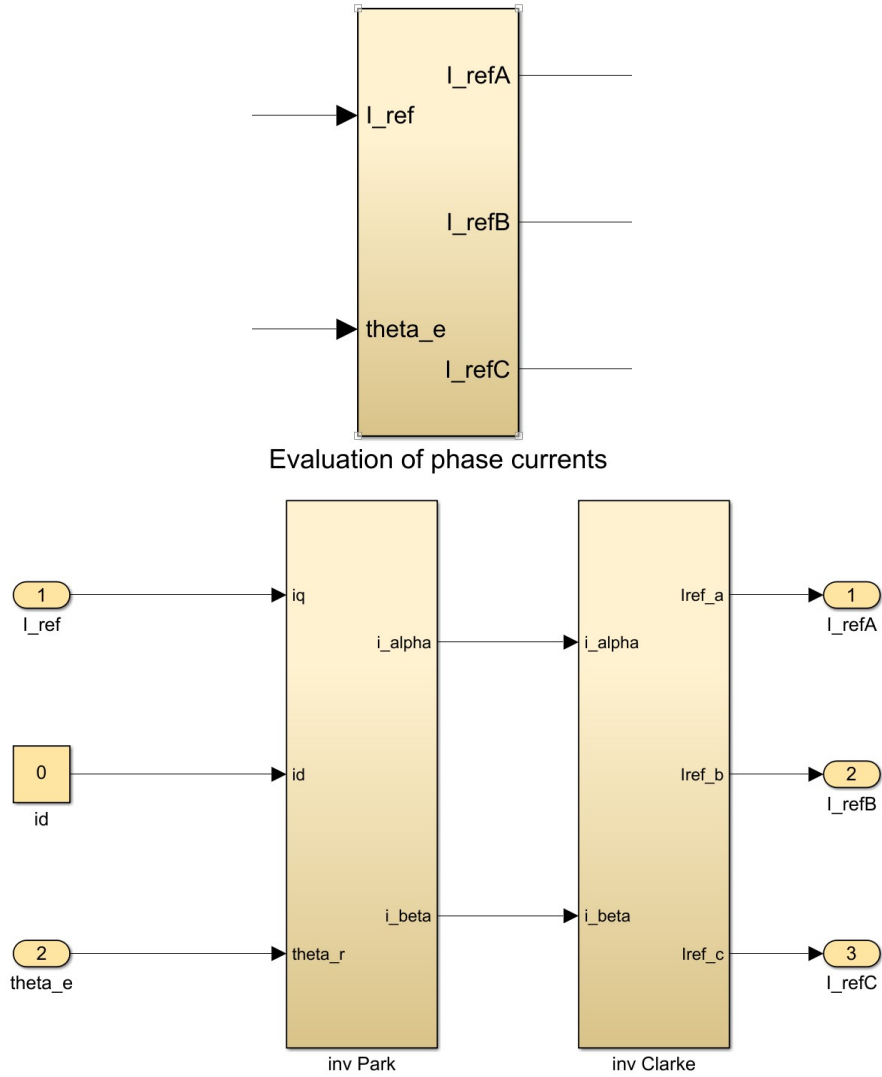


Figure 4.8: Evaluation of phase currents subsystem

to project the system of currents from a reference system A-B-C to a fixed, right-handed $\alpha - \beta$ reference system via the Clark matrix $[C]$. The algebraic expression of the Clark transformation is given by the equations:

$$\begin{Bmatrix} I_\alpha \\ I_\beta \end{Bmatrix} = [C] \begin{Bmatrix} I_A \\ I_B \\ I_C \end{Bmatrix} = \frac{2}{3} \begin{bmatrix} 1 & -\frac{1}{2} & -\frac{1}{2} \\ 0 & \frac{\sqrt{3}}{2} & -\frac{\sqrt{3}}{2} \end{bmatrix} \begin{Bmatrix} I_A \\ I_B \\ I_C \end{Bmatrix}$$

from which the currents in the $\alpha - \beta$ reference system can be calculated:

$$\begin{cases} I_\alpha = \frac{2}{3}I_A - \frac{1}{3}(I_B + I_C) \\ I_\beta = \frac{\sqrt{3}}{3}(I_B - I_C) \end{cases}$$

Park's transformation brings the currents I_α and I_β into a reference system integral with the rotor defined by two axes d and q with respect to which the direct current (aligned in the direction of the rotor's north pole) and the quadrature current (orthogonal to the magnetic field, which is the one that generates the maximum torque of the motor) are calculated respectively. Therefore, it is possible to calculate the currents in the new reference system \hat{d} and \hat{q} :

$$\begin{aligned} \begin{Bmatrix} I_d \\ I_q \end{Bmatrix} &= [P] \begin{Bmatrix} I_\alpha \\ I_\beta \end{Bmatrix} = \begin{bmatrix} \cos \vartheta_e & \sin \vartheta_e \\ -\sin \vartheta_e & \cos \vartheta_e \end{bmatrix} \begin{Bmatrix} I_\alpha \\ I_\beta \end{Bmatrix} \\ &\begin{cases} I_d = I_\alpha \cos \vartheta_e + I_\beta \sin \vartheta_e \\ I_q = -I_\alpha \sin \vartheta_e + I_\beta \cos \vartheta_e \end{cases} \end{aligned}$$

The complete Clark-Park transformation is defined:

$$\begin{Bmatrix} I_d \\ I_q \end{Bmatrix} = [P] \begin{Bmatrix} I_\alpha \\ I_\beta \end{Bmatrix} = [P][C] \begin{Bmatrix} I_A \\ I_B \\ I_C \end{Bmatrix} = \frac{2}{3} \begin{bmatrix} 1 & -\frac{1}{2} & -\frac{1}{2} \\ 0 & \frac{\sqrt{3}}{2} & -\frac{\sqrt{3}}{2} \end{bmatrix} \begin{bmatrix} \cos \vartheta_e & \sin \vartheta_e \\ -\sin \vartheta_e & \cos \vartheta_e \end{bmatrix} \begin{Bmatrix} I_A \\ I_B \\ I_C \end{Bmatrix}$$

From which it is possible to calculate the expression of the direct current I_d and the quadrature current I_q as a function of the electrical angle ϑ_e and the currents circulating on each phase I_A, I_B, I_C .

$$\begin{cases} I_d = \left[\frac{2}{3}I_A - \frac{1}{3}(I_B + I_C) \right] \cos \vartheta_e + \frac{\sqrt{3}}{3}(I_B - I_C) \sin \vartheta_e \\ I_q = - \left[\frac{2}{3}I_A - \frac{1}{3}(I_B + I_C) \right] \sin \vartheta_e + \frac{\sqrt{3}}{3}(I_B - I_C) \cos \vartheta_e \end{cases}$$

The figure 4.9 shows the three reference systems adopted for the transformations.

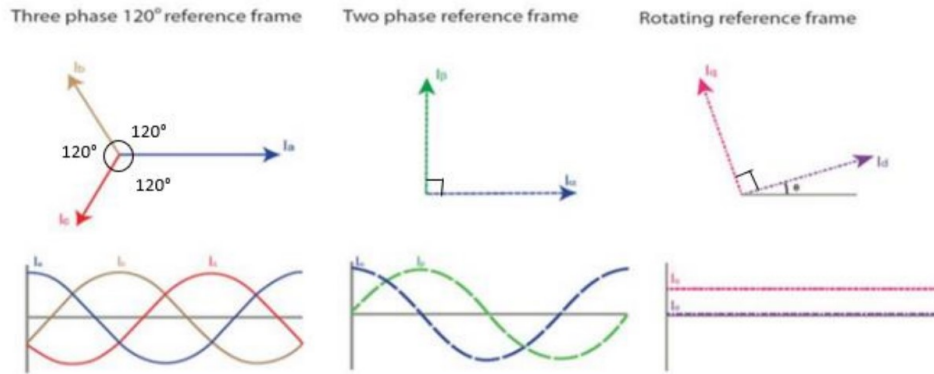


Figure 4.9: Reference system transformation

However, the model analysed relies on knowledge of the direct current I_d and quadrature current I_q to calculate the current circulating on each phase, so the inverse Clark-Park transformation must be used.

- **Inverse Park transformation**

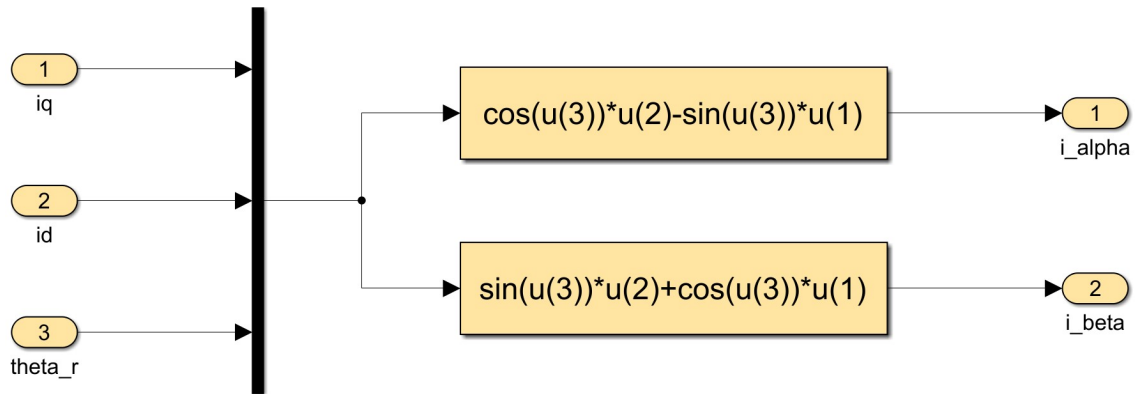
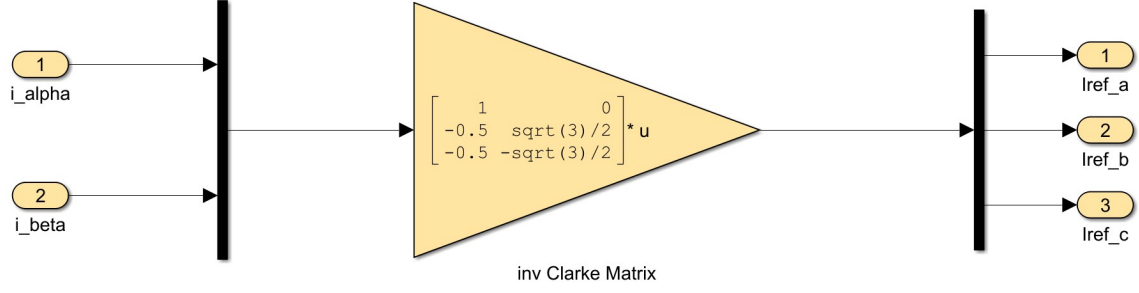


Figure 4.10: Inverse Park matrix

Since the matrix P is orthogonal, the inverse matrix coincides with the transposed matrix.

$$[P]^{-1} = \begin{bmatrix} \cos \vartheta_e & -\sin \vartheta_e \\ \sin \vartheta_e & \cos \vartheta_e \end{bmatrix}$$

- **Inverse Clark transformation**


Figure 4.11: Inverse Clark matrix

The Clark matrix, however, is not square, so the pseudo-inverse matrix must be calculated.

$$[C]^{-1} = \begin{bmatrix} 1 & 0 \\ -\frac{1}{2} & \frac{\sqrt{3}}{2} \\ -\frac{1}{2} & -\frac{\sqrt{3}}{2} \end{bmatrix}$$

Therefore, the inverse Clark-Park transformation will be:

$$\begin{Bmatrix} I_A \\ I_B \\ I_C \end{Bmatrix} = [C]^{-1} \begin{Bmatrix} I_\alpha \\ I_\beta \end{Bmatrix} = [C]^{-1} [P]^{-1} \begin{Bmatrix} I_d \\ I_q \end{Bmatrix} = \begin{bmatrix} 1 & 0 \\ -\frac{1}{2} & \frac{\sqrt{3}}{2} \\ -\frac{1}{2} & -\frac{\sqrt{3}}{2} \end{bmatrix} \begin{bmatrix} \cos \vartheta_e & -\sin \vartheta_e \\ \sin \vartheta_e & \cos \vartheta_e \end{bmatrix} \begin{Bmatrix} I_d \\ I_q \end{Bmatrix}$$

From which the expression for calculating the current on each phase can be obtained.

$$\begin{cases} I_A = I_d - I_q \sin \vartheta_e \\ I_B = \frac{1}{2} \left[(\sqrt{3} I_q - I_d) \cos \vartheta_e + (\sqrt{3} I_d + I_q) \sin \vartheta_e \right] \\ I_C = \frac{1}{2} \left[(-\sqrt{3} I_q - I_d) \cos \vartheta_e + (-\sqrt{3} I_d + I_q) \sin \vartheta_e \right] \end{cases}$$

From the figure 4.7, the signals I_{refA} , I_{refB} , I_{refC} are compared with the currents instantaneously circulating on the stator windings through algebraic sum blocks. The output of the three sum blocks will be the corresponding current error which is the input for the "hysteresis PWM" subsystem. Subsequently, the model implements the calculation of the active currents on the stator windings. In particular, the subsystem "Hysteresis PWM" allows the PWM power supply technique to be modelled, and the subsystem "Three-phase bridge" models the operation of the three-phase bridge with six Mosfet-type power transistors that allow the switching

of the phases. In addition, there is a further subsystem, "Three-phase bridge and RL model SSC", which implements the operation of the inverter and the three-phase stator circuit in the Simscape environment. The operation of the listed subsystems has already been described in detail in the previous Chapter 3 regarding the brushless DC motor model.

4.7 BLDC electromagnetic model subsystem

The BLDC electromagnetic model subsystem is shown in the figure 4.12.

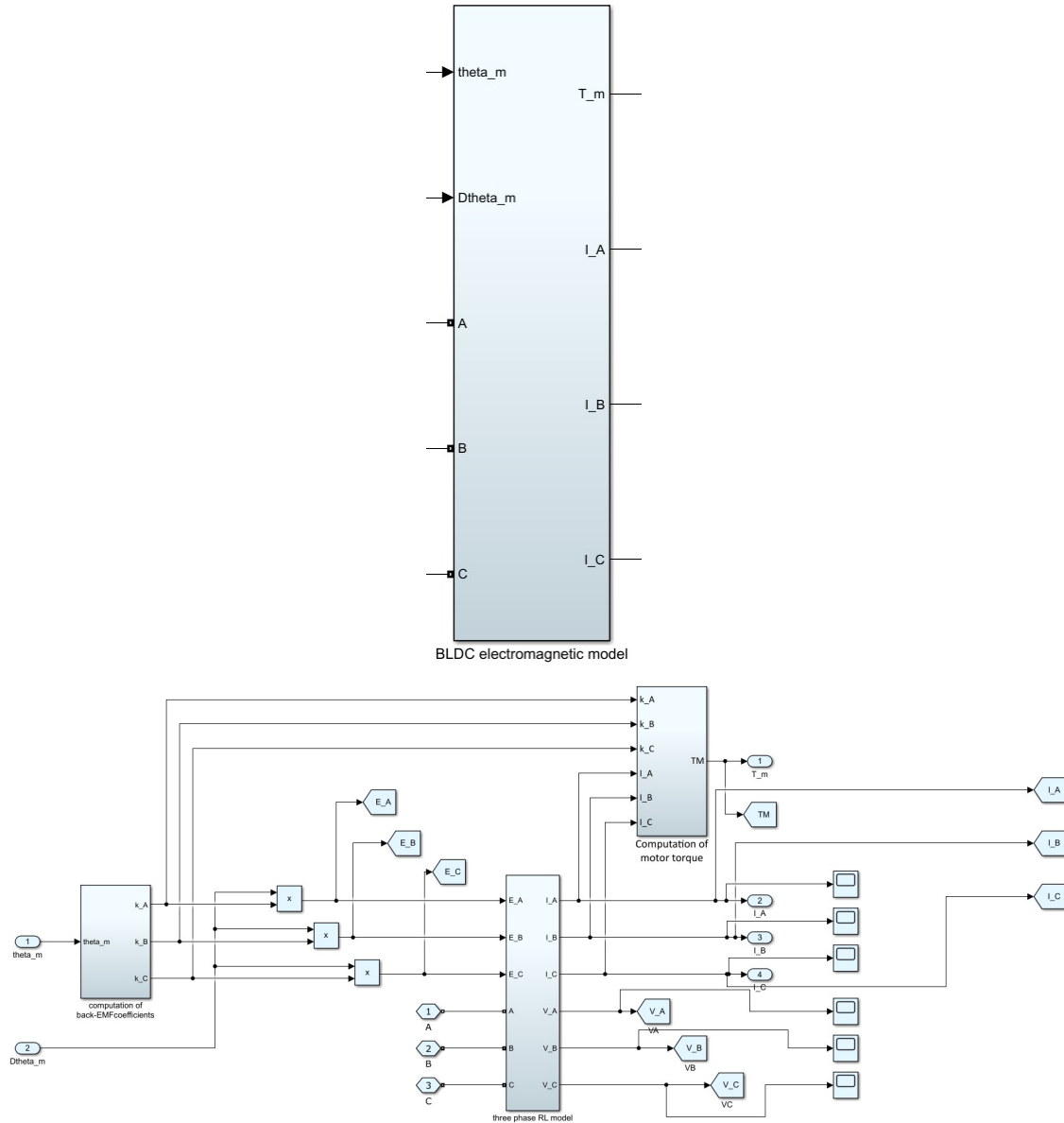


Figure 4.12: BLDC electromagnetic model subsystem

4.7.1 Computation of back-EMF coefficients subsystem

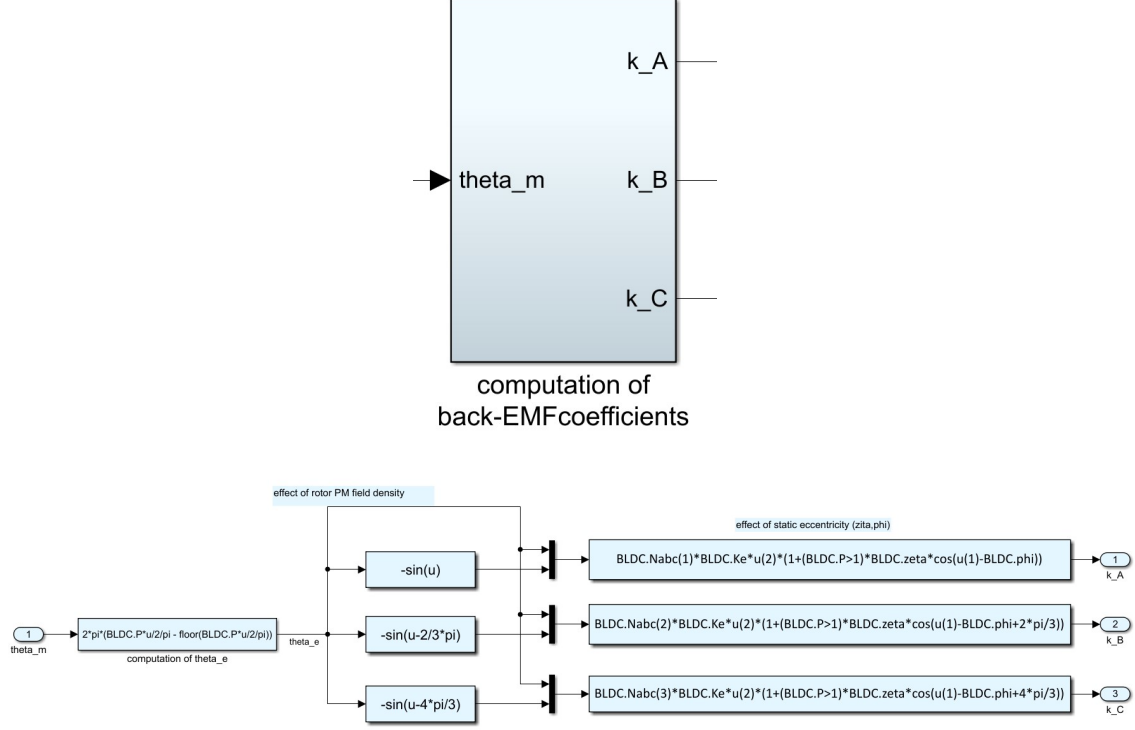


Figure 4.13: Computation of back-EMF coefficients subsystem

The input motor angular position signal is converted from a mechanical signal to an electrical signal in the same way as described in the equation 4.3. At this point, it is necessary to calculate the nominal counter-electromotive force on each phase of the motor stator circuit. This operation is performed in a different way to that seen for the brushless DC motor model since the waveform to be implemented is no longer trapezoidal but sinusoidal. This characteristic, which is at the apex of the difference between the PMSM and the brushless DC motor, is modelled in the "effect of rotor PM field density" section by means of three "Function" blocks, as shown in the figure 4.13, which make it possible to generate sinusoidal signals that are 120° out of phase with each other. The signals of the three sine waves and ϑ_e are used in the "effect of static eccentricity (ζ, ϕ)" section to implement two different faults, such as a potential short circuit of the stator windings and the effect of rotor eccentricity. The relation allowing the description of such phenomena is 4.4:

$$K_{fcm}^{(i)} = N_i K_e^{(i)} f(\vartheta_e) \cdot \left(1 + \zeta \cos \left(\vartheta_e - \varphi + \frac{2(i-1)}{3} \pi \right) \right) \quad (4.4)$$

where $K_e^{(i)} f(\vartheta_e)$ is the waveform of the normalised counter-electromotive force for each individual motor phase without faults, evaluated in the lookup table above, ζ is the ratio of rotor eccentricity and nominal air gap, N_i is the fraction of active coils of the i -th phase and φ is the static eccentricity phase.

At the output of the "Computation of back-EMF coefficients" subsystem, the three counter-electromotive force constants k_A , k_B , k_C are multiplied by $\dot{\vartheta}_m$ to calculate the counter-electromotive force acting on each phase of the stator circuit E_A , E_B , E_C . The "three phase RL model" subsystem makes it possible to calculate, taking into account the counter-electromotive force acting on each phase E_A , E_B , E_C respectively, the voltages and currents active on each winding. The latter, together with the signals k_A , k_B , k_C , enter the "computation of motor torque" subsystem, which calculates the motor torque generated by the electric motor. The operation of these subsystems is identical to that described in detail in the previous Chapter 3 regarding the brushless DC motor.

4.8 Signal acquisition subsystem

The characterisation of the PMSM model includes an additional subsystem called "signal acquisition" which introduces modifications to the measurement of the voltages acting on each stator phase to obtain results in line with those obtained from the experiments conducted on the test bench. The diagram is shown in the figure 4.14.

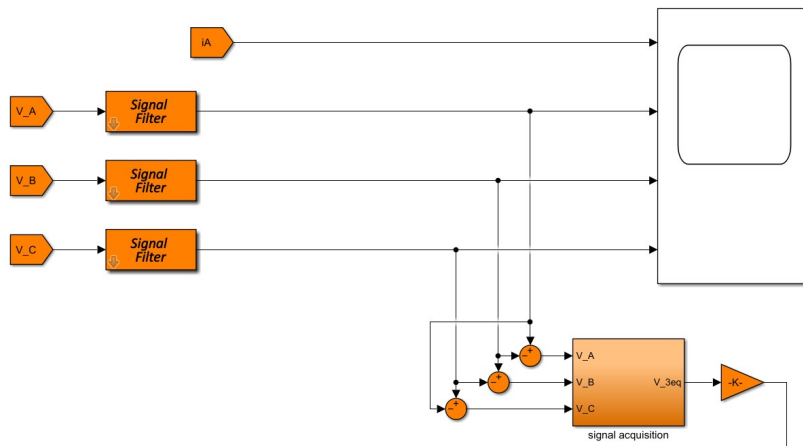


Figure 4.14: Signal acquisition

The voltage signal characteristic of each phase V_A , V_B , V_C passes through the "Signal filter" block which implements the operation of three first-order filters placed in series to eliminate any noise and signal fluctuations. Subsequently, the voltage acting on a specific phase of the stator is subtracted from the voltage acting on the

adjacent phase to obtain the following signals: $(V_A - V_B)$, $(V_B - V_C)$, $(V_C - V_A)$. These signals are input to the "signal acquisition" subsystem, whose structure is represented in the figure 4.15.

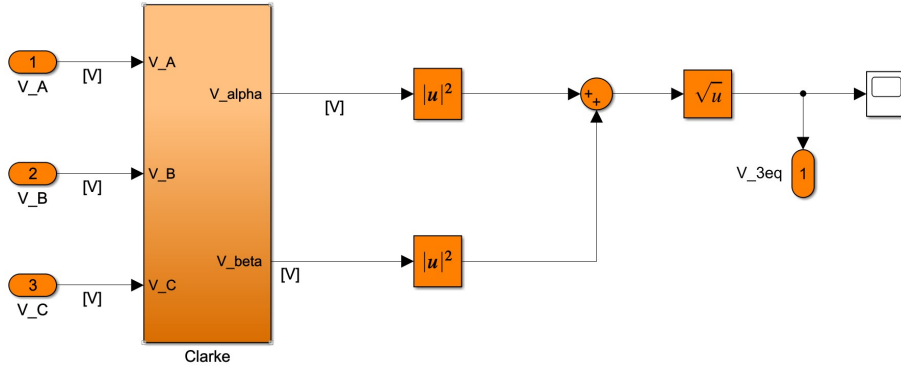


Figure 4.15: Clarke transformation

At the input of the "Clark" subsystem, which implements the direct Clark transformation, the differences of the voltages just obtained enter.

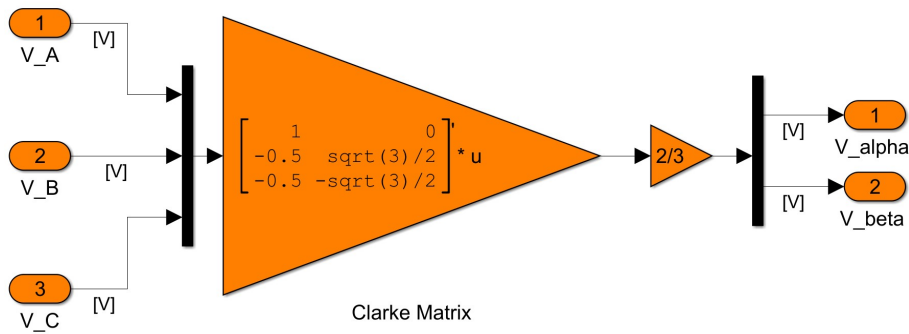


Figure 4.16: Clarke matrix

By means of the Clark matrix shown in the figure 4.16, it is possible to convert the three signals into voltage in a reference system with only two coordinates α and β to obtain, analogously to what is done for currents, the voltages V_α and V_β . Next, the square root of the sum of the square of the absolute value of the two signals is determined to obtain the absolute magnitude of the total voltage. Finally, this value is multiplied by $1/\sqrt{2}$ to obtain the voltage value in rms.

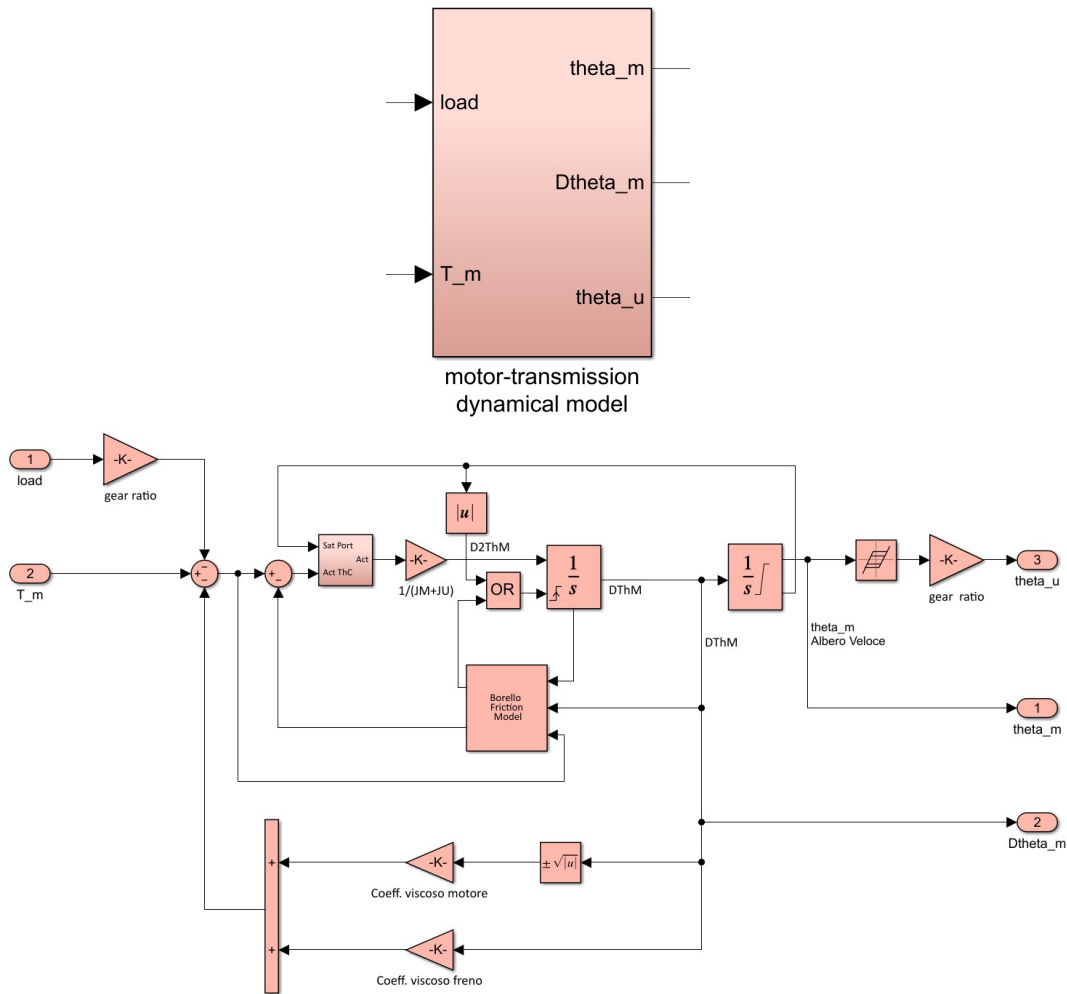


Figure 4.17: Motor transmission dynamical model subsystem

4.9 Motor transmission dynamical model subsystem

- **Viscous model**

Unlike what was seen for the brushless DC motor model, the characterisation of the HF model of the PMSM on the test bench made it possible to highlight a further phenomenon which must necessarily be taken into account during modelling. Initially, the contribution of the torque generated by the viscous actions was assumed to be linear with the angular speed of the motor. In reality, the bench tests showed that only the contribution of the viscous action of the braking module was linear with the angular speed, while that provided by the PMSM was a function of the square root of the angular speed. In fact,

it can be seen from figure 4.17 that the characteristic viscosity coefficient of the motor multiplies the square root of the angular speed and then adds the contribution of the brake viscosity, which has a linear relationship.

- **Borello friction model**

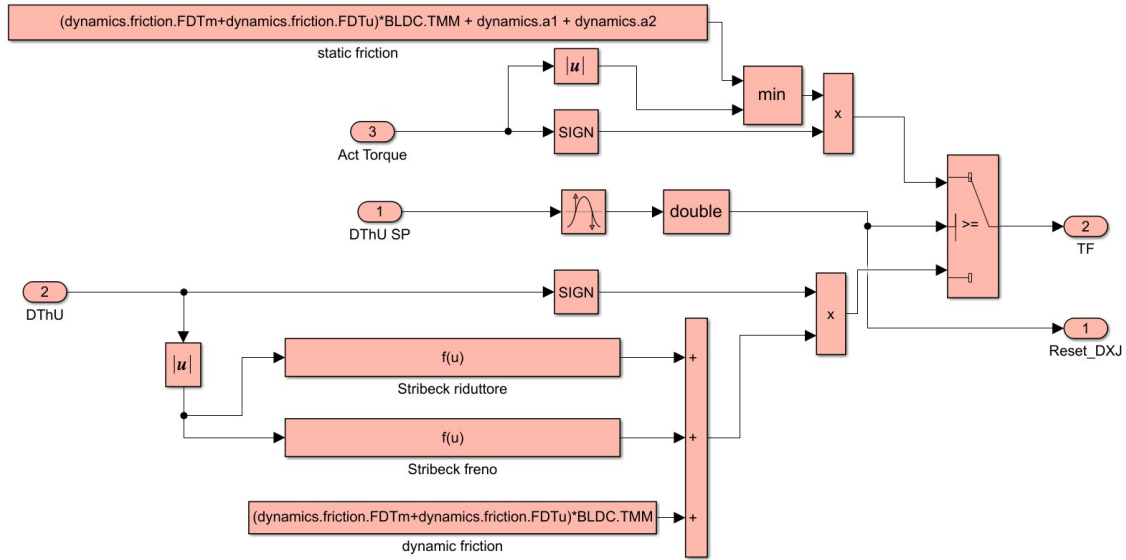


Figure 4.18: Borello friction model

The Borello friction model of the PMSM is different from that of the brushless DC motor in that it implements the relationships linked to the Stribeck curve which takes into account the variation of the friction coefficient for very low speeds and close to zero. The simulations on the test bench have shown that the friction torque produced by the gearbox and the brake decreases for very low angular speed values. This phenomenon is taken into account by means of Gaussian curves describing the trend of the points for speeds close to zero. The equations are implemented in the two blocks "Stribeck gearbox" and "Stribeck brake" as the figure 4.18 shows, which receive as input the absolute value of the angular speed and return two torque contributions which are added to the dynamic friction torque. In addition, the calculation of the static friction torque has also been modified in that it is evaluated by adding the value of the dynamic friction torque and the maximum of the Gaussian curves.

4.10 PMSM Simscape model validation

Similarly to what was seen for the validation of the Simscape model for the brushless DC motor, several simulations have been conducted in parallel between the numerical HF model produced in Simulink and the physical model produced in Simscape to validate the effectiveness of the latter in faithfully reproducing the same values and trends of the characteristic quantities of the system. In particular, the interest falls only on the voltages and currents acting in the stator circuit since the Simscape model under examination has been produced to simulate the operation of the three-phase bridge and the electromagnetic effects on the windings.

In the following analyses, the graphs of the mechanical quantities of the system, voltages and currents are shown. Only for the case of the "step command" the trends of all three voltages and currents are shown; for the other commands only the trend of the voltage and current on phase A is shown for reasons of synthesis. The graphs of all the characteristic quantities are shown in Appendix B.

4.10.1 Step command

The simulation parameters are reported in the table 4.1.

Initial amplitude	Final amplitude	Instant of application	External load	Simulation time
0 rad	0.5 rad	0.01 sec	0 Nm	0.5 sec

Table 4.1: Data step command

The figures 4.19, 4.20, 4.21 show respectively the trend of angular position and speed of the motor and angular position of the user.

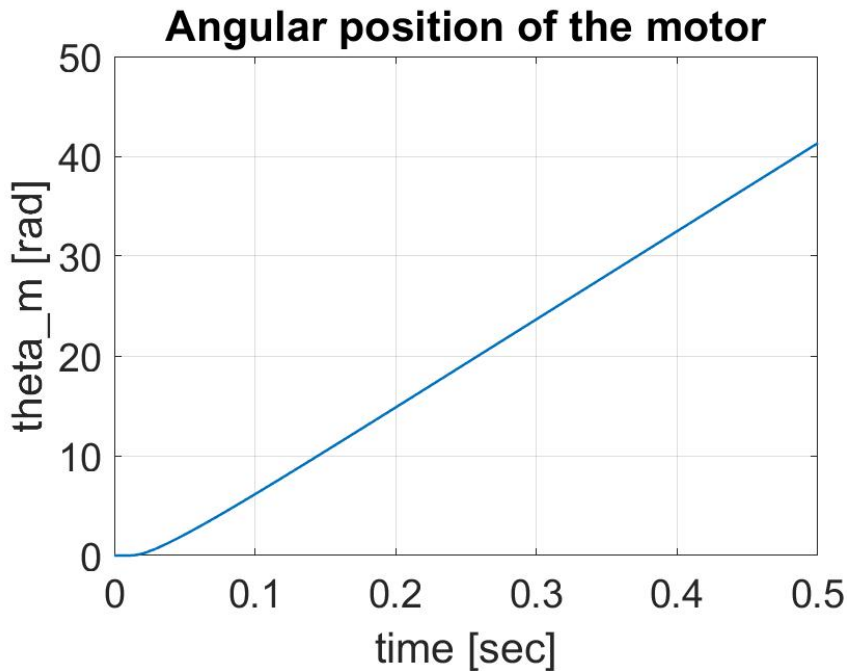


Figure 4.19: Angular position of the motor

The figures 4.22, 4.24 and 4.26 show respectively the trend of phase A, B, C current throughout the simulation. The figures 4.23, 4.25, 4.27 show respectively the trend of phase A, B and C current at steady state. Unlike the brushless DC motor model, the PMSM has a sinusoidal current pattern. This is due to the fact that the control logic signal is now characterised by three sine waves offset by 120° , so that the induced magnetic field, the counter-electromotive force and the currents on each phase will also have a sinusoidal pattern [9].

The figures 4.28, 4.30 and 4.32 show respectively the trend of phase A, B and C tension throughout the duration of the simulation. The figures 4.29, 4.31, 4.33 show

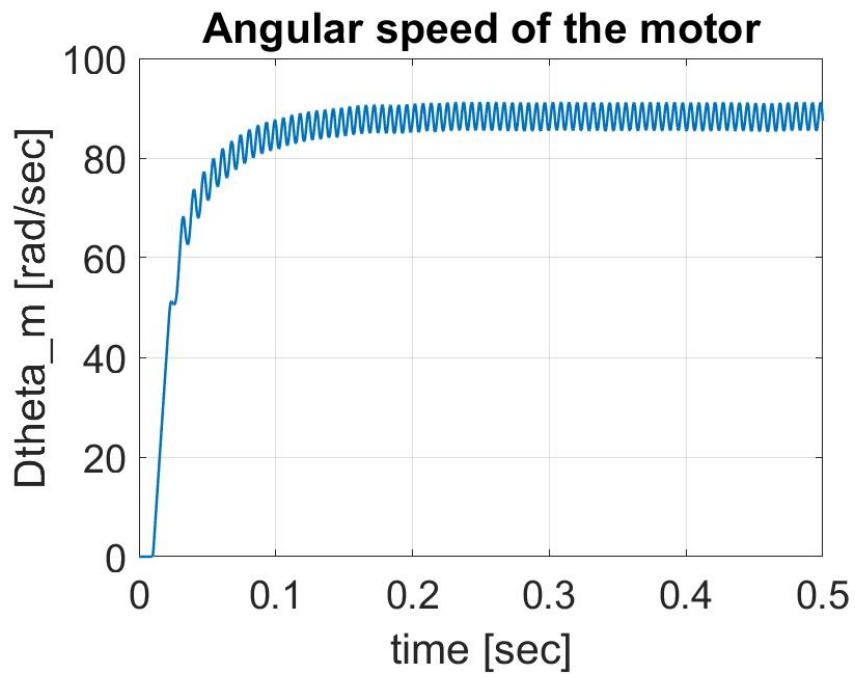


Figure 4.20: Angular speed of the motor

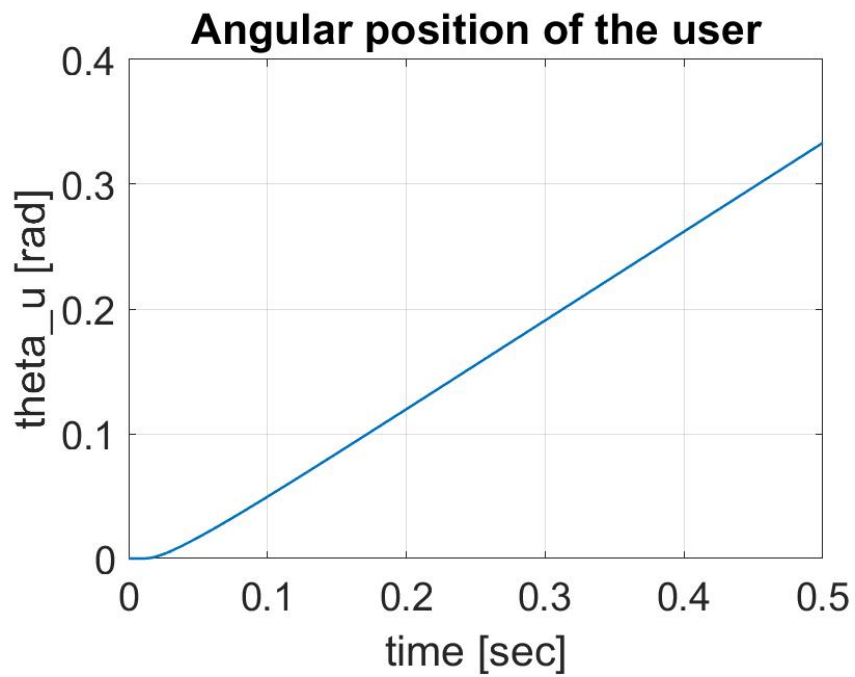


Figure 4.21: Angular position of the user

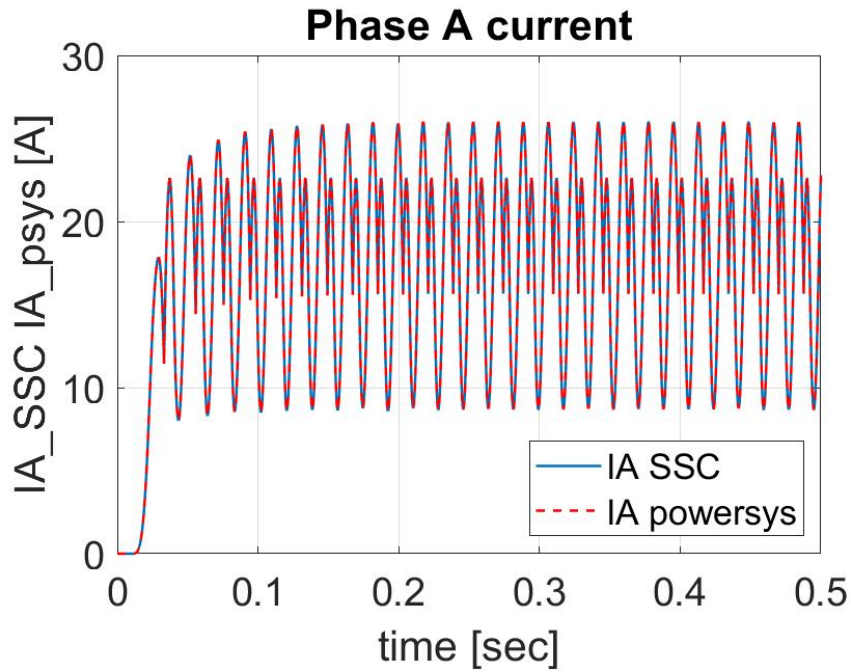


Figure 4.22: I_A

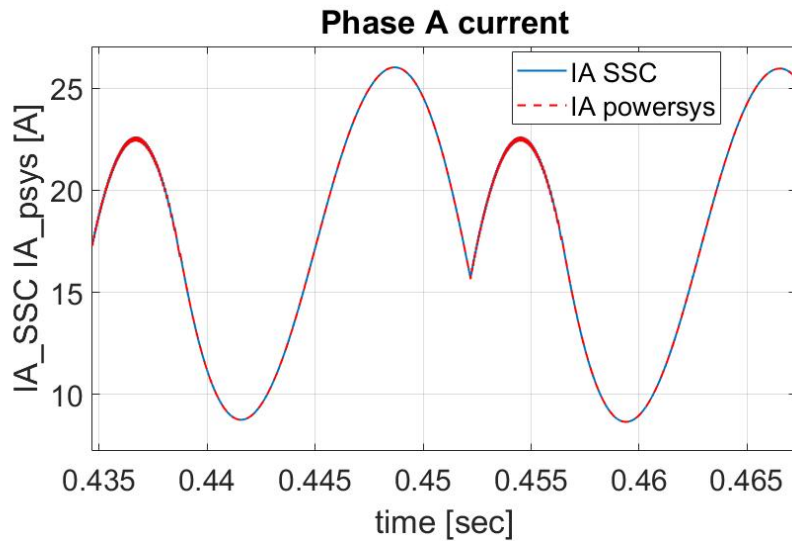


Figure 4.23: I_A at steady state

respectively the trend of phase A, B and C tension at steady state highlighting the overlap of two curves of the two respective models.

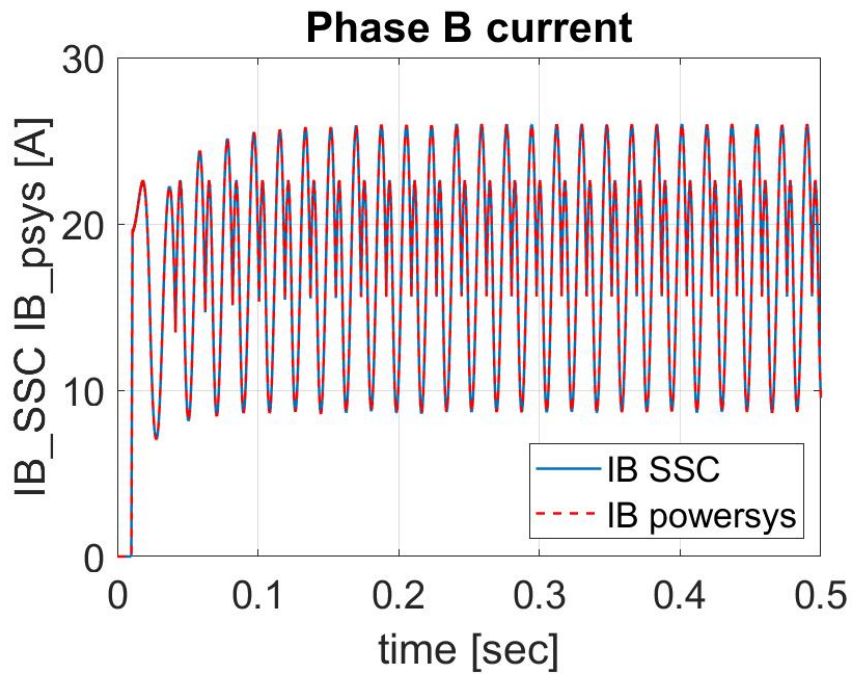


Figure 4.24: I_B

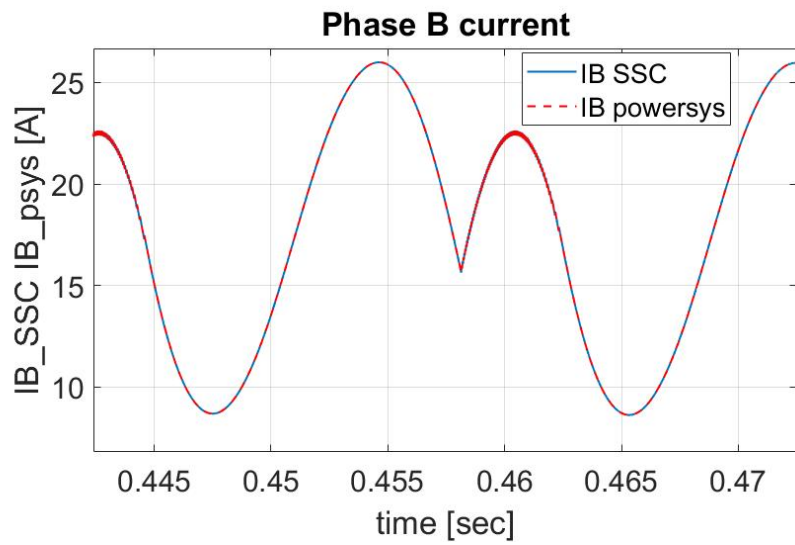


Figure 4.25: I_B at steady state

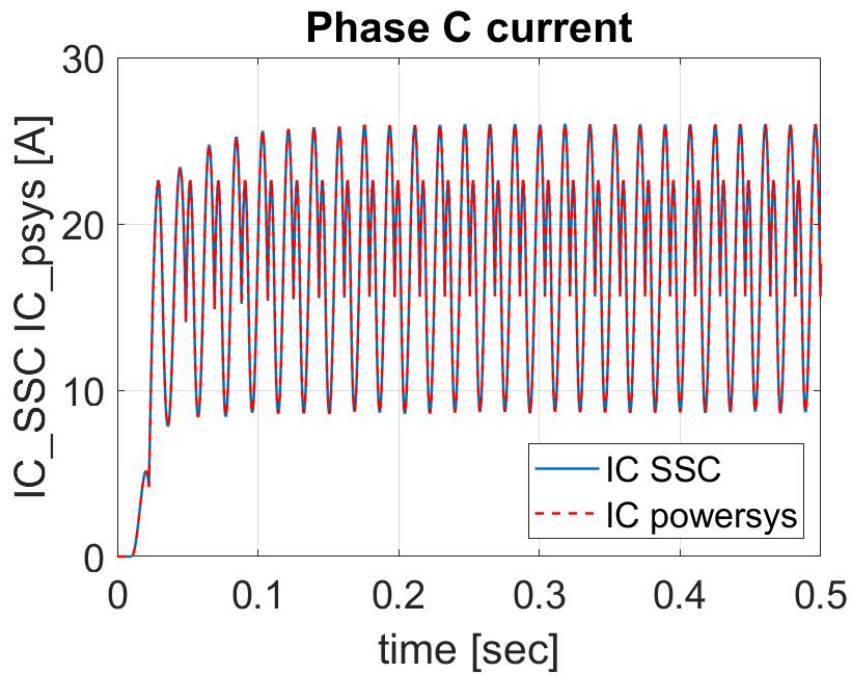


Figure 4.26: I_C

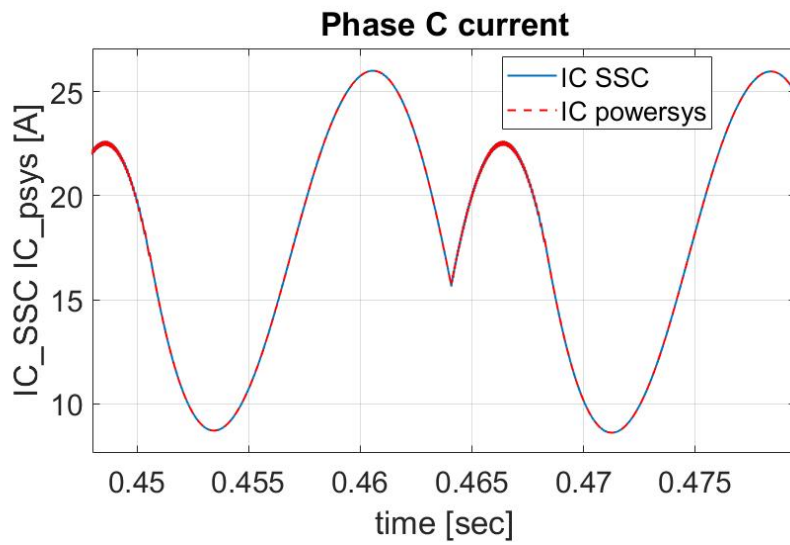


Figure 4.27: I_C at steady state

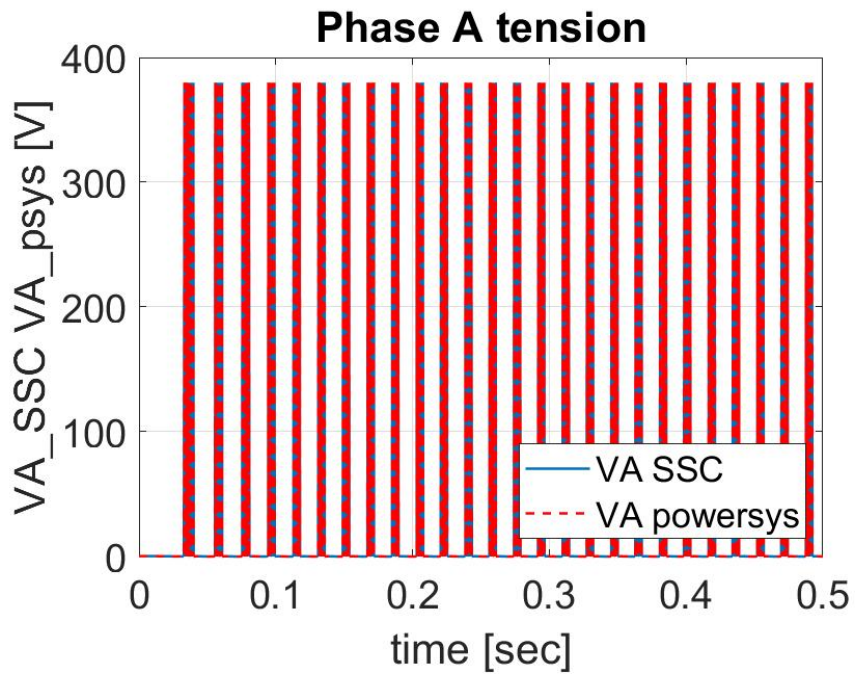


Figure 4.28: V_A

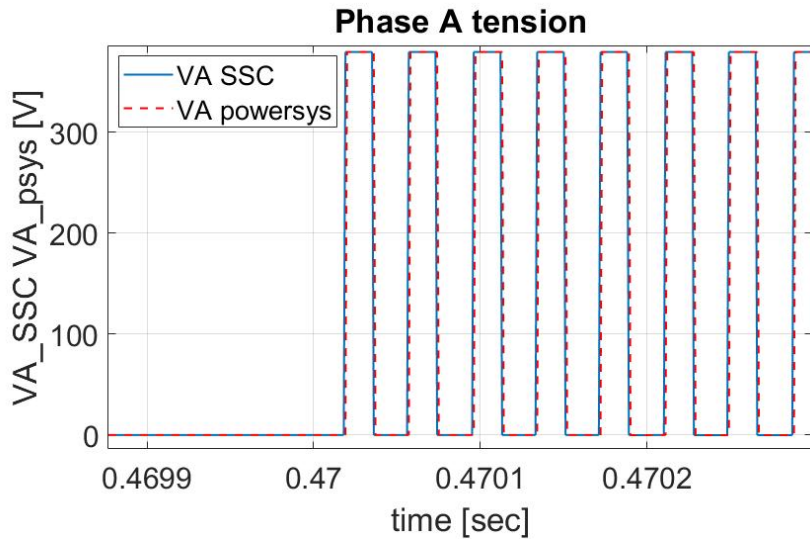


Figure 4.29: V_A at steady state

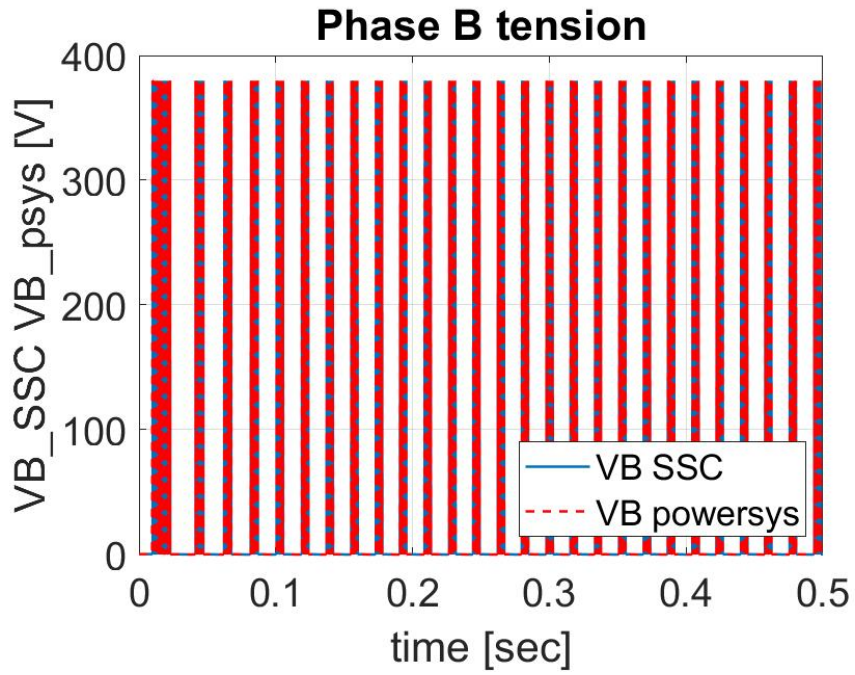


Figure 4.30: V_B

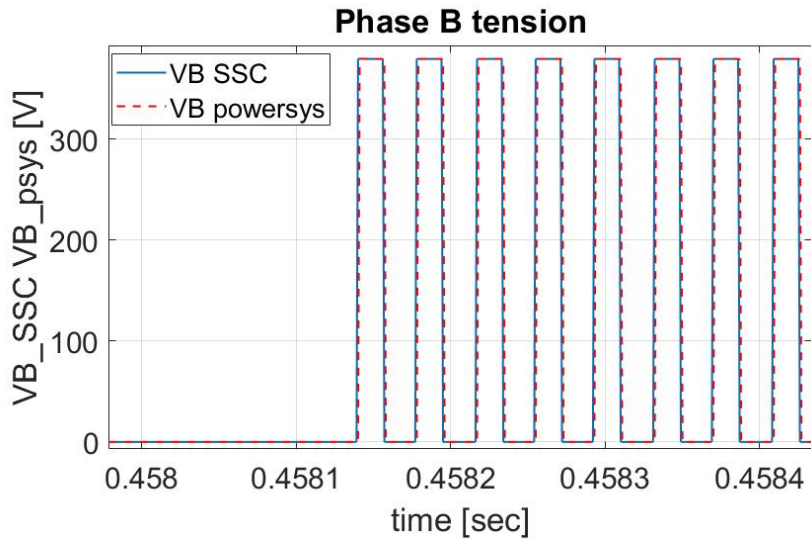


Figure 4.31: V_B at steady state

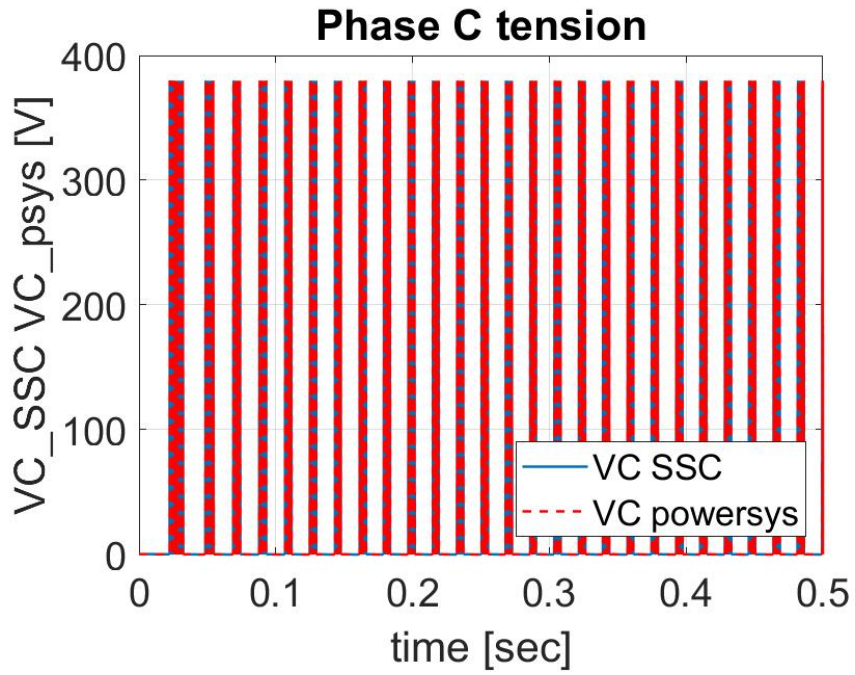


Figure 4.32: V_C

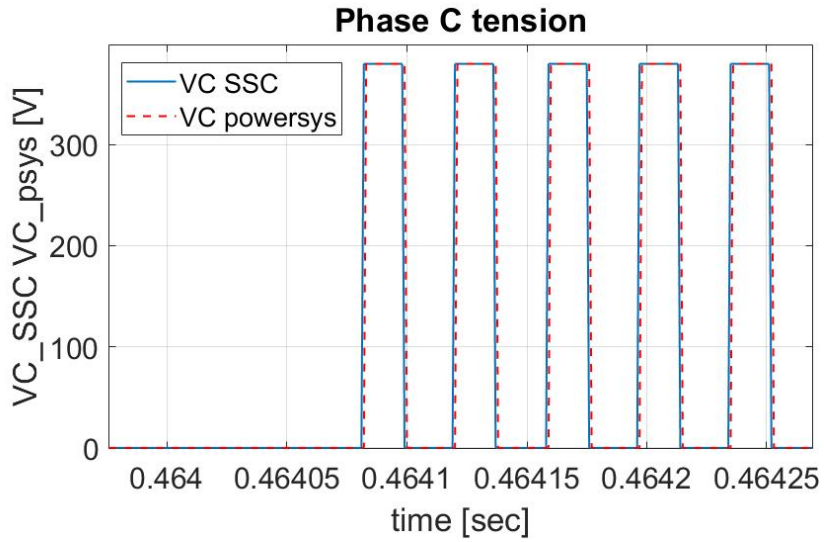


Figure 4.33: V_C at steady state

4.10.2 Ramp command

The simulation parameters are reported in the table 4.2.

Initial output	Slope	Instant of application	External load	Simulation time
0 rad	0.3 rad/sec	0 sec	0 Nm	0.5 sec

Table 4.2: Data ramp command

The figures 4.34, 4.35 and 4.36 show respectively the trend of angular position and angular speed of the motor and angular position of the user.

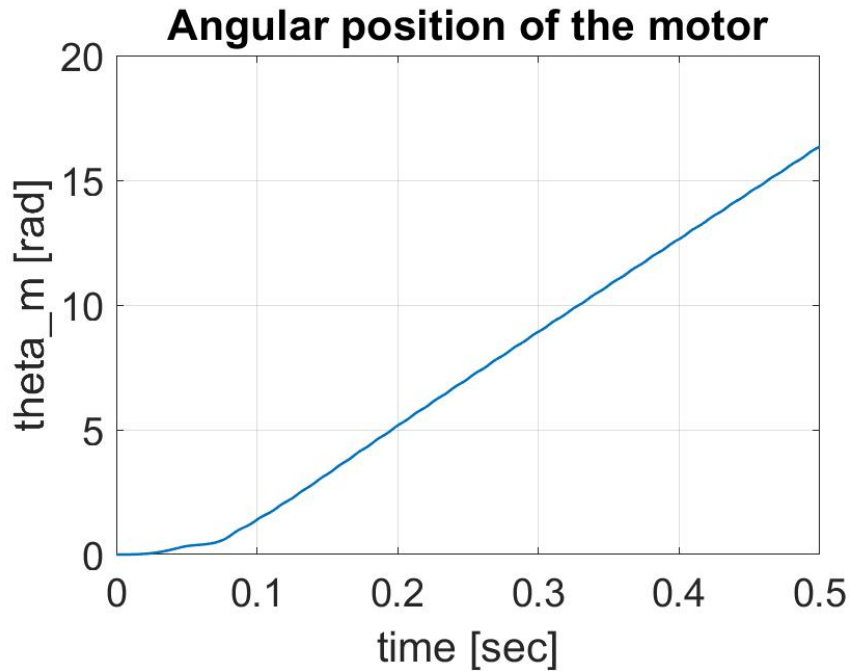


Figure 4.34: Angular position of the motor

The figures 4.37 and 4.38 show respectively the phase A current and tension at steady state to highlight the overlapping of the curves.

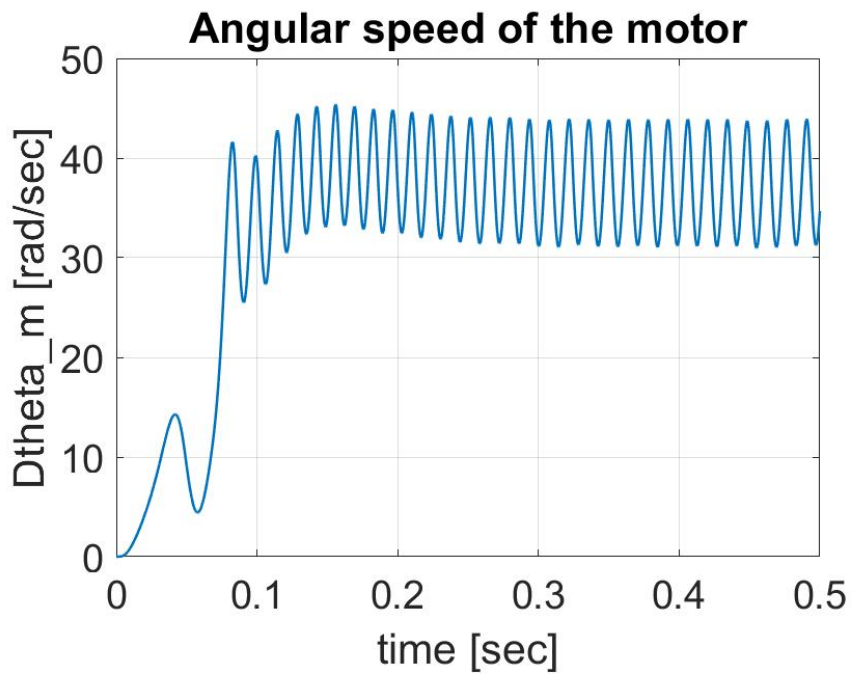


Figure 4.35: Angular speed of the motor

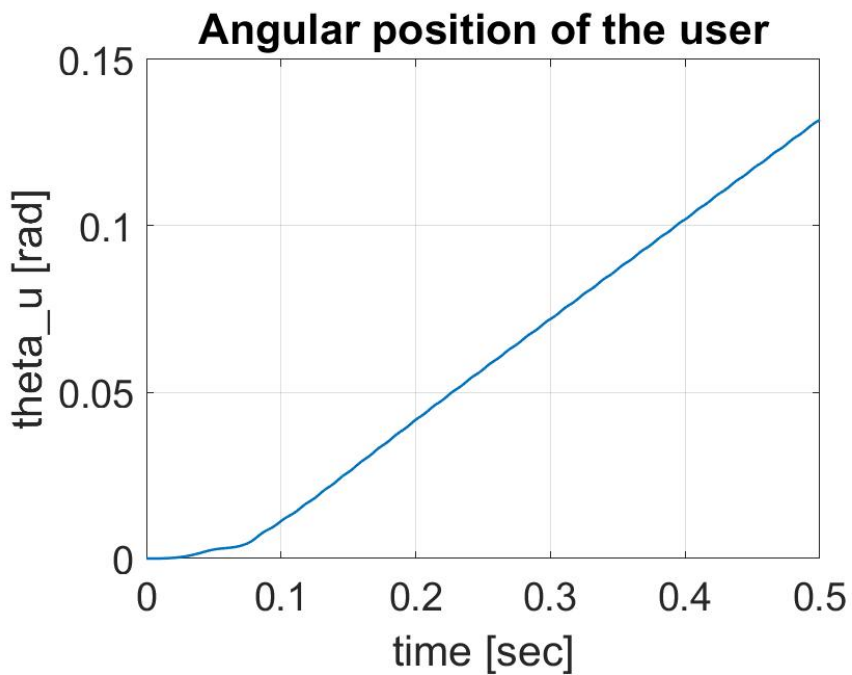


Figure 4.36: Angular position of the user

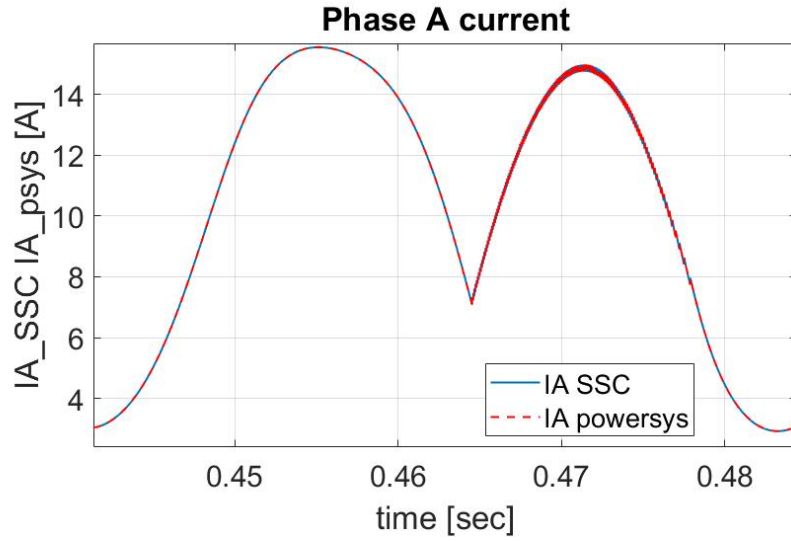


Figure 4.37: I_A at steady state

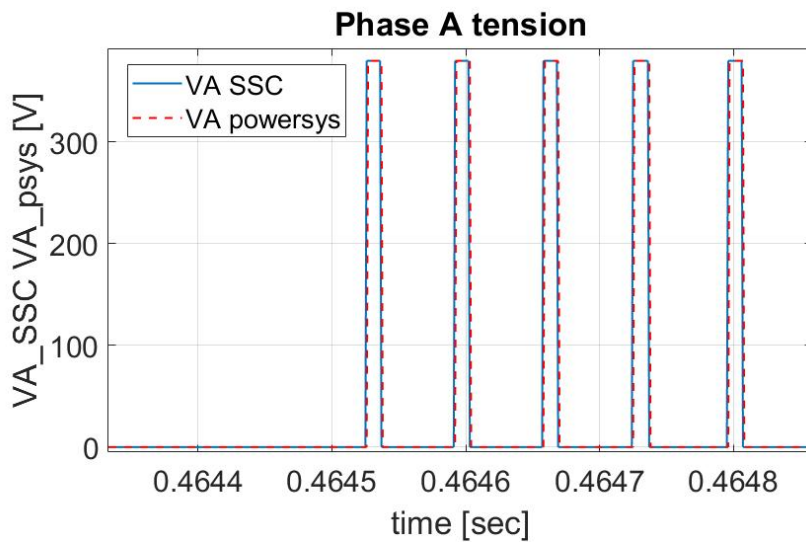


Figure 4.38: V_A at steady state

4.10.3 Sinusoidal command

The simulation parameters are reported in the table 4.3.

Input semiamplitude	Bias input	Input frequency	External load	Simulation time
0.005 rad	0 rad	15 Hz	0 Nm	0.5 sec

Table 4.3: Data sinusoidal command

The figures 4.39, 4.40 and 4.41 show respectively the trend of angular position and angular speed of the motor and angular position of the user.

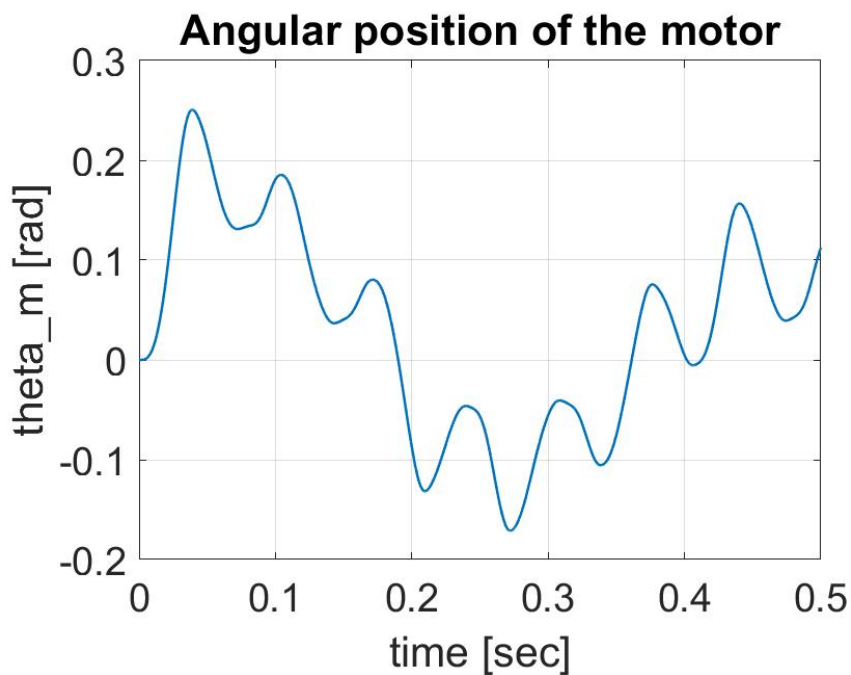


Figure 4.39: Angular position of the motor

The figures 4.42 and 4.43 show respectively the phase A current and tension at steady state to highlight the overlapping of the curves.

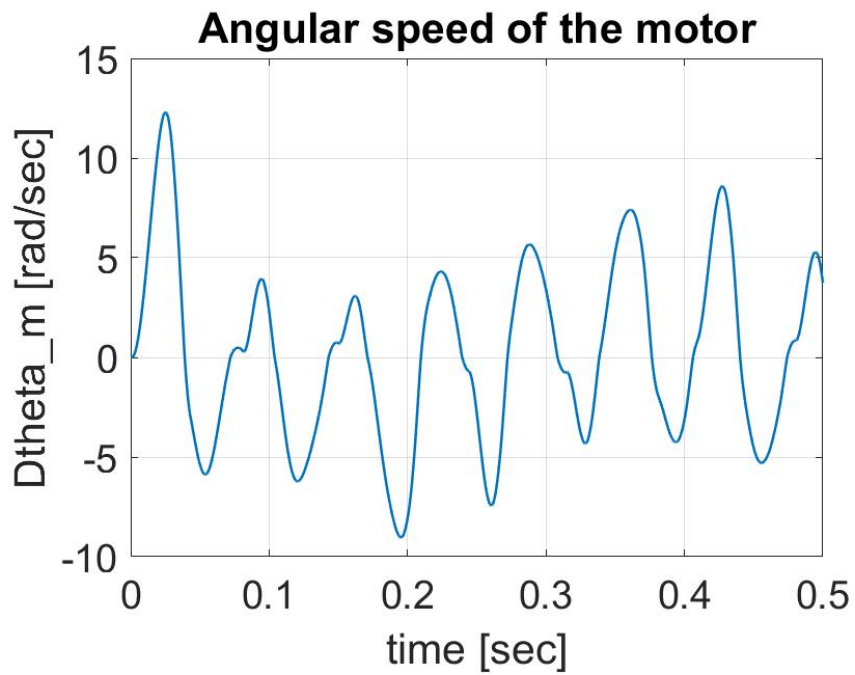


Figure 4.40: Angular speed of the motor

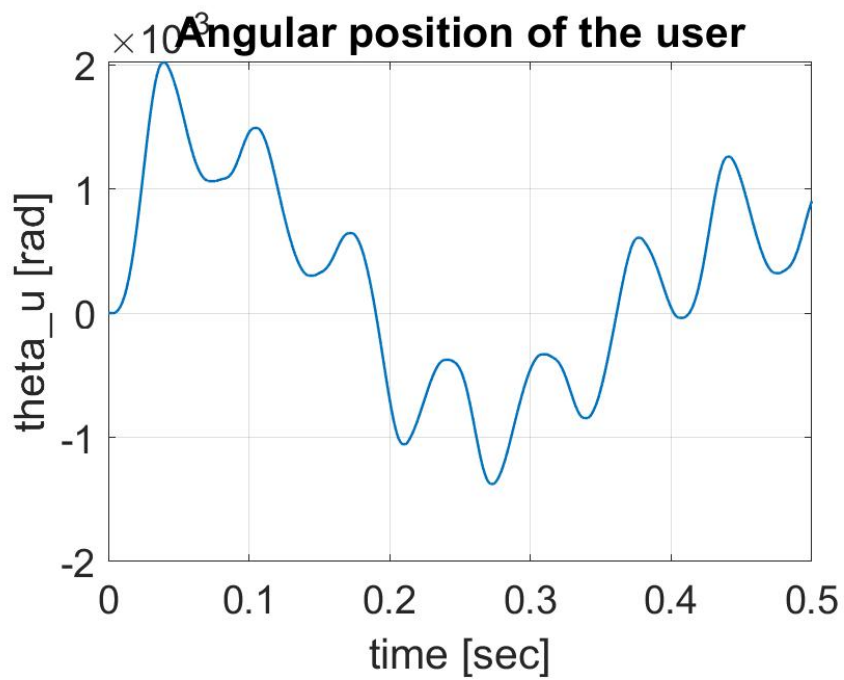


Figure 4.41: Angular position of the user

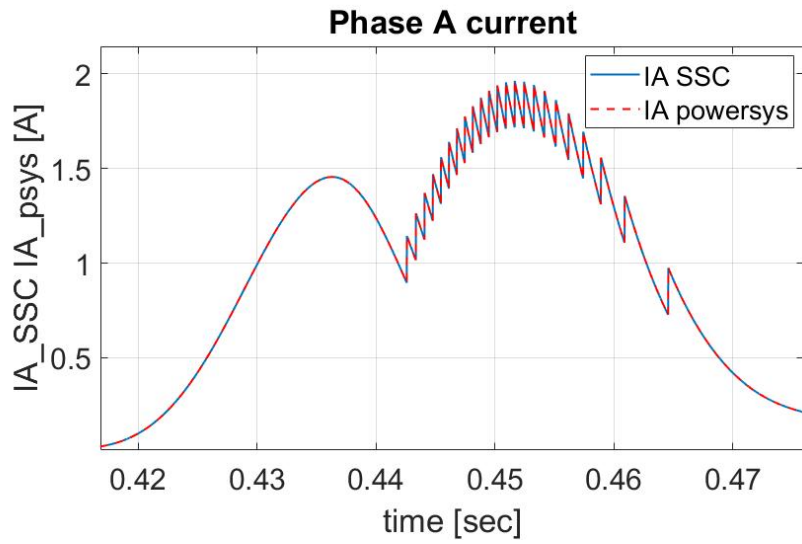


Figure 4.42: I_A at steady state

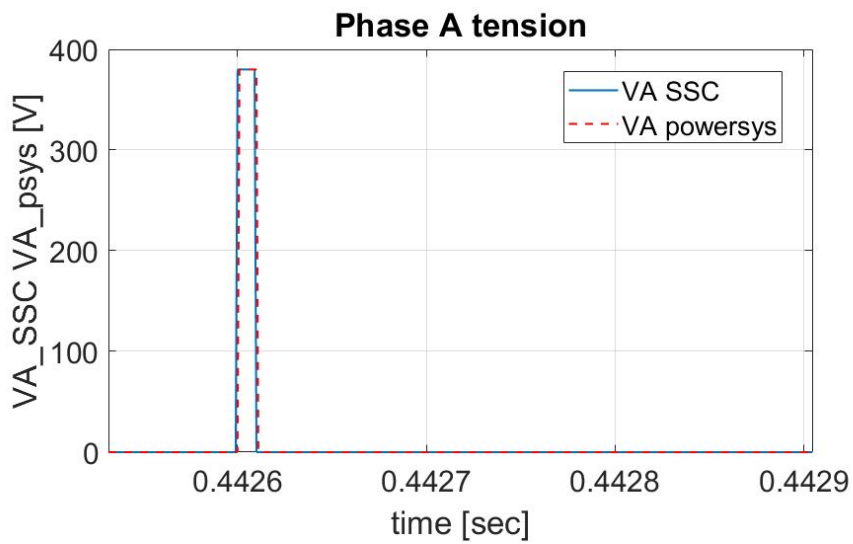


Figure 4.43: V_A at steady state

4.10.4 Step, ramp and external load

The simulation parameters of two commands are reported in the table 4.4 and graphic representation over time is shown in the figure 4.44.

Step command			Ramp command	
t=0 sec	t=0.05 sec	t=0.2 sec	t=0.2 sec	t=0.5 sec
0 rad	0 rad - 0.1 rad	0.1 rad - 0 rad	0 rad	0.1 rad

Table 4.4: Characteristics of two commands

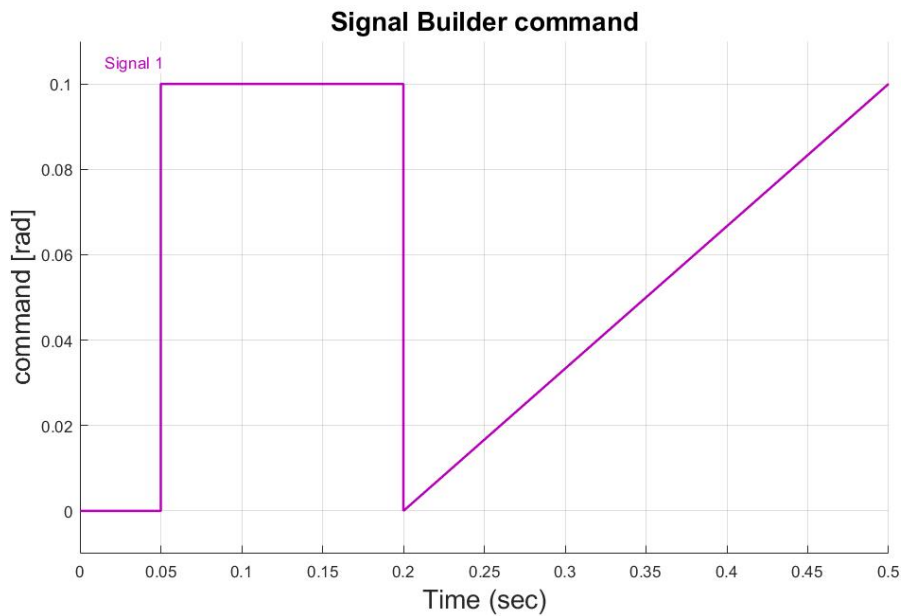


Figure 4.44: Signal builder command

The simulation parameters of external load are reported in the table 4.5 and the graphic representation over time is shown in the figure 4.45.

The figures 4.46, 4.47 and 4.48 show respectively the trend of angular position and angular speed of the motor and angular position of the user.

From the figure 4.47, it can be seen that the angular speed of the motor is reduced because at 0.35 sec an external load is applied which acts in the opposite direction to the direction of rotation of the motor and therefore acts as a brake. The reduction in speed produces a change in the slope of the curve on the angular position of the motor and consequently the user will also be slowed down.

The figures 4.49 and 4.50 show respectively the phase A current and tension at

External load		
t=0 sec	t=0.35 sec	t=0.5 sec
0 Nm	0-150 Nm	150 Nm

Table 4.5: Characteristics of the external load



Figure 4.45: Signal builder load

steady state to highlight the overlapping of the curves.

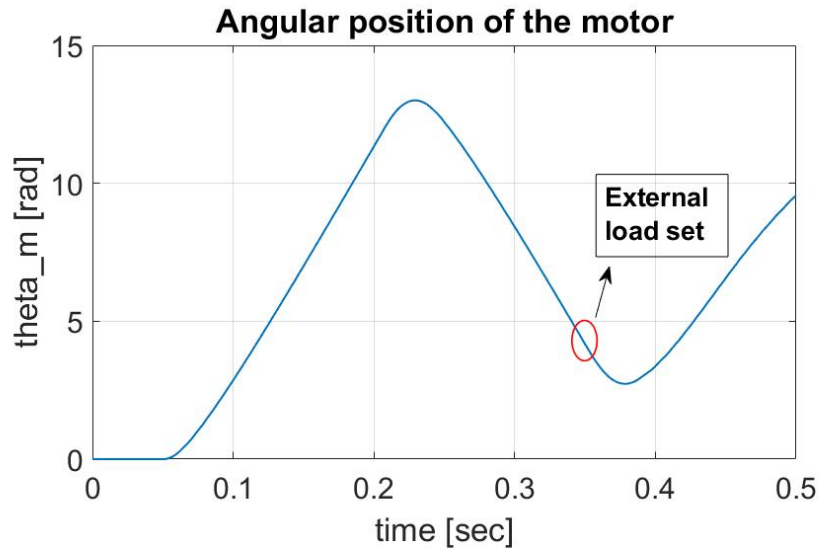


Figure 4.46: Angular position of the motor

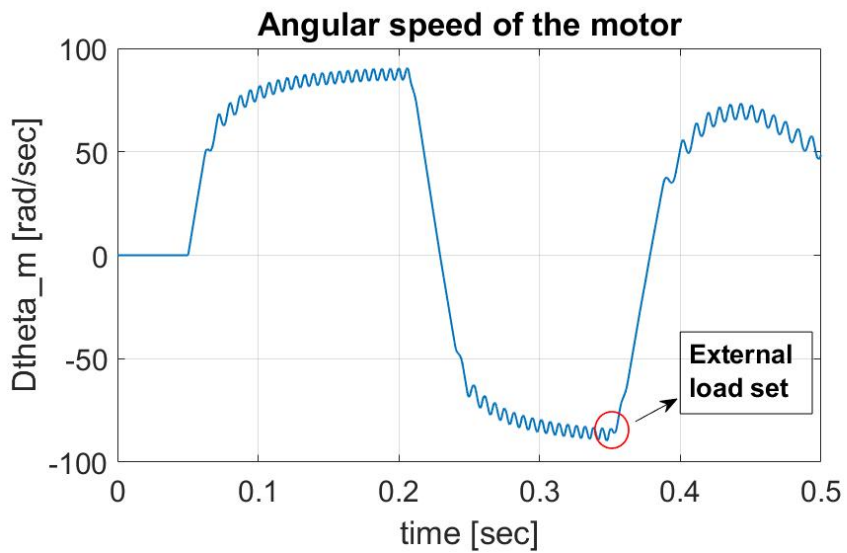


Figure 4.47: Angular speed of the motor

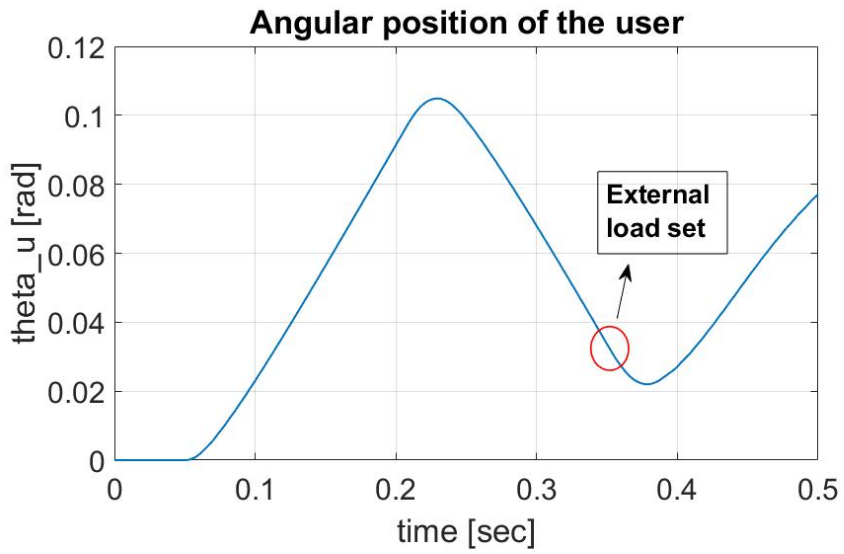


Figure 4.48: Angular position of the user

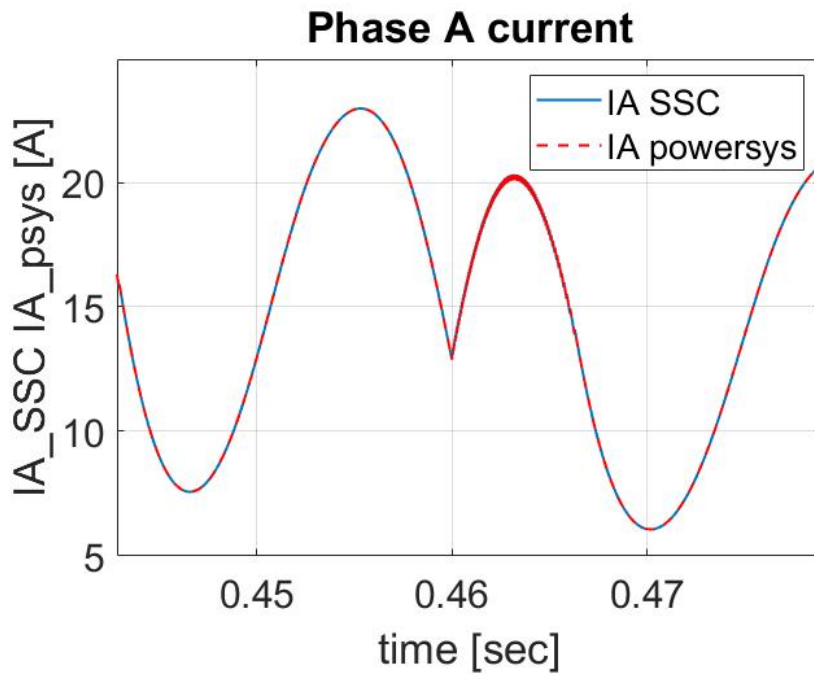


Figure 4.49: I_A at steady state

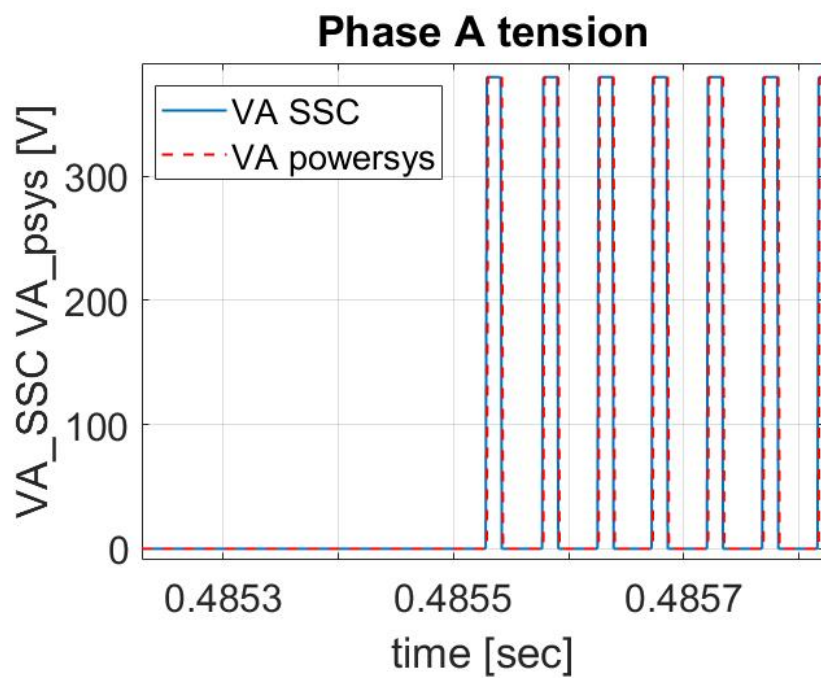


Figure 4.50: V_A at steady state

Chapter 5

Results and conclusions

From an initial graphical analysis of the voltage and current trends of the two models, it can be stated that the curves produced by the Simscape model follow very well the trend of the curves provided by the High-Fidelity model produced in Simulink. To quantify the difference between the values returned by the Simulink model and those returned by the Simscape model, the root mean square error of the voltages and currents was calculated in Matlab. For voltages, the order of magnitude of the root mean square error is around 10^{-5} V and for currents around 10^{-3} A. Therefore, it is possible to state that the two models return exactly the same values for voltages and currents with a tolerance of a few tens of microvolts and a few milliamperes respectively.

Confirmation of the validity of the model produced in Simscape allows future analysis of faults such as a partial short circuit or the percentage of rotor eccentricity to assess their overall effects on the whole system. Therefore, it will be possible to validate the Simscape model even in the presence of faults.

The model produced in Simscape allows the further modelling of the mechanical component of the servomechanism affected by transmission components and non-linear phenomena such as backlash. In addition, it will be possible to perform multi-domain simulations in Simscape considering the interaction of different physical effects allowing, for example, a parallel thermal analysis of the stator windings to prevent potential overheating and demagnetisation of the components with consequent motor loss. These factors offer the possibility of developing highly accurate and effective prognostic algorithms for electromechanical servomechanisms.

Appendix A

Brushless DC motor

A.1 Step command

The figures A.1, A.2 and A.3 show the phase A, B, C current.

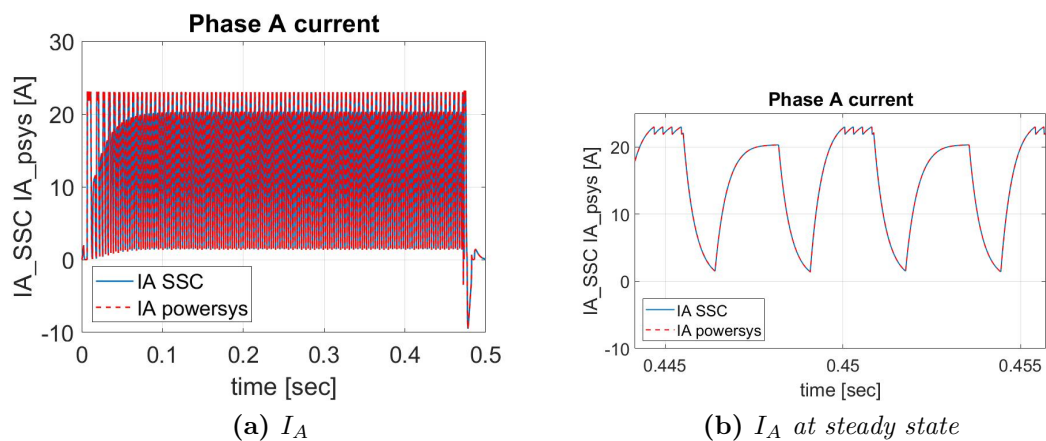


Figure A.1: Phase A current

The figures A.4, A.5 and A.6 show the phase A, B, C tension.

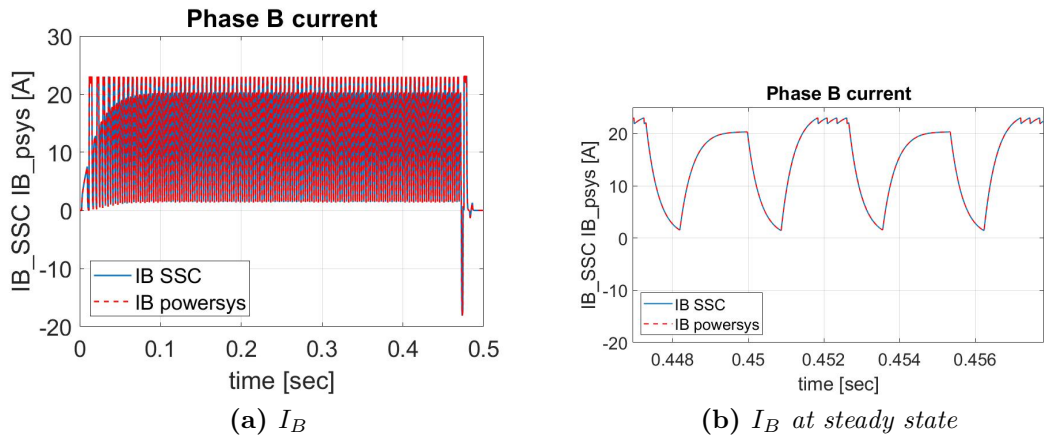


Figure A.2: Phase B current

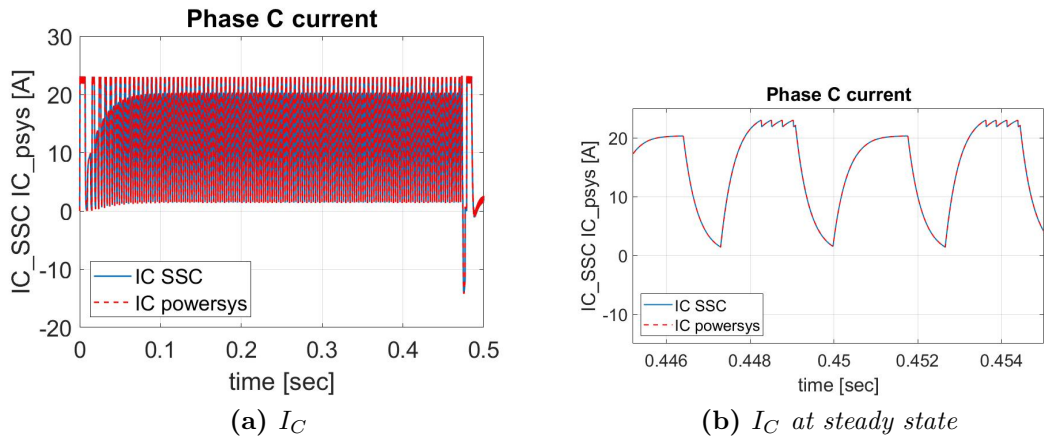


Figure A.3: Phase C current

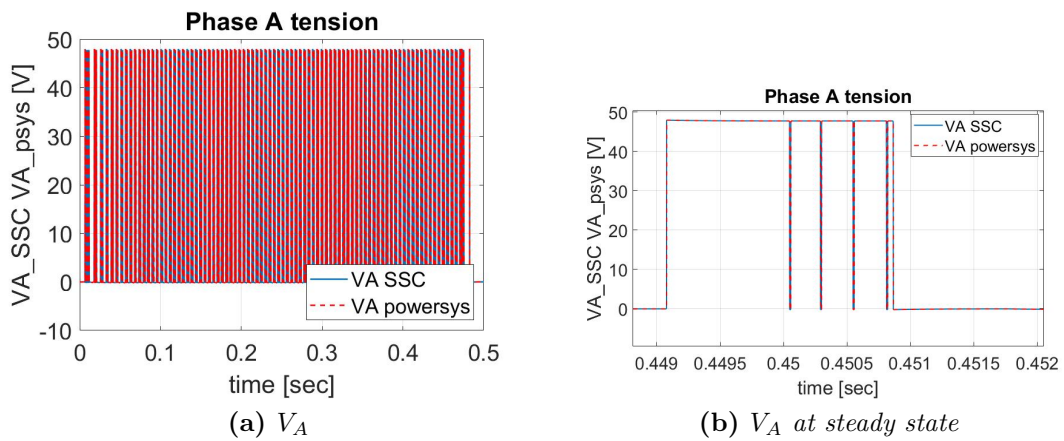


Figure A.4: Phase A tension

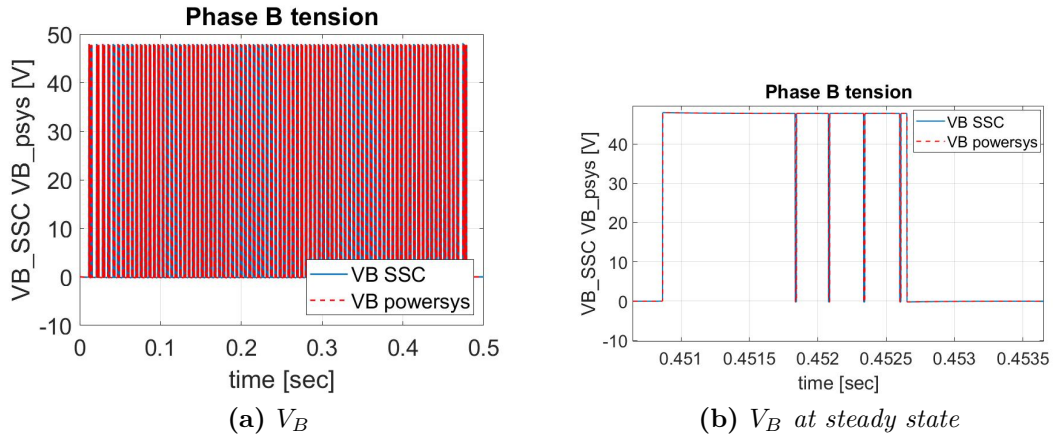


Figure A.5: Phase B tension

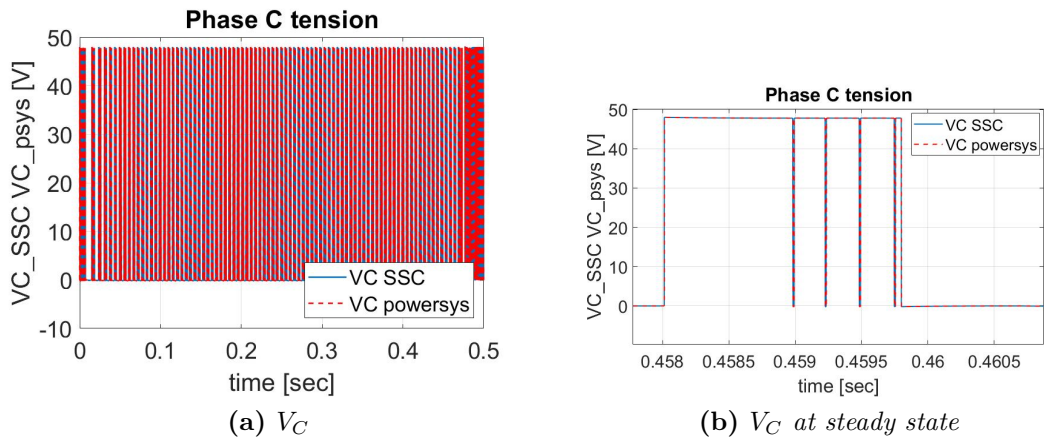


Figure A.6: Phase C tension

A.2 Ramp command

The figures A.7, A.8 and A.9 show the phase A, B, C current.

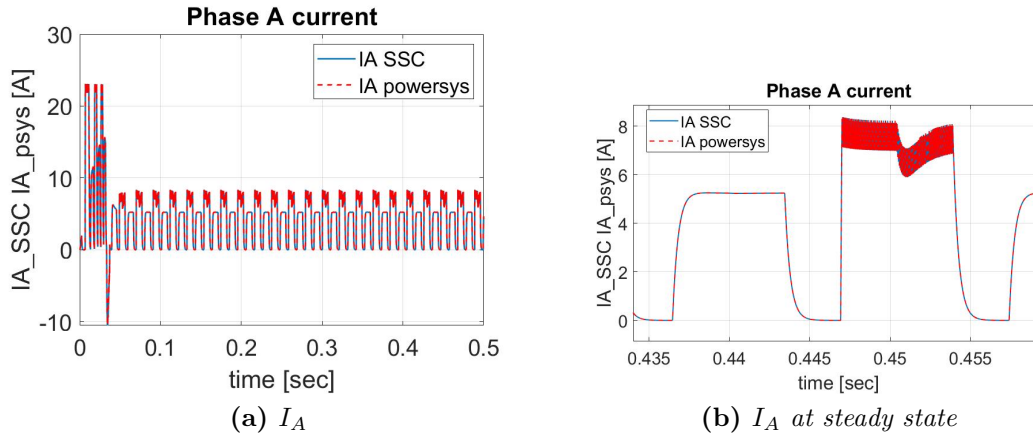


Figure A.7: Phase A current

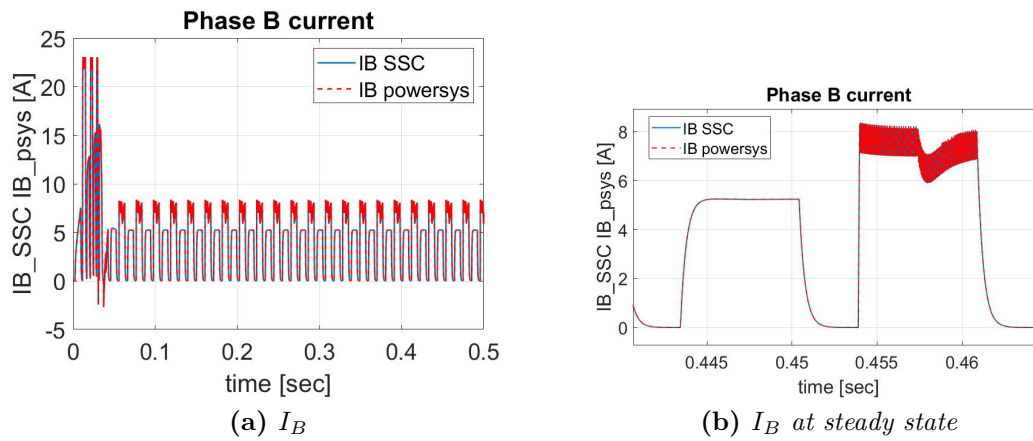


Figure A.8: Phase B current

The figures A.10, A.11 and A.12 show the phase A, B, C tension.

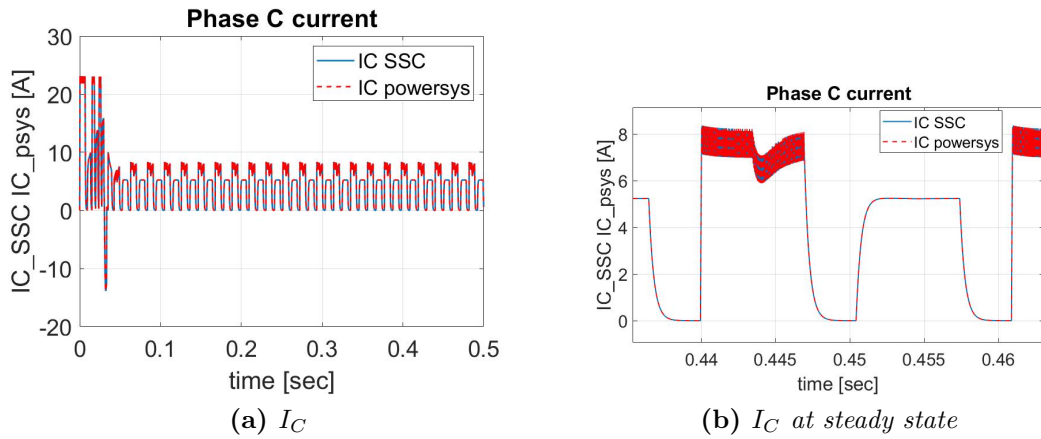


Figure A.9: Phase C current

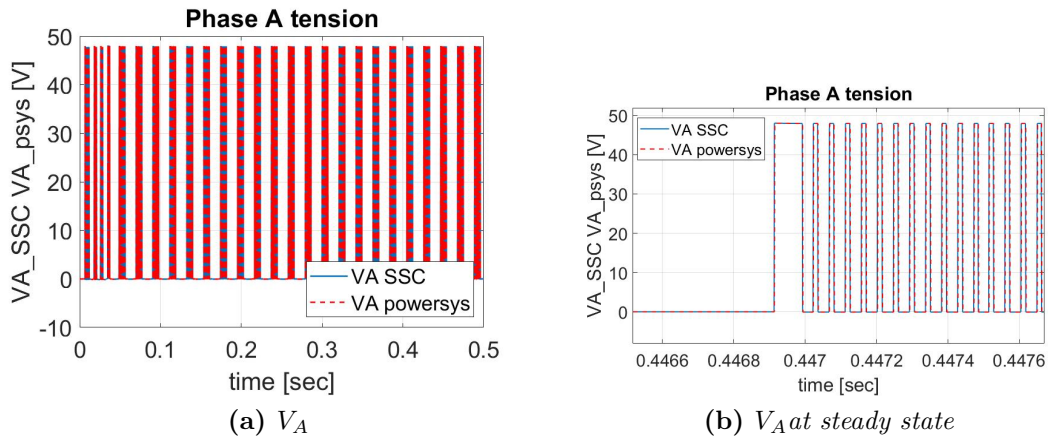


Figure A.10: Phase A tension

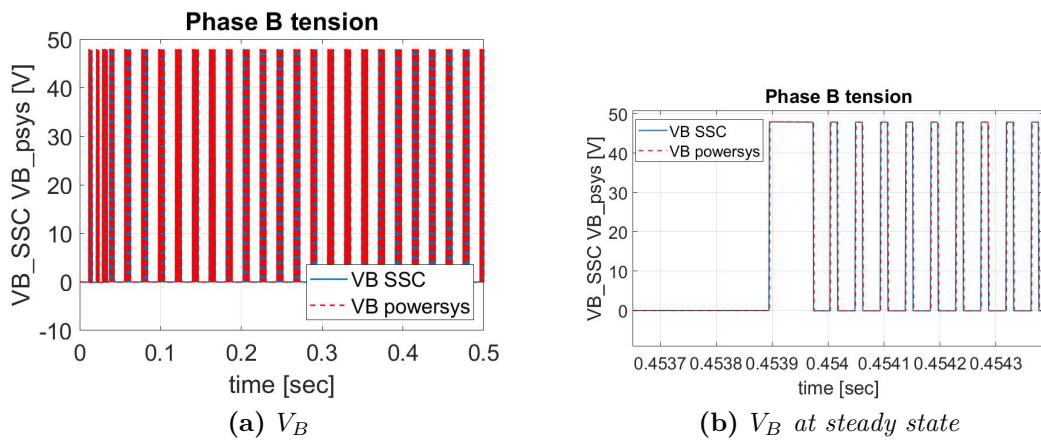


Figure A.11: Phase B tension

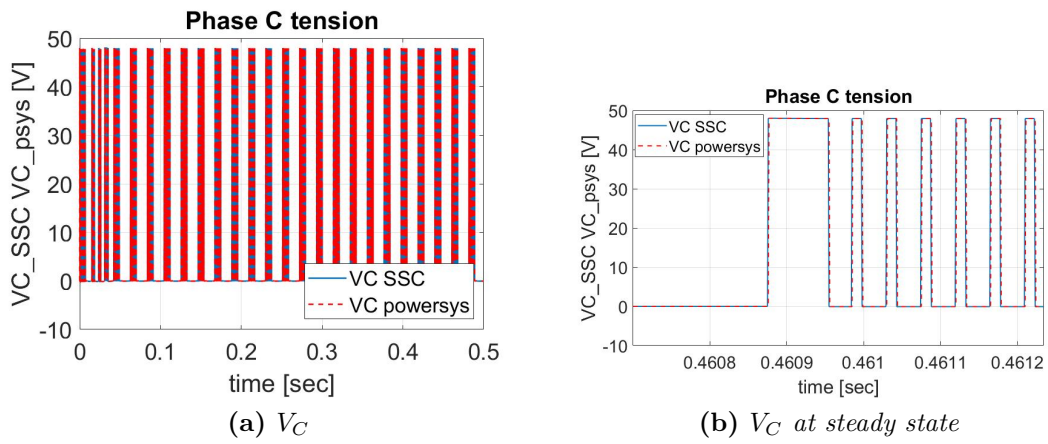


Figure A.12: Phase C tension

A.3 Sinusoidal command

The figures A.13, A.14 and A.15 show the phase A, B, C current.

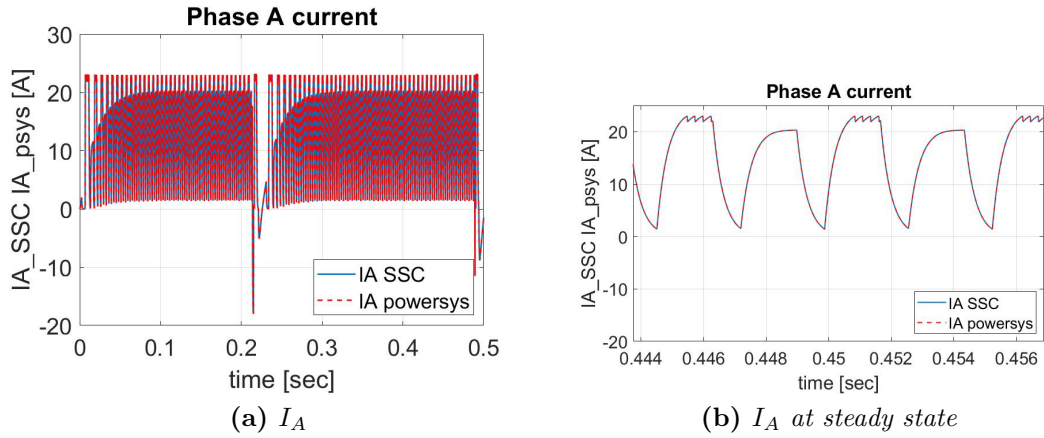


Figure A.13: Phase A current

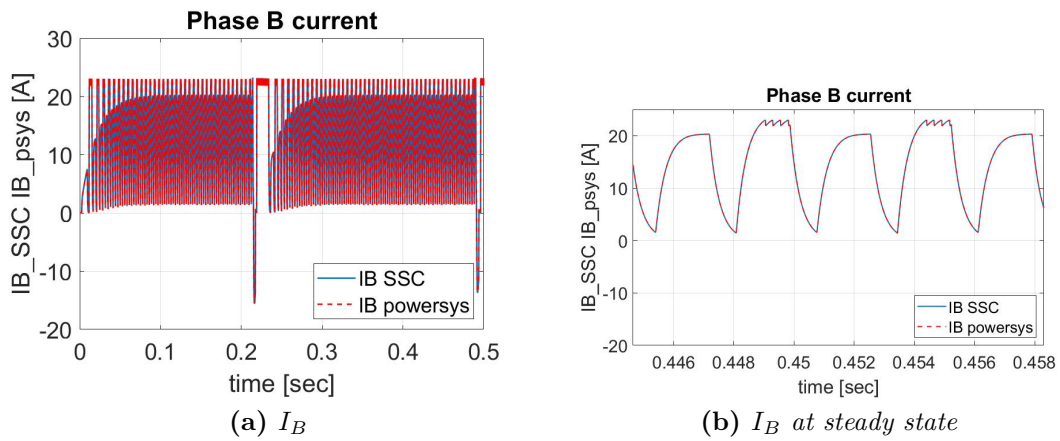


Figure A.14: Phase B current

The figures A.16, A.17 and A.18 show the phase A, B, C tension.

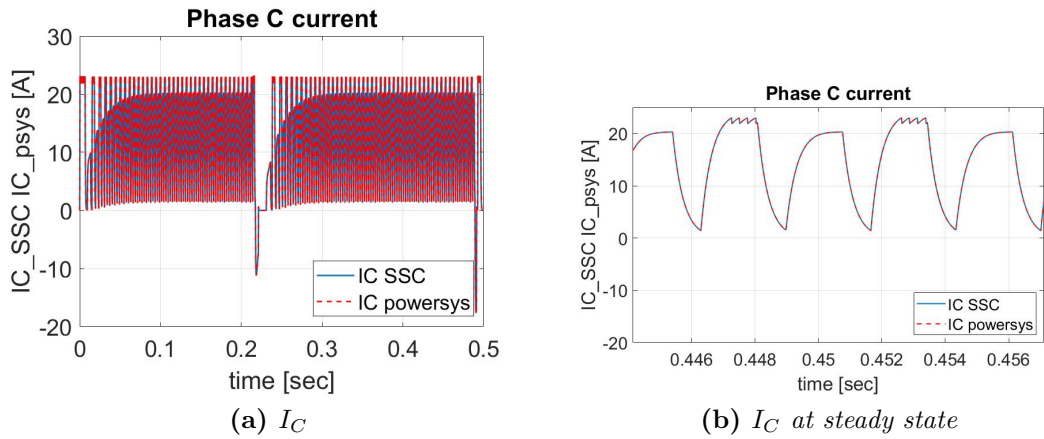


Figure A.15: Phase C current

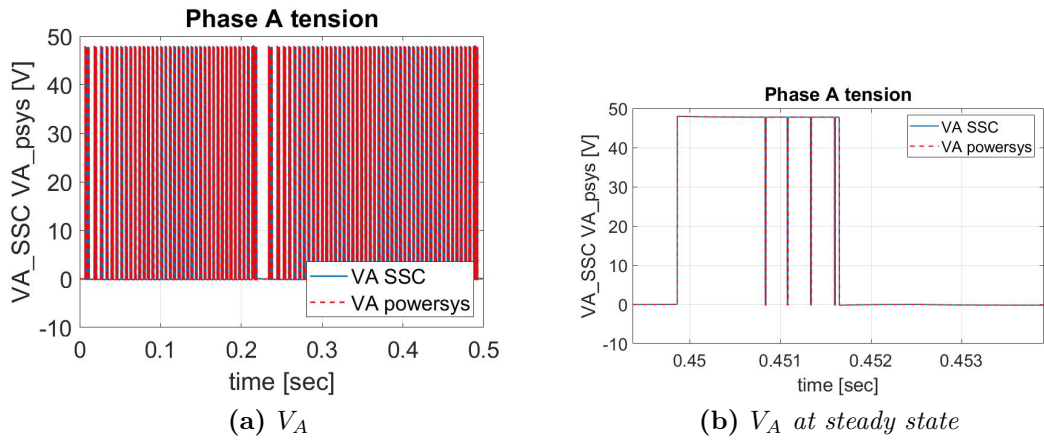


Figure A.16: Phase A tension

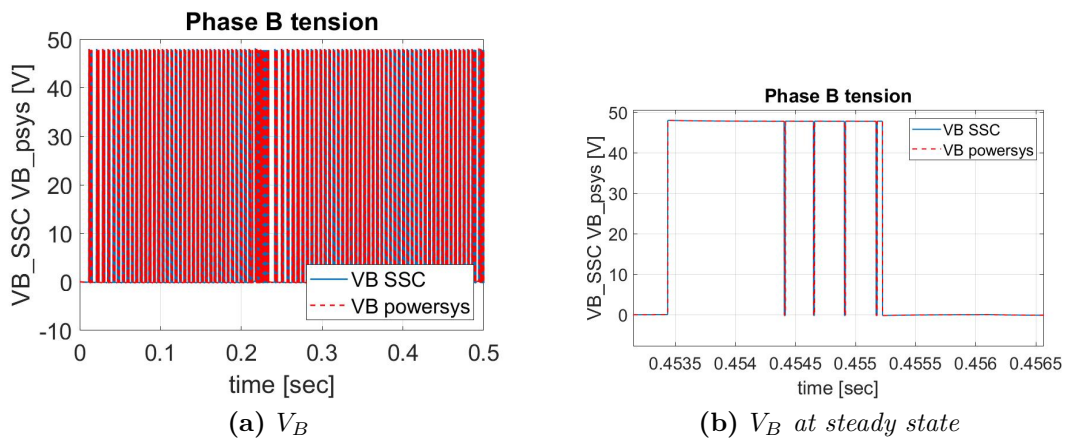


Figure A.17: Phase B tension

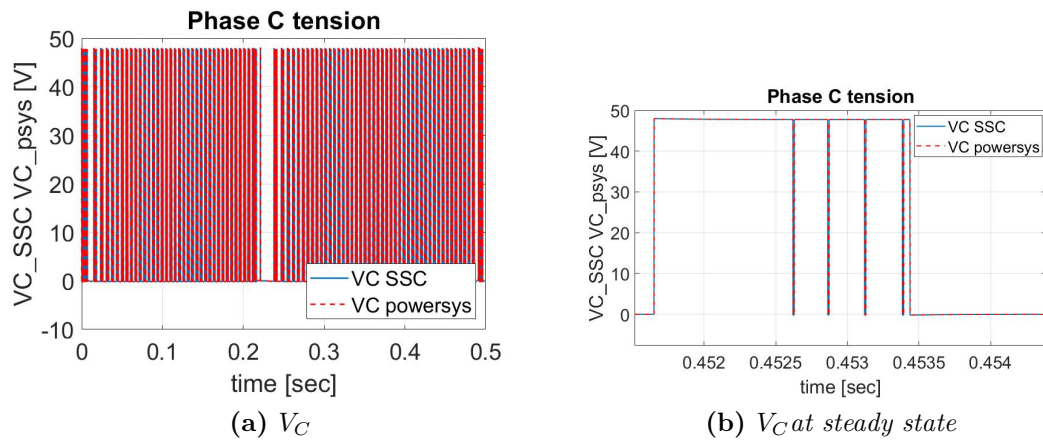


Figure A.18: Phase C tension

A.4 Step, ramp and external load

The figures A.19, A.20 and A.21 show the phase A, B, C current.

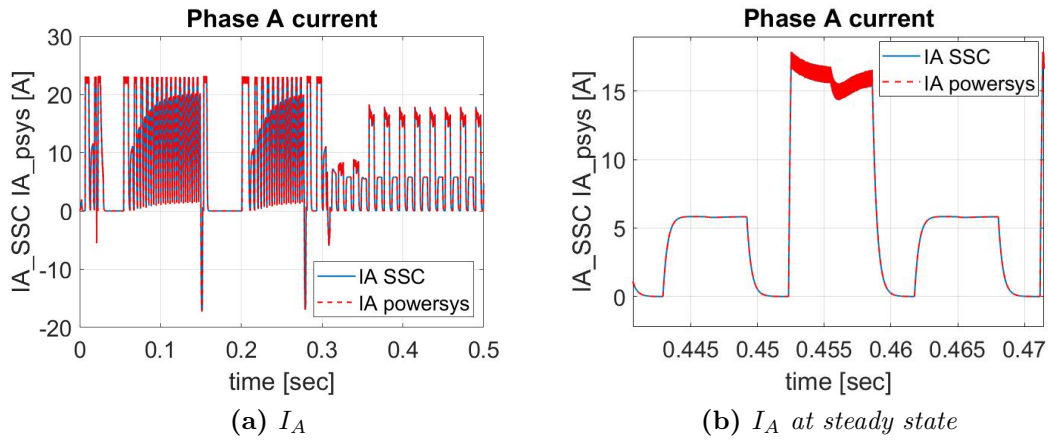


Figure A.19: Phase A current

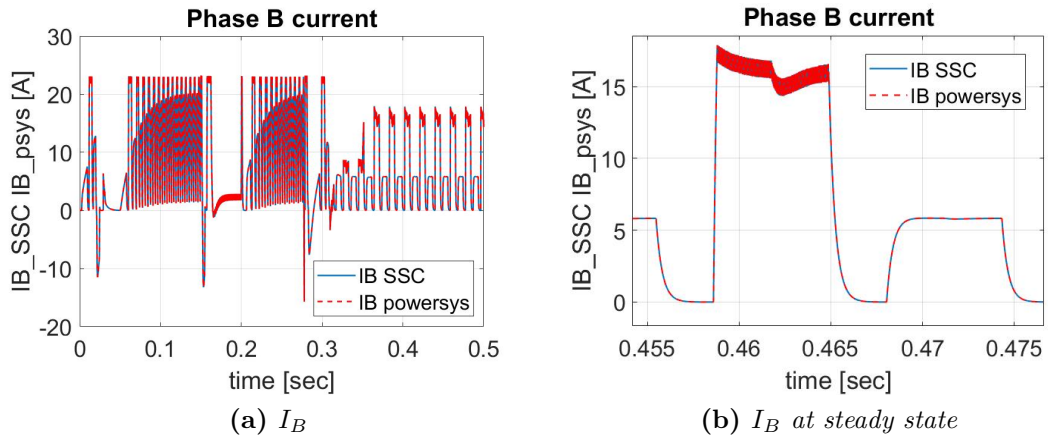


Figure A.20: Phase B current

The figures A.22, A.23 and A.24 show the phase A, B, C tension.

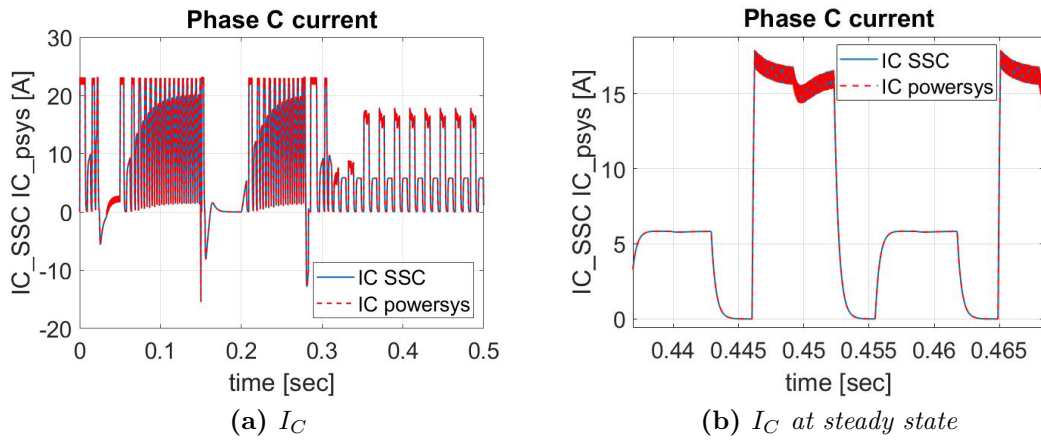


Figure A.21: Phase C current

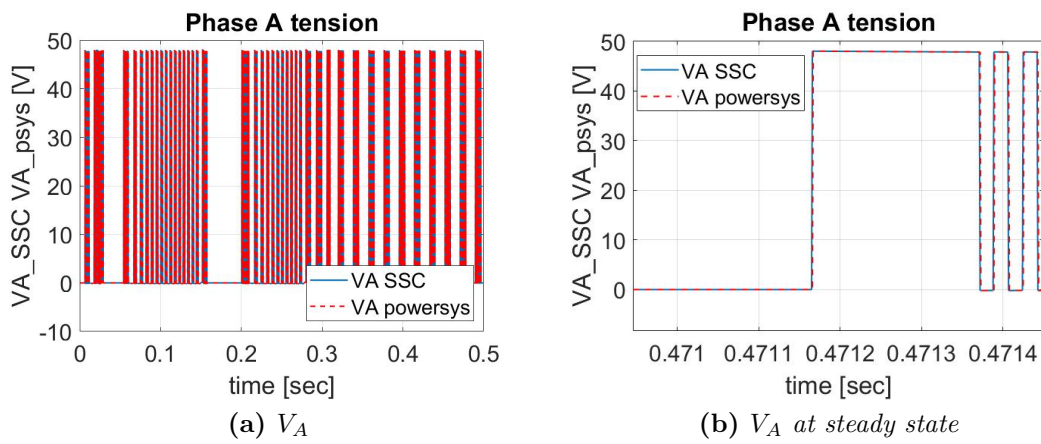


Figure A.22: Phase A tension

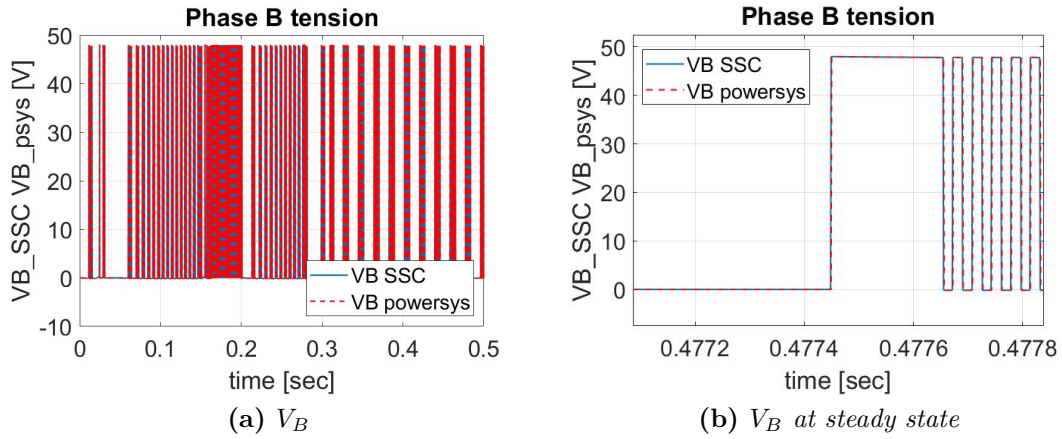


Figure A.23: Phase B tension

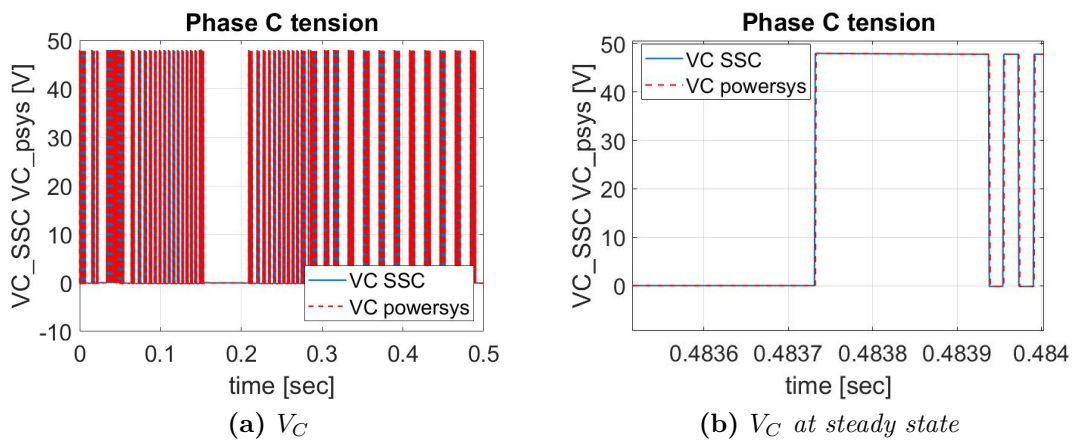


Figure A.24: Phase C tension

Appendix B

PMSM

B.1 Step command

The figures B.1, B.2 and B.3 show the phase A, B, C current.

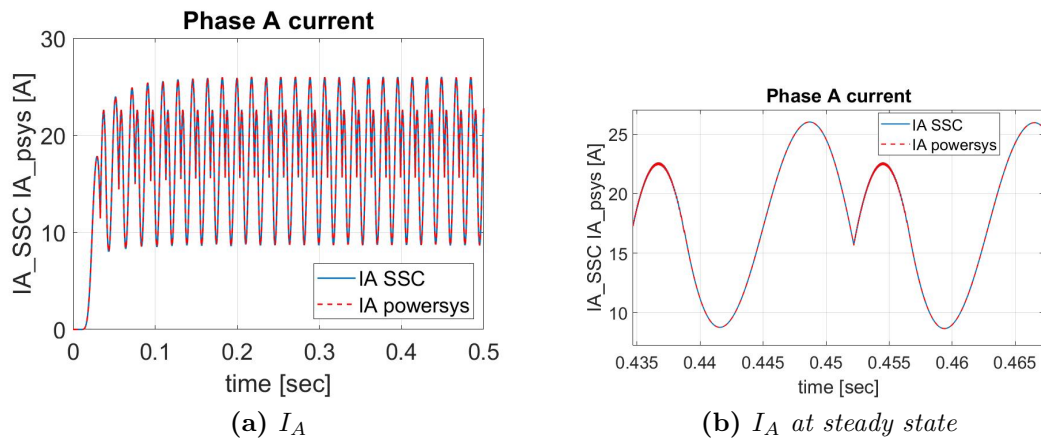


Figure B.1: Phase A current

The figures B.4, B.5 and B.6 show the phase A, B, C tension.

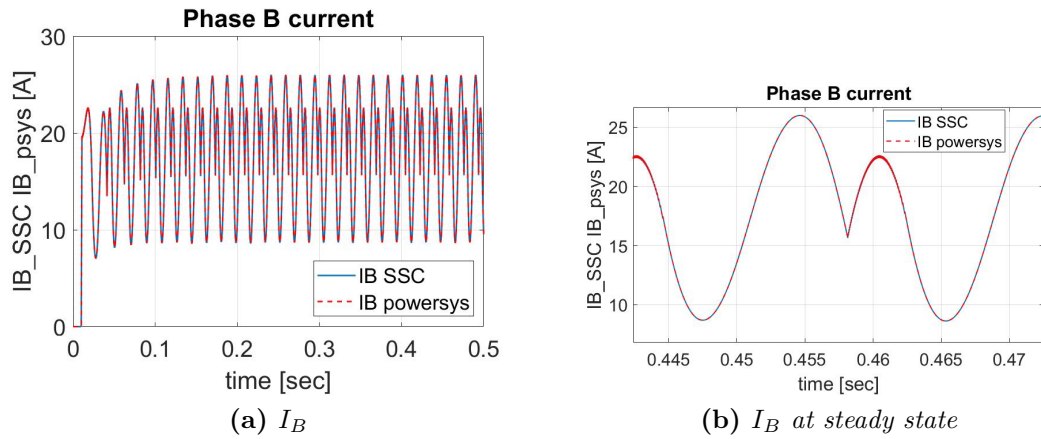


Figure B.2: Phase B current

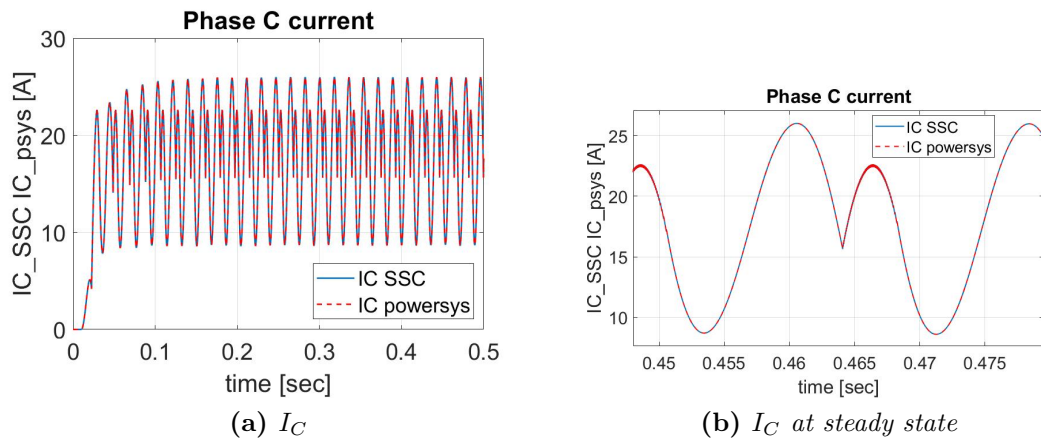


Figure B.3: Phase C current

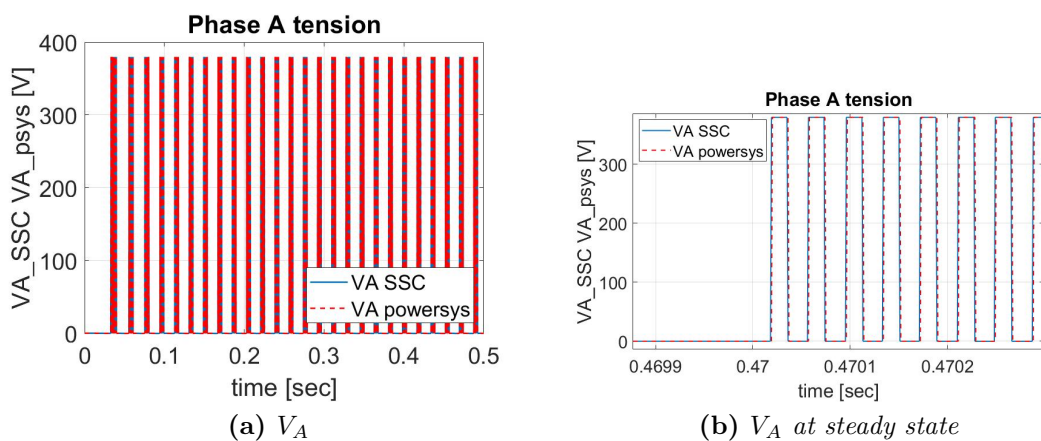


Figure B.4: Phase A tension

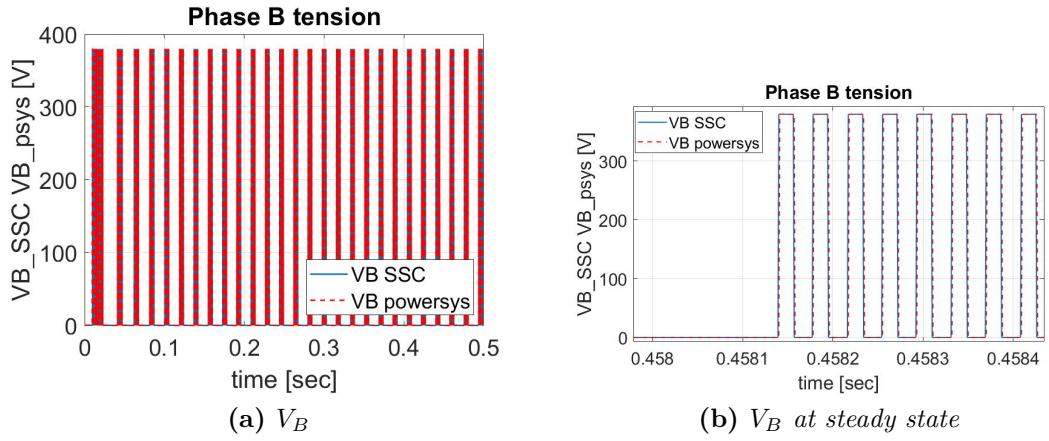


Figure B.5: Phase B tension

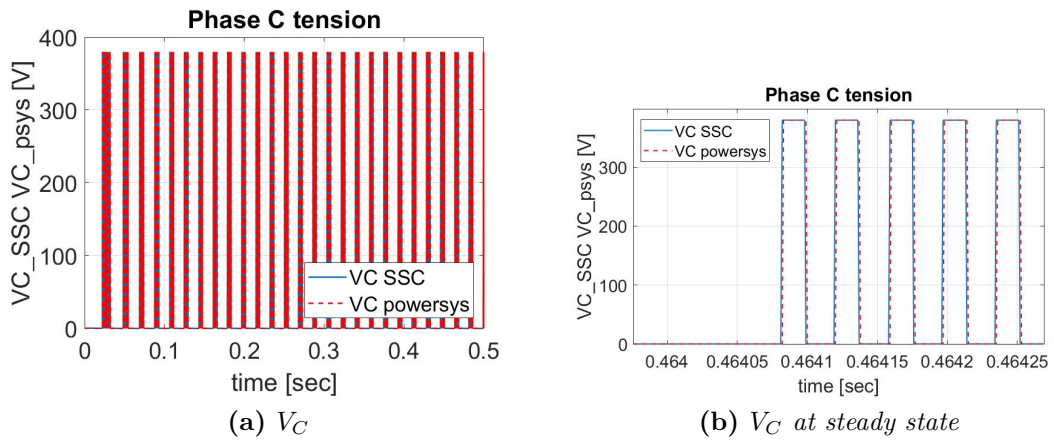


Figure B.6: Phase C tension

B.2 Ramp command

The figures B.7, B.8 and B.9 show the phase A, B, C current.

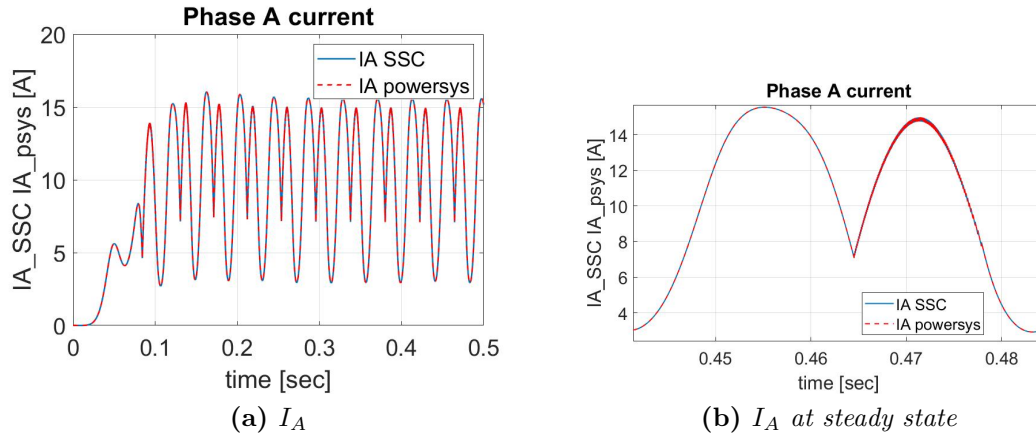


Figure B.7: Phase A current

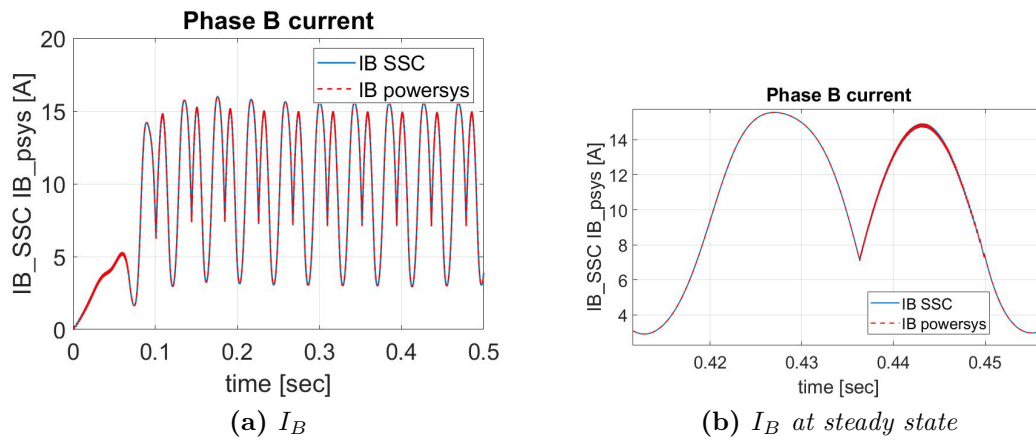


Figure B.8: Phase B current

The figures B.10, B.11 and B.12 show the phase A, B, C tension.

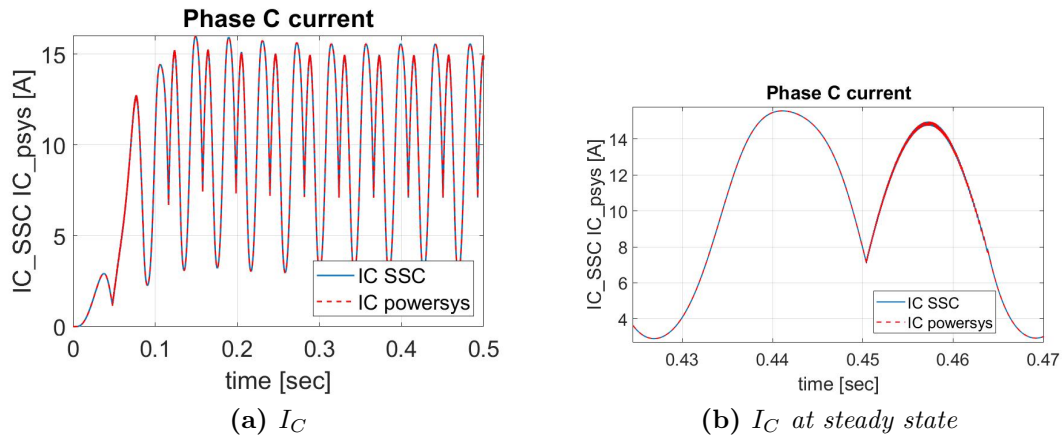


Figure B.9: Phase C current

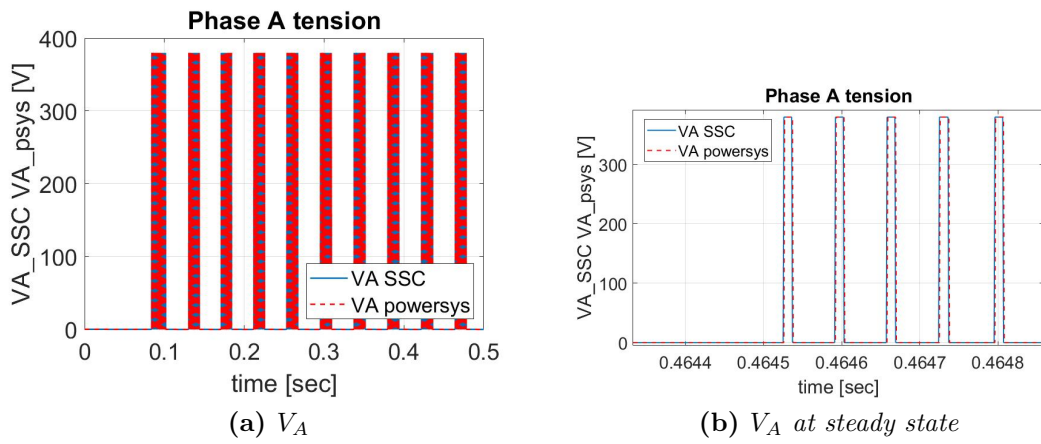


Figure B.10: Phase A tension

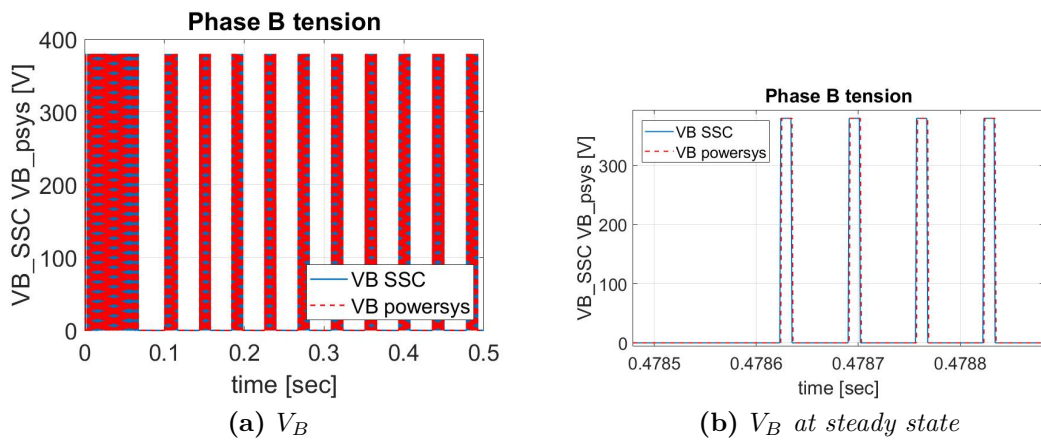


Figure B.11: Phase B tension

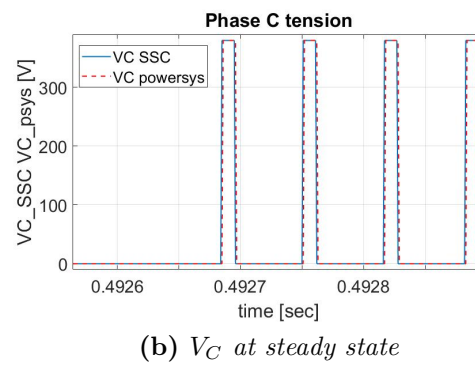
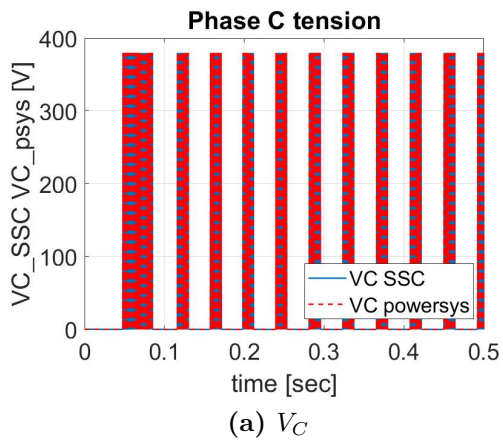


Figure B.12: Phase C tension

B.3 Sinusoidal command

The figures B.13, B.14 and B.15 show the phase A, B, C current.

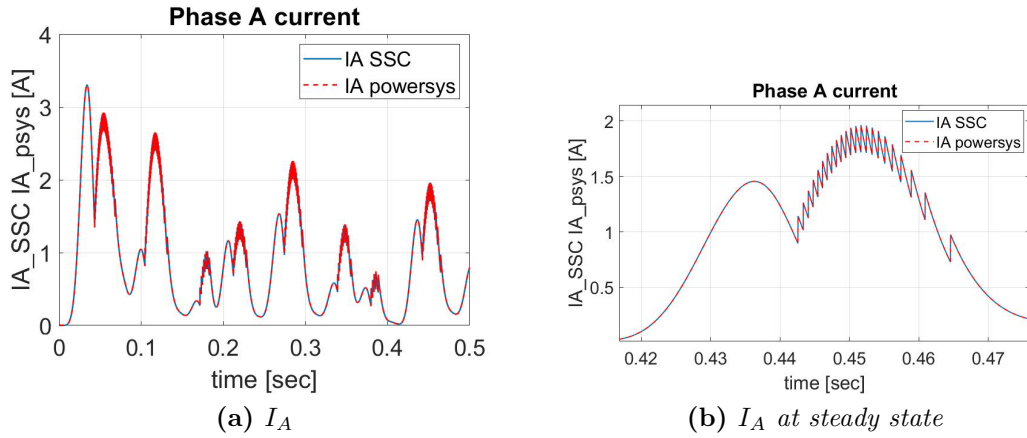


Figure B.13: Phase A current

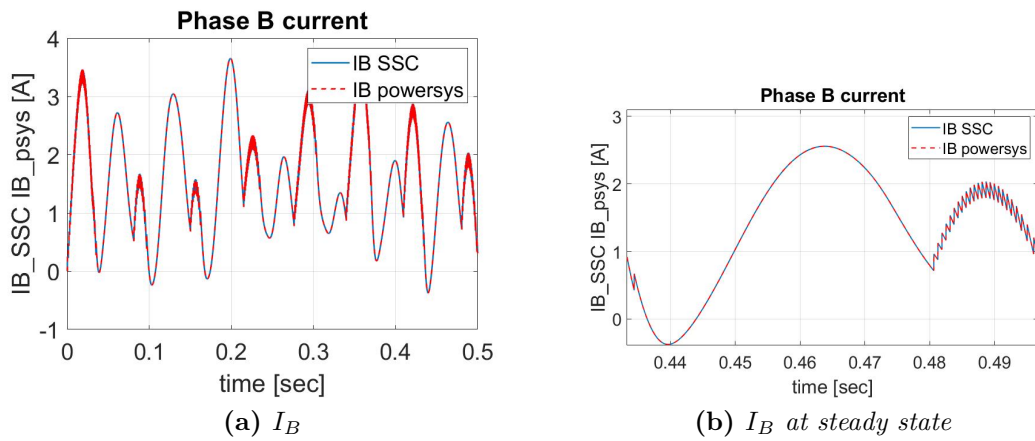


Figure B.14: Phase B current

The figures B.16, B.17 and B.18 show the phase A, B, C tension.

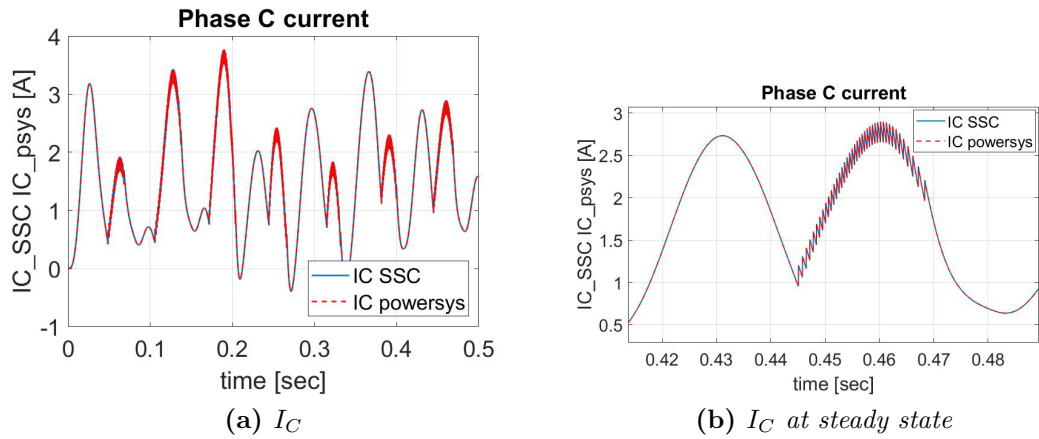


Figure B.15: Phase C current

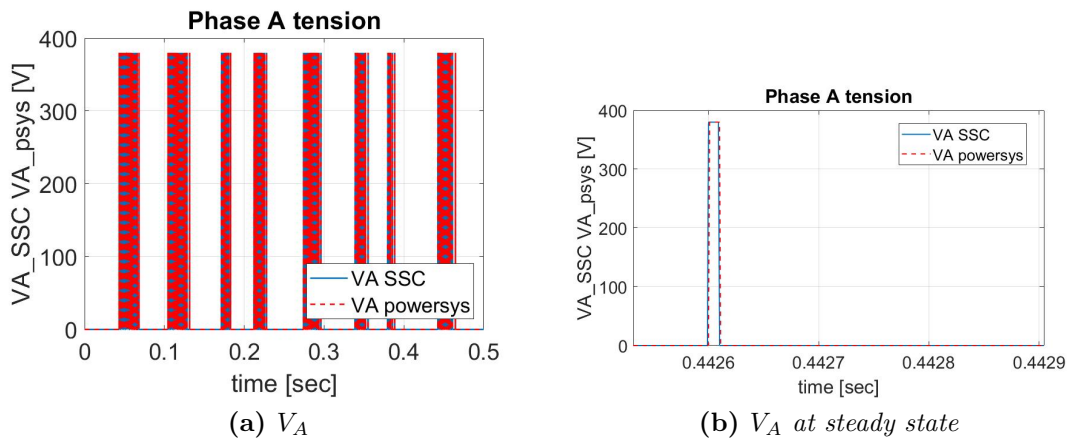


Figure B.16: Phase A tension

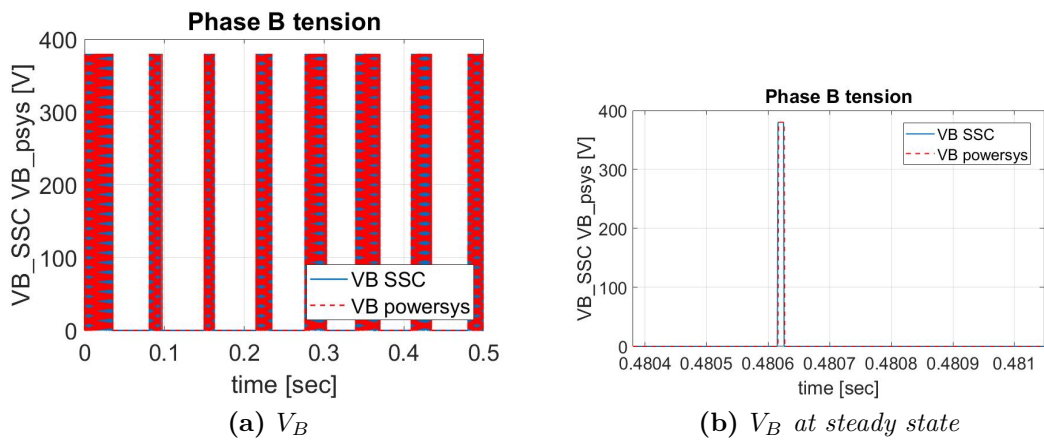
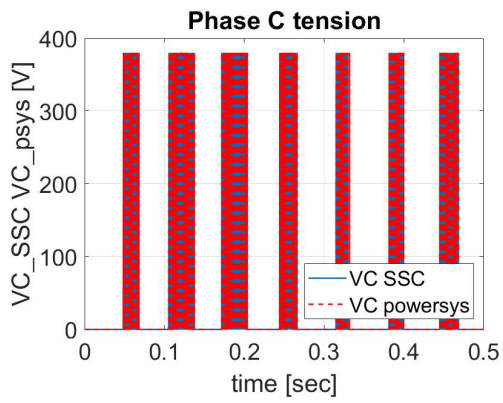
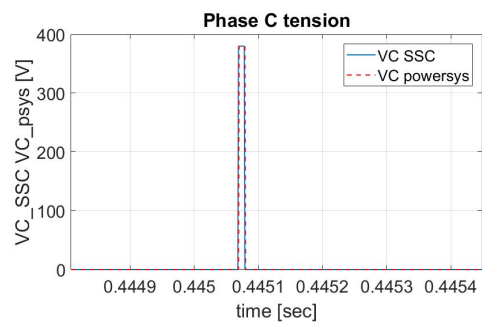


Figure B.17: Phase B tension



(a) V_C



(b) V_C at steady state

Figure B.18: Phase C tension

B.4 Step, ramp and external load

The figures B.19, B.20 and B.21 show the phase A, B, C current.

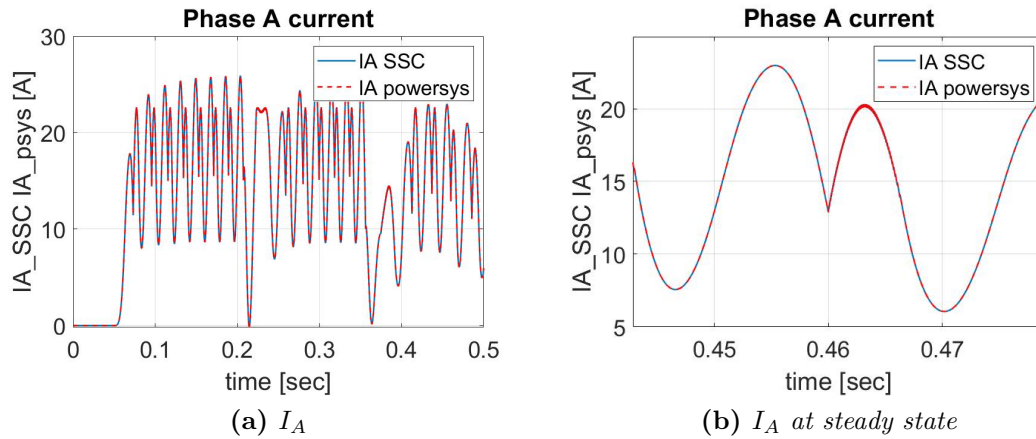


Figure B.19: Phase A current

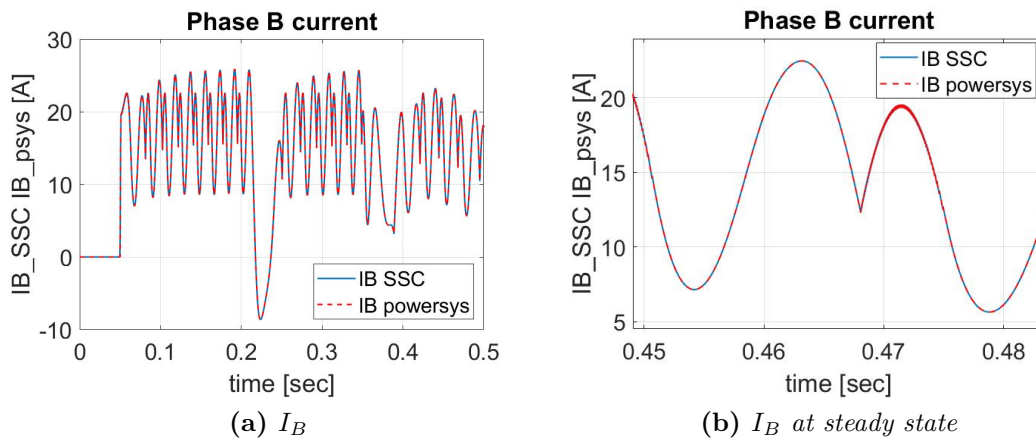


Figure B.20: Phase B current

The figures B.22, B.23 and B.24 show the phase A, B, C tension.

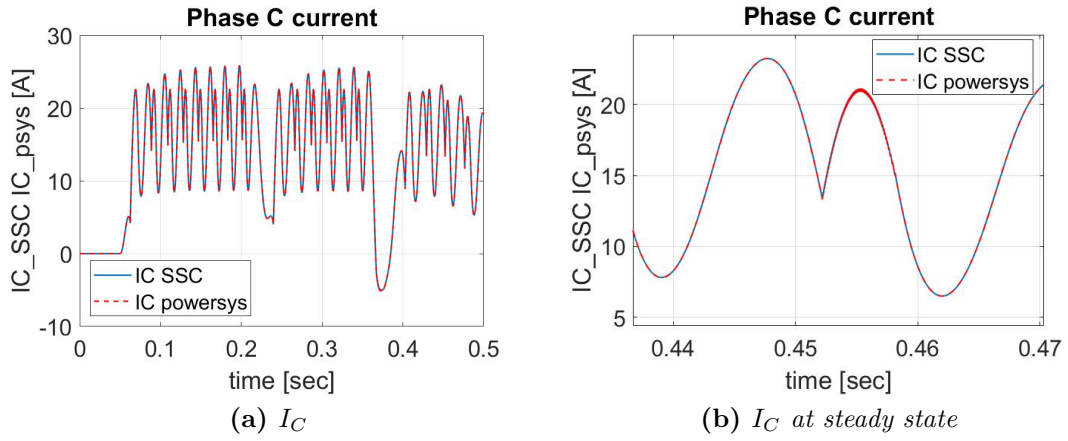


Figure B.21: Phase C current

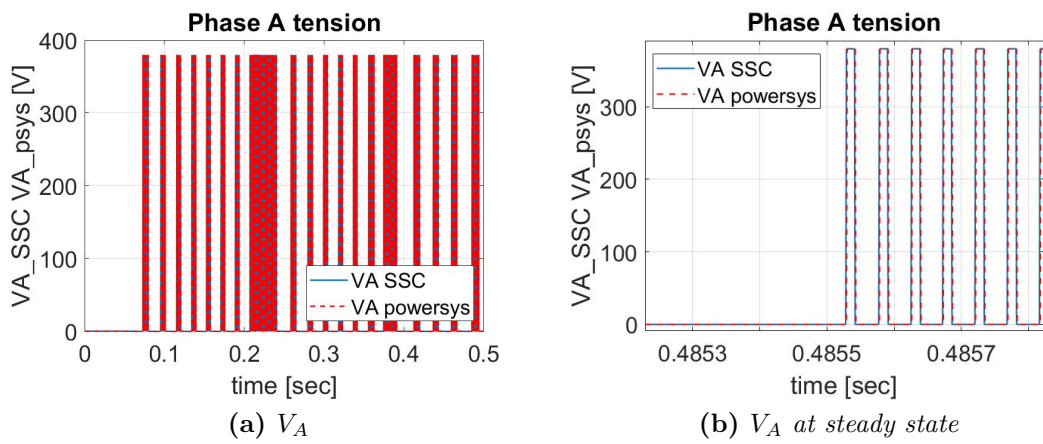


Figure B.22: Phase A tension

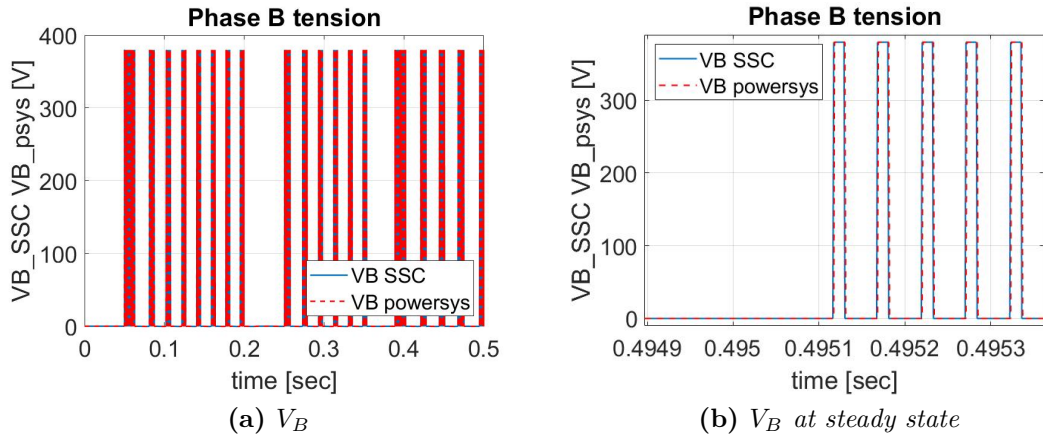


Figure B.23: Phase B tension

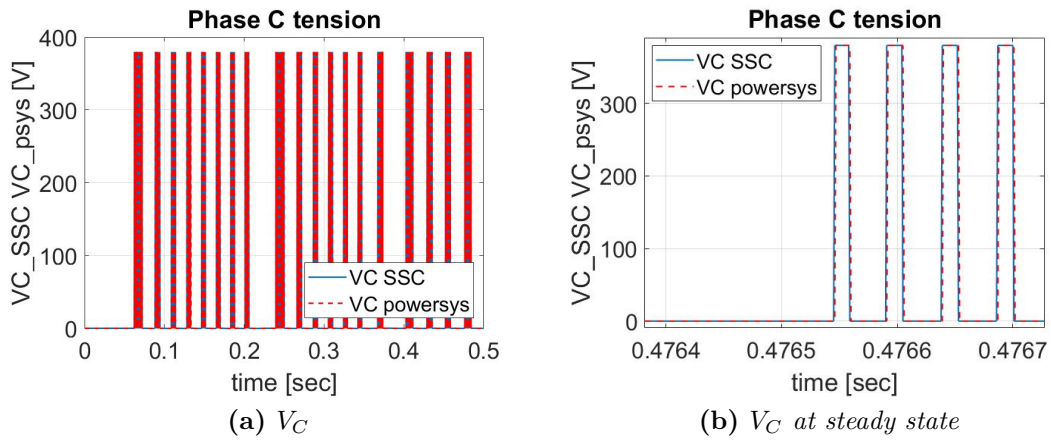


Figure B.24: Phase C tension

Bibliography

- [1] Z. Yu, «A review of electromechanical actuation system for more electric aircraft», *IEEE/CSAA International Conference on Aircraft Utility Systems (AUS)*, 2016.
- [2] G. Qiao, G. Liu, Z. Shi, Y. Wang, S. Ma, and T. Lim, «A review of electromechanical actuators for More/all Electric aircrafts systems», *J Mechanical Engineering Science 2018, Vol. 232(22) 4128-4151*, IMechE, 2017.
- [3] Vachtsevanos and G. J., *Intelligent fault diagnosis and prognosis for engineering systems. Vol. 456*. Hoboken: Wiley, 2006.
- [4] K. Goebel, M. J. Daigle, A. Saxena, I. Roychoudhury, S. Sankararaman, and J. R. Celaya, *The science of making predictions*, 2017.
- [5] R. Quigley, «More Electric Aircraft», in *Proceedings Eighth Annual Applied Power Electronics Conference and Exposition*,, 1993, pp. 906–911. DOI: 10.1109/APEC.1993.290667.
- [6] M. Howse, «All electric aircraft», *Power Engineer*, vol. 17, no. 4, pp. 35–37, 2003. DOI: 10.1049/pe:20030410.
- [7] P. Maggiore, *Slides and lessons of the course*, 2019.
- [8] J. Zhao and Y. Yu, «Brushless DC Motor Fundamentals Application Note», 2011.
- [9] P. Maggiore, *Slides and lessons of the course*, 2021.
- [10] V. Boschetti, «Development of an Experimental Test Bench for the Validation of Prognostic Algorithms for Electromechanical Actuators», Master’s Thesis, Politecnico di Torino, 2019.
- [11] P. Sciandra, «Development and Validation of Prognostic Algorithms for Electromechanical Actuators», Master’s Thesis, Politecnico di Torino, 2019.
- [12] Siemens, *SINAMICS S120/S150, List Manual*, 2018.
- [13] —, *SINAMICS S120 AC Drive, Product manual*, 2019.
- [14] —, *SIMOTICS Synchronous motors SIMOTICS S-1FK7 Generation 2, For SINAMICS S120, Configuration Manual*, 2018.

- [15] P. C. Berri, M. D. L. Dalla Vedova, P. Maggiore, and G. Riva, «Design and Development of a Planetary Gearbox for Electromechanical Actuator Test Bench through Additive Manufacturing», *Actuators* 2020, 9, 35.,
- [16] P. C. Berri, M. D. L. Dalla Vedova, P. Maggiore, and A. M. Bertetto, «Evaluation of Aiding and Opposing Load Efficiency for an Actuator Planetary Drive», *International Journal of Mechanics and Control*, Vol. 21, No. 01, pp. 113-120, 2020, 2020.
- [17] —, «Simplified Models for Mechanical Transmission Efficiency with Opposing and Aiding loads», *International Journal of Mechanics and Control*, Vol. 20, No. 01, 2019, 2019.
- [18] P. C. Berri, «Design and development of algorithms and technologies applied to prognostics of aerospace systems», Doctoral Dissertation, Politecnico di Torino, ScuDo, 2021.
- [19] —, «Genetic Algorithms for Prognostics of Electromechanical Actuators», Master's Thesis, Politecnico di Torino, 2016.
- [20] M. D. L. Dalla Vedova, *Slides and lessons of the course*, 2021.